Investigation of Spin Injection and Optical Imaging

With Scanning Probe Microscopy Techniques

Thesis by

Cory J. Hill

In Partial Fulfillment of the Requirements
for the Degree of
Doctor of Philosophy

California Institute of Technology
Pasadena, California

2001
(Submitted May 29, 2001)

Acknowledgements

First and foremost it is necessary to acknowledge the role of Prof. T. C. McGill in the production of this thesis. Tom has put together a research group of incredibly talented and competitive people and managed to have the group run in harmony. In this group we are granted the rare combination of the academic freedom to pursue our own interests and the considerable capital resources necessary for that pursuit. From what I have observed, it seems that having the training of students be the number one priority is becoming increasingly rare, and I am thankful to have benefited from a system like this one.

It was always a pleasure to work with the many senior students who came before me. Erik Daniel taught me about processing and the dual joys of the 6.1 Å materials and system administration. Xiao-Chang Cheng turned over his III-V MBE machine to me and probably aged a few years in the process. I know I'll have hard time giving the keys to the next grower. Eric Piquette and Alicia Alonzo were always helpful in and out of the lab. For several years I shared an office with Zvonimir Bandić, who taught me how to use the X-ray machine, PL setup, and never tired of edifying me in the areas of solid state physics in which I was ignorant and he was already master. Zvonimir also passed on the single most important lesson a grad student can learn: It's ok to break things. Best do it early and get the anxiety out of your system. (Of course there are numerous caveats to that rule.) Paul Bridger showed me how to use the scanning probe microscopes that show up all too often on the following pages. If I didn't like him so much, I would hold that against him. Bob Beach beat me out by a month so he gets mentioned in this paragraph. Without him the MBE room would be a much lonelier place, and that would be exacerbated by the fact that nothing would work.

The present generation of students is going to be great as well. Xavier Cartoixà has always been there for me with rigorous explanations of the solid state theory

behind the experiments I build and samples I grow. I enjoyed climbing the learning curve with Matthew Barton before he took the road most often avoided by other Caltech students. Robert Strittmater has provided color to the past few years, if a bit extreme on occasion. His SEM skills have come in handy quite often. Ed Preisler, although he resists the moniker, is becoming our oxide guru and has helped quite often in characterizing my growths. He has also tied my group record golf score, but that can't last forever. Stephan Ichiriu has taken a great burden from my shoulders by taking over the system administration, and will undoubtedly have as much fun as I have had with the scanning probes. Neal Oldham now shares my office and is always ready with a materials analysis of any problem that shows up. I must also thank the group's administrative assistant, Tim Harris, for making all the trains run on time. These guys will have a lot of fun over the next few years.

I have been privileged to interact with many former group members and associates during my brief five years here. David Ting has patiently explained the intricacies of quantum structures to me as he has to so many other students. David Chow and Jenna Zinck have shared with me valuable advice that has increased the quality of my III-V growths. Prof. Jim McCaldin has explained semiconductor surface physics to me on numerous occasions and pointed me down many fruitful avenues when I was trying to passivate GaAs surfaces. Ogden Marsh has saved all of us many hours of frustration with his materials and device processing experience. Gerry Picus has proofread all of my papers and provided a much needed voice of reason when experiments were frustrating.

I must mention the support my family gave to get me this far. My parents provided the opportunities that led me here. I daresay they are as happy about the situation as I am.

Finally, I must mention my wife, Akiko, who has put up with quite a bit during the writing of this thesis and the process of getting this far. Her love is one of the few things that gets me out of the lab. She has also carried our first child throughout the writing of this thesis, and had the magnanimity to hold him in long enough for me to get it finished.

Abstract

The work presented in thesis focuses on two important applications of scanning probe microscopy. The first is the attempt at measuring spin-polarized current injection from a ferromagnet into a semiconductor in an *ex-situ* environment at room temperature. The interface current-voltage characteristics in scanning tunneling microscopy (STM) offer one of the few viable methods that can produce the current densities and contact resistances necessary to surmount the theoretical barriers to this type of spin injection. Surface passivation techniques for the semiconductors used in these experiments are also discussed. Experimental data with different ferromagnetic tips on two types of semiconductors are presented. The results obtained in this and other spin injection experiments are explained with an interfacial equilibrium drift-diffusion theory.

The second part focuses on the theory of the generally accepted contrast mechanism in scanning apertureless microscopy (SAM). Simulations are presented of a dipole-dipole interaction model between the tip and sample. These simulations show that the dipole coupling model does indeed predict optical discrimination on the nanometer scale. Simulated images are contrasted with experiment in order to test the validity of the model.

Contents

List of Figures

List of Tables

Chapter 1 Introduction

1.1 Thesis Overview

This thesis is a report on the investigation into two important applications of scanning probe microscopy. Part I deals with the use of the scanning tunneling microscope (STM) to investigate the basic physics involved in injecting spin-polarized currents from ferromagnetic metals into semiconductors. Part II details our efforts in simulating the image contrast mechanism in scanning apertureless microscopy(SAM).

1.2 Motivation

1.2.1 Spin Injection and STM Light Emission

Spin-dependent tunneling phenomena have driven the exponential increase in magnetic data storage and retrieval with the use of GMR devices. These devices take advantage of conduction asymmetry in tunnel junctions where a non-ferromagnetic metal is sandwiched between two ferromagnetic layers. Although similar spin-based advances in semiconductor technology have not been forthcoming, many uses for semiconductors with spin population differences have been proposed. It is widely believed that quantum computing on a large scale must be spin-based in the solid state. Devices such as the spin-FET [1], where transistor action is achieved through gate modulation of the Rashba effect, have been proposed but not demonstrated. These devices require a robust method of injecting spin-polarized currents into semiconductors. Although spin-polarized electron populations in the conduction band have been produced by optically exciting carriers with circularly polarized light, in the foreseeable future electrical injection will be the method of choice for practical devices.

Uncontested electrical injection of spin into semiconductors from a metallic ferromagnet has only been reported once by Alvarado et al [2]. These experiments used an UHV STM setup with nickel tips to inject spin into a cleaved GaAs surface. The spin polarization of the electrons contributing to the optical recombination was determined through measuring the degree of circular polarization of the emitted luminescence. Other low temperature experiments using magnetic II-VI semiconductors coupled to GaAs quantum wells have also demonstrated sizable spin-injection [3, 4]. Only recently have theories been published [5, 6, 7] which explain why this type of experiment may work while other more pedestrian attempts at injecting spin into semiconductors fail.

The work presented in this thesis details our attempts to construct an experimental setup which allows us to investigate the STM spin injection phenomena with an *ex-situ* technique. We have used various ferromagnetic metals as current sources to induce luminescence from both gallium nitride (GaN) and gallium arsenide (GaAs) surfaces. Much effort was invested in passivating the surface of one of the semiconductors, GaAs, so that STM light emission experiments could be performed in air.

1.2.2 Scanning Apertureless Microscopy

Several years ago an apertureless optical microscope with claims of sub-nanometer resolution was developed by Wickramasinghe [8]. An instrument with the ability to measure optical properties on this scale could enable biological or chemical identification of molecules. However, as with any near-field optical technique, there is a question as to what portion of an ostensibly "optical" image is actually due to topography.

The mechanism proposed by Zenhausern et al. for the image contrast in SAM is a tip-sample dipole coupling model [9]. This model and its resolution claims have never been rigorously investigated. The work presented in part II of this thesis deals with the dipole theory and the optical images such a model would produce.

1.3 Summary of Results

1.3.1 Spin Injection and STM Light Emission

We have constructed an experimental setup which measures the Stokes parameters of the luminescence from the optical recombination near a semiconductor surface. A Digital Instruments Multimode STM operated in ambient conditions is used as the current source. The semiconductors used were gallium nitride (GaN) and gallium arsenide (GaAs), both of which have radiative recombination at wavelengths accessible to high gain, low noise photodetectors. GaN was used for the stable native oxide and low surface state density. GaAs was chosen due to its technological significance and many avenues were explored in producing a passivated surface. We have taken spectral data of the electroluminescence from GaN and nitride passivated GaAs surfaces to insure that we are looking at near bandgap recombination and not other types of light-emitting phenomenon common in STM work. Polarization control experiments were performed with commercially available PtIr tips. Magnetic experiments were performed with Ni, Co, and Fe tips fashioned from high-purity wire. We have demonstrated successful spin injection from all three magnetic materials into GaN. The GaAs samples have also exhibited interesting polarization behavior.

1.3.2 SAM

We have developed a computer simulation technique which uses data from an atomic force microscope (AFM) as a template for reconstructing optical images using the coupled dipole model. Simulations have been performed on 50 and 200 nm diameter size standards and compared with experiment. The dependence of image contrast on parameters such as tip size, sample index of refraction, illuminating wavelength and polarization, are discussed.

1.4 Chapter Outline

This thesis is divided into two parts. Part I deals with STM spin injection experiments and Part II deals with apertureless microscopy. Chapter 2 begins Part I with a brief history of spin injection. Chapter 3 presents the current theory of spin injection at semiconductor interfaces and applies it to common spin injection geometries. Details of the experimental setup and characterization of the STM luminescence are presented in Chapter 4. Circular polarization measurements with magnetic tips are the subject of Chapter 5. Chapter 6 begins Part II with an introduction to SAM and a derivation of the dipole coupling equations. In Chapter 7 the results of simulations and dipole visualization experiments are presented. Chapter 8 discusses the future of SAM.

Bibliography

[1] S. Datta and B. Das, Appl. Phys. Lett. **56**, 665 (1990).

[2] S. F. Alvarado and P. Renaud, J. Appl. Phys. **73**, 5816 (1993).

[3] B. T. Jonker, Y. D. Park, B. R. Bennett, H. D. Cheong, G. Kioseoglou, and A. Petrou, Phys. Rev. B **62**, 8180 (2000).

[4] R. Fiederling, M. Keim, G. Reuscher, W. Ossau, G. Schmidt, A. Waag, and L. W. Molenkamp, Nature **402**, 787 (1999).

[5] G. Schmidt, D. Ferrand, L. W. Molenkamp, A. T. Filip, and B. J. van Wees, Phys. Rev. B **62**, R4790 (2000).

[6] E. I. Rashba, Phys. Rev. B **62**, R16267 (2000).

[7] D. L. Smith and R. N. Silver, submitted to Phys. Rev. B.

[8] H. Wickramasinghe and C. Williams, 1989, Apertureless Near Field Optical Microscope, U.S. Patent 4,947,034.

[9] F. Zenhausern, M. P. Oboyle, and H. K. Wickramasinghe, Appl. Phys. Lett. **65**, 1623 (1994).

Part I

STM Spin Injection

Chapter 2 Background

2.1 History

Successful measurement of spin polarized tunneling was first reported by Tedrow and Meservey in 1971 [1, 2, 3]. They were able to measure the spin asymmetry in conductance from a ferromagnet into a superconducting metal film. From these measurements they were able to determine the spin polarization of Ni, Co, and Fe to be 23, 35, and 40%, respectively. Later experiments using MBE-prepared samples with high quality interfaces saw these values increase to 33, 42, and 44% [4].

The pioneering work by Julliere [5] in magnetoresistance and the later discovery of giant magnetoresistance parallel the study of electrical spin injection and have had a huge economic effect, with applications from data storage to the automobile industry.

The magnetoresistance work engendered in the scientific community the belief that ferromagnetic metal/normal metal spin injection efficiency is a function of the interfacial quality. This belief has carried over to studies involving ferromagnets and semiconductor interfaces, more as an excuse for the inability to successfully demonstrate spin injection than as a theoretical impediment for spin injection into semiconductors.

Work by Johnson and Silsbee [6] in 1985 showed that a spin polarized current from a ferromagnet could be injected into aluminum and could maintain its spin-polarized nature long enough to be measured electrically at a second contact. The spin-polarized nature of the injected current could be observed by a change in the voltage drop between two ferromagnetic contacts on the aluminum as an applied magnetic field alternately aligned or anti-aligned the magnetization directions of the contacts.

The Datta and Das proposal [7] in 1990 of a spin-FET transistor, where the gate voltage controls the precession of electron spins in the channel, provided the impetus for the design of many novel semiconductor devices which utilized the electron spin in the device function. The spin-FET combines the three crucial requirements of spin-based semiconductor devices: injection, manipulation, and retrieval of spin. This marks the beginning of the field of electronics based on spin phenomena in semiconductors, which is now known by the more common sobriquet "spintronics". The field of spintronics is currently a well-funded one. As such, it attracts a lot of attention, both theoretical and experimental.

The first experimental evidence of spin injection from a ferromagnetic metal into semiconductors was done in an in-situ STM experiment by Alvarado [8]. In this experiment, a Ni STM tip injected spin-polarized electrons into a cleaved p-type GaAs (110) surface. The emitted light was circularly polarized, indicative of overall spin injection. Much effort went into the UHV experimental setup, where manipulating the magnetic properties of tips in-situ and characterizing the emitted luminescence is a considerable endeavor [9]. The results of Alvarado provided an experimental proof of concept for most of the STM experiments detailed in this thesis.

Later attempts by Johnson [10] to measure spin injection, using a semiconductor structure in place of the aluminum in his experiments, yielded a 1% change in interface resistance with changing magnetic field. This was interpreted as a 20% spin injection efficiency. Johnson also developed a theory of spin dependent transport into semiconductors [11]. The conclusions of the theory and experiments were contested [12] by VanWees on the basis that local Hall effects and not spin injection explain the observed results. These points are still a matter of contention [13]. Monzon and Roukes [14] performed a thorough investigation of spin injection and local Hall effects for permalloy deposited on InAs and saw no unambiguous sign of spin injection. Interfacial spin-scattering was cited as a possible factor limiting spin injection.

Successful spin injection was demonstrated recently from a dilute magnetic semiconductor into a GaAs quantum well by both Jonker et al. [15] using ZnMnSe and Fiederling et al. [16] using BeMnZnSe lattice-matched to the quantum well. These devices took advantage of the large g factors in dilute magnetic II-VI semiconductors. At cryogenic temperatures in an applied field the magnetic energy splitting between spin-up and spin-down electrons becomes large with respect to kT. It is then possible to prepare a large difference in spin populations in the II-VI semiconductor. The experiments utilized this effect and characterized the light emission from a GaAs quantum well to determine the spin polarization. Similar experiments were performed by Ohno et al. [17], where Mn doped GaAs was used as the spin aligner. A much smaller effect was seen in this case due to the smaller g factor in GaAs as compared to the magnetic II-VI materials.

Several theories have evolved describing the injection of spin-polarized currents. Molenkamp [18] developed an injection theory based on a semiconductor drift-diffusion model and concluded that conventional implementations of spin injection like those used in the experiments of Johnson and Monzon could not work. Smith and Silver [19] have developed a unifying theory of spin injection into semiconductors. This theory explains the original Johnson results and the well-known properties of GMR devices, as well as the successful attempts at injecting spin into semiconductors. This theory has guided the materials selection and processing techniques of most of the work presented here. A similar theory was also published recently by Rashba [20]. Because of its importance in understanding the motivation behind our experiments, the salient aspects of the Smith theory will be presented in the next chapter.

Bibliography

[1] R. Meservey, P. M. Tedrow, and P. Fulde, Phys. Rev. Lett. **25**, 1270 (1970).

[2] R. Meservey and P. M. Tedrow, Phys. Rev. Lett. **26**, 192 (1971).

[3] R. Meservey and P. M. Tedrow, Phys. Rev. B. **7**, 318 (1973).

[4] J. S. Moodera, J. Nassar, and G. Mathon, Ann. Rev. Of Mat. Sci. **29**, 381 (1999).

[5] M. Julliere, Phys. Lett. **54A**, 225 (1975).

[6] M. Johnson and R. H. Silsbee, Phys. Rev. Lett. **55**, 1790 (1985).

[7] S. Datta and B. Das, Appl. Phys. Lett. **56**, 665 (1990).

[8] S. F. Alvarado and P. Renaud, J. Appl. Phys. **73**, 5816 (1993).

[9] S. F. Alvarado, H. Riechert, and N. E. Christensen, Phys. Rev. Lett. **55**, 2716 (1985).

[10] P. R. Hammar, B. R. Bennett, M. J. Yang, and M. Johnson, Phys. Rev. Lett. **83**, 203 (1999).

[11] M. Johnson, Phys. Rev. B **58**, 9635 (1998).

[12] B. J. van Wees, Phys. Rev. Lett. **84**, 5023 (2000).

[13] P. R. Hammar, B. R. Bennett, M. J. Yang, and M. Johnson, Phys. Rev. Lett. **84**, 5024 (2000).

[14] F. G. Monzon and M. L. Roukes, J. Magn. & Magn. Mater. **199**, 632 (1999).

[15] B. T. Jonker, Y. D. Park, B. R. Bennett, H. D. Cheong, G. Kioseoglou, and A. Petrou, Phys. Rev. B **62**, 8180 (2000).

[16] R. Fiederling, M. Keim, G. Reuscher, W. Ossau, G. Schmidt, A. Waag, and L. W. Molenkamp, Nature **402**, 787 (1999).

[17] Y. Ohno, D. K. Young, B. Beschoten, F. Matsukura, H. Ohno, and D. D. Awschalom, Nature **402**, 790 (1999).

[18] G. Schmidt, D. Ferrand, L. W. Molenkamp, A. T. Filip, and B. J. van Wees, Phys. Rev. B **62**, R4790 (2000).

[19] D. L. Smith and R. N. Silver, submitted to Phys. Rev. B.

[20] E. I. Rashba, Phys. Rev. B **62**, R16267 (2000).

Chapter 3 Theory of Spin Injection

3.1 Background

The theory presented here was worked out in detail by Smith and Silver [1], and we follow their derivation closely. In earlier work by Schmidt et al. [2], it was first pointed out that the high conductivity of the ferromagnetic metals poses a significant barrier to spin injection into semiconductors. Similar results were obtained by Rashba [3], who reported on the utility of tunnel contacts in overcoming the conductivity mismatch problem.

3.2 Equilibrium Theory of Spin Injection at Semiconductor Interfaces

We assume a non-degenerate semiconductor is in electrical contact with a ferromagnet. The region where $x < 0$ is the semiconductor and $x > 0$ is the ferromagnet. The interface is at $x = 0$. In this configuration the current density j will be positive for electron injection into the semiconductor.

In the semiconductor conduction band the ratio of spin-up electrons to the total number of electrons is

$$\alpha_s = \frac{n_{\uparrow s}}{n_{\uparrow s} + n_{\downarrow s}}, \tag{3.1}$$

where n_s is the electron density for the indicated spin type. This is related to the spin polarization, which is defined as

$$P_s = \frac{n_{\uparrow s} - n_{\downarrow s}}{n_{\uparrow s} + n_{\downarrow s}}. \tag{3.2}$$

In order for the two electron densities to differ at a given point in the semiconductor, they must be allowed to have different chemical potentials, such that

$$n_{\eta s} = n_o \exp \frac{-(E_c - \mu_\eta)}{kT}, \tag{3.3}$$

where n_o is the intrinsic electron concentration, E_c is the conduction band edge, and η represents one of the two spin types. This allows us to express α_s as

$$\alpha_s = \frac{1}{1 + exp(-\frac{\Delta\mu}{kT})}, \tag{3.4}$$

where $\Delta\mu = \mu_\uparrow - \mu_\downarrow$. This difference in chemical potentials can only occur when the spins are driven out of equilibrium. The difference in chemical potentials must relax like a diffusion equation [2]

$$\frac{\partial^2(\mu_\uparrow - \mu_\downarrow)}{\partial x^2} = \frac{\mu_\uparrow - \mu_\downarrow}{\Lambda^2}, \tag{3.5}$$

where Λ is the spin diffusion length in a given material. With the boundary condition that $\Delta\mu$=0 far from the interface ($x \rightarrow \pm\infty$) the solution to 3.5 is

$$\Delta\mu = K_s \exp \frac{x}{\Lambda_s} \quad x < 0 \tag{3.6}$$

$$\Delta\mu = K_f \exp \frac{-x}{\Lambda_f} \quad x > 0, \tag{3.7}$$

where K_s and K_f are the values of $\Delta\mu$ evaluated on the semiconductor and ferromagnet sides of the interface, respectively. The drift-diffusion equations for each spin type are [4]

$$qj_\eta = \sigma_\eta \frac{\partial \mu_\eta}{\partial x}. \tag{3.8}$$

At the interface the current for each spin type is

$$qj_\eta^0 = C_\eta \Delta\mu_\eta, \tag{3.9}$$

where j_η^0 is the current density evaluated at the interface, C_η is the contact conductance, and $\Delta\mu_\eta$ is the discontinuity in chemical potential for spin type η. $1/C_\eta$ is the contact resistance for spin type η.

The transformation of variables $\beta j = j_\uparrow$ and $(1-\beta)j = j_\downarrow$ greatly simplifies the algebra in solving for α_s. Using equations 3.6 and 3.9 we find

$$K_s - K_f = -qj\left(\beta\left(\frac{1}{C_\downarrow}+\frac{1}{C_\uparrow}\right)-\frac{1}{C_\downarrow}\right). \tag{3.10}$$

Evaluating the drift-diffusion equation at each side of the interface gives

$$\begin{aligned}
\frac{K_s}{\Lambda_s} &= \frac{\partial}{\partial x}\left(\mu_\uparrow - \mu_\downarrow\right)|_{x=0^-}\\
&= \frac{qj_{\uparrow s}}{\sigma_{\uparrow s}} - \frac{qj_{\downarrow s}}{\sigma_{\downarrow s}}\\
&= \frac{qj}{\sigma_s}\left(\frac{\beta-\alpha_s}{\alpha_s\left(1-\alpha_s\right)}\right)\\
K_s &= qj\Lambda_s R_s\left(\beta-\alpha_s\right), \qquad (3.11)
\end{aligned}$$

where 3.11 makes use of the modified bulk resistivity, R, where

$$\begin{aligned}
R &= \left(\frac{1}{\sigma_\uparrow}+\frac{1}{\sigma_\downarrow}\right)\\
R &= \frac{1}{\sigma\alpha\left(1-\alpha\right)} \qquad (3.12)
\end{aligned}$$

for a given material. R is the sum of the bulk resistivities for each spin type. It varies from four times the bulk resistivity for an unpolarized source to infinity for a 100% spin polarized source. In iron, cobalt, and nickel, where $\alpha_f \approx 0.7$ [5], we have R_f is 4.8 times the bulk resistivity.

The solution for β can be found by subtracting the expression for K_f from K_s in 3.11 and equating the result with 3.10. We find

$$\beta = \frac{\Lambda_s R_s \alpha_s + \Lambda_f R_f \alpha_f + \frac{1}{C_\downarrow}}{\Lambda_s R_s + \Lambda_f R_f + \frac{1}{C_\downarrow} + \frac{1}{C_\uparrow}}. \tag{3.13}$$

We can now rearrange 3.11 and after considerable algebraic manipulation find an expression for α_s

$$\alpha_s = \frac{C_\downarrow \Lambda_f R_f \alpha_f + 1}{C_\downarrow + \frac{C_\downarrow}{C_\uparrow}\Lambda_f R_f + 1} + \left(\frac{C_\downarrow}{C_\downarrow + \frac{C_\downarrow}{C_\uparrow}\Lambda_f R_f + 1} + \frac{1}{\Lambda_s R_s} \right) \frac{K_s}{qj} \tag{3.14}$$

which is a transcendental equation for α_s, since we have from 3.4 that

$$K_s = -kTln\left(\frac{1}{\alpha_s} - 1\right). \tag{3.15}$$

The essence of equation 3.14 is the following: in the absence of a 100% spin polarized ferromagnet very large current densities are required to inject spin from a metallic contact into a semiconductor. Furthermore, if a difference in contact resistances for each spin type cannot be achieved, then the contact conductance-bulk resistivity product must be large, such that $R_f \Lambda_f C_\downarrow \geq 1$.

Equation 3.14 has all of the information necessary for explaining qualitatively the results of previous spin injection experiments involving semiconductors. There are two important limiting cases. The first is when the contact conductance at the interface is very high (negligible contact resistance). In this regime, $C_\downarrow \Lambda_f R_f \gg 1$ and

$$\alpha_s = \alpha_f + \left(\frac{1}{R_f \Lambda_f} + \frac{1}{R_s \Lambda_s} \right) \frac{K_s}{qj}. \tag{3.16}$$

In this case the first term in 3.14 simplifies to α_f and allows significant spin polarization of the injected current at high current densities. When dealing with metals the last term in 3.14 becomes pivotal. Experiments by Hammar et al. [6] and Monzon et al. [7], using ferromagnetic contacts on InAs, failed to yield significant spin injection. Although InAs has a small band gap and can have very high electron mobility, its resistivity is still orders of magnitude smaller than that of the metallic contact. Coupling this with the very low current densities used in these experiments forces the injected spin polarization to be near zero. However, in the UHV tunneling microscopy experiments of Alvarado, measurement of successful spin injection from nickel into GaAs was reported. The very high current densities available in an STM configuration can substantially separate the chemical potentials for the two different spin types in the semiconductor near the interface.

Figure 3.1 illustrates this point. The top panel is for a metallic contact on a semiconductor. The spin fraction in the semiconductor at the interface cannot saturate to the value in the ferromagnet unless extremely high current densities are used. This is the so-called the conductivity mismatch problem pointed out by Schmidt [2]. The current density must be very large to overcome the factor of $1/(\Lambda_f R_f)$ in the denominator of the second part of equation 3.16. However, if we let the ferromagnet have much higher resistivities, we have the situation shown in the bottom panel of figure 3.1, where much lower current densities are needed to saturate α_s.

The works of Fiederling et al. [8] and Jonker et al. [9] involved a magnetic II-VI semiconductor used to inject spin polarized current into a GaAs quantum well. In this case both the magnetic source and the target material had high resistivities and the experiments were performed at liquid helium temperatures. The temperature difference helps to reduce the current density necessary to saturate α_s to the contact value. Figure 3.2 shows that low temperatures coupled with semiconductor contacts allow spin injection at realizable current densities.

When the contact conductance is small, such that $C_\downarrow \Lambda_f R_f \ll 1$, we see that

$$\alpha_s = \frac{1}{1 + C_\downarrow / C_\uparrow} + \left(\frac{C_\downarrow}{1 + C_\downarrow / C_\uparrow} + \frac{1}{R_s \Lambda_s} \right) \frac{K_s}{qj}. \tag{3.17}$$

Here, there can be no spin injection unless there is a difference in interface resistance for the two spin types. However, as shown in the lower panel figure 3.2, when a difference does exist, the saturation value of α_s only depends on the ratio of the contact resistances. Significant spin injection can occur with a spin selective interface, such as a ferromagnetic insulator acting as a tunnel barrier. It is not expected that the STM can provide this spin-dependant tunnel barrier, since the difference in k values for the two spin types in the ferromagnet at the Fermi level is very small with respect to k_F, the average value of k at the Fermi level.

The theory makes several predictions about which types of spin injection experiments should work. Both the current densities and contact resistances necessary

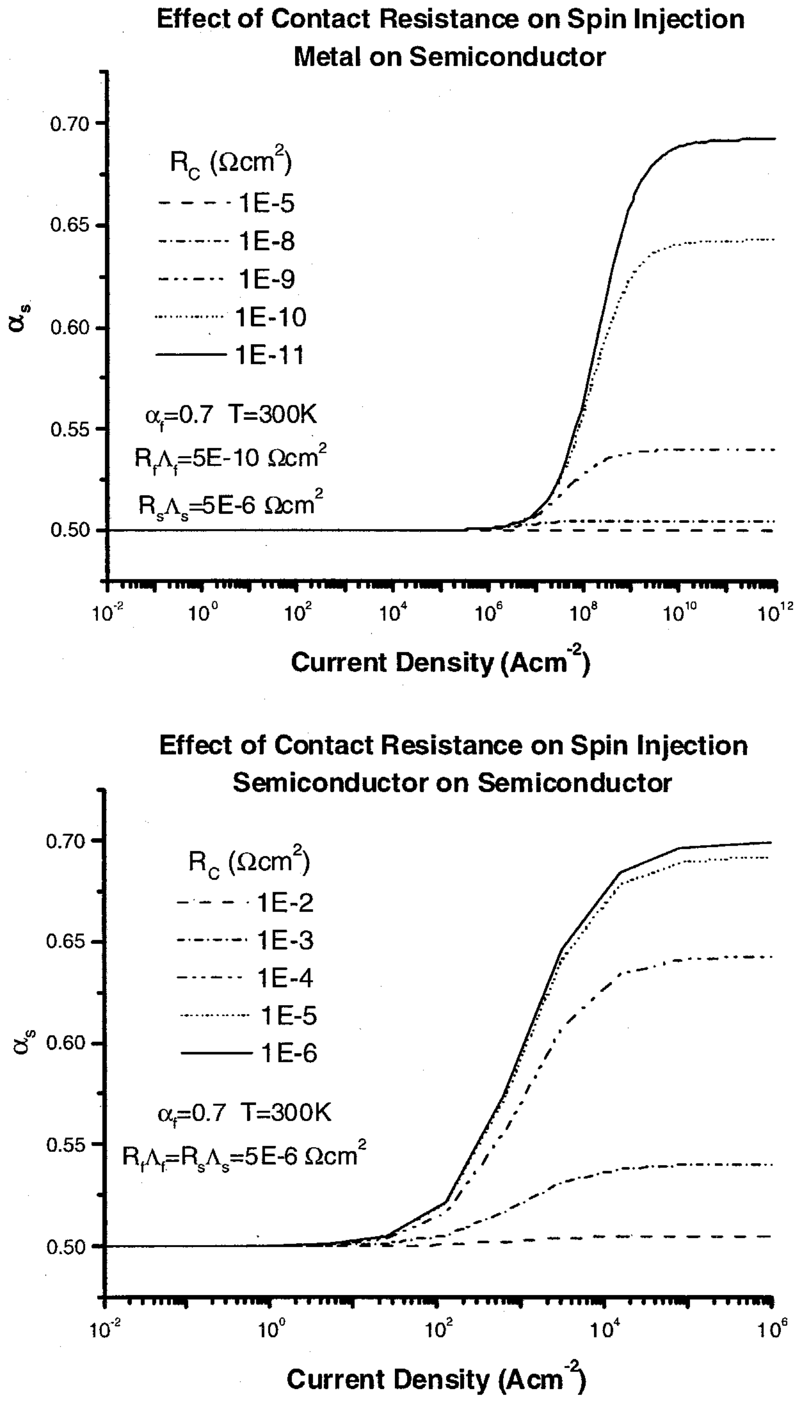

Figure 3.1: Solutions to Spin Injection Equations I. Each panel plots the semiconductor spin polarization α_s versus current density for different contact resistances. Top panel is for metallic contacts on semiconductors. Lower panel is for semiconductor-semiconductor contacts.

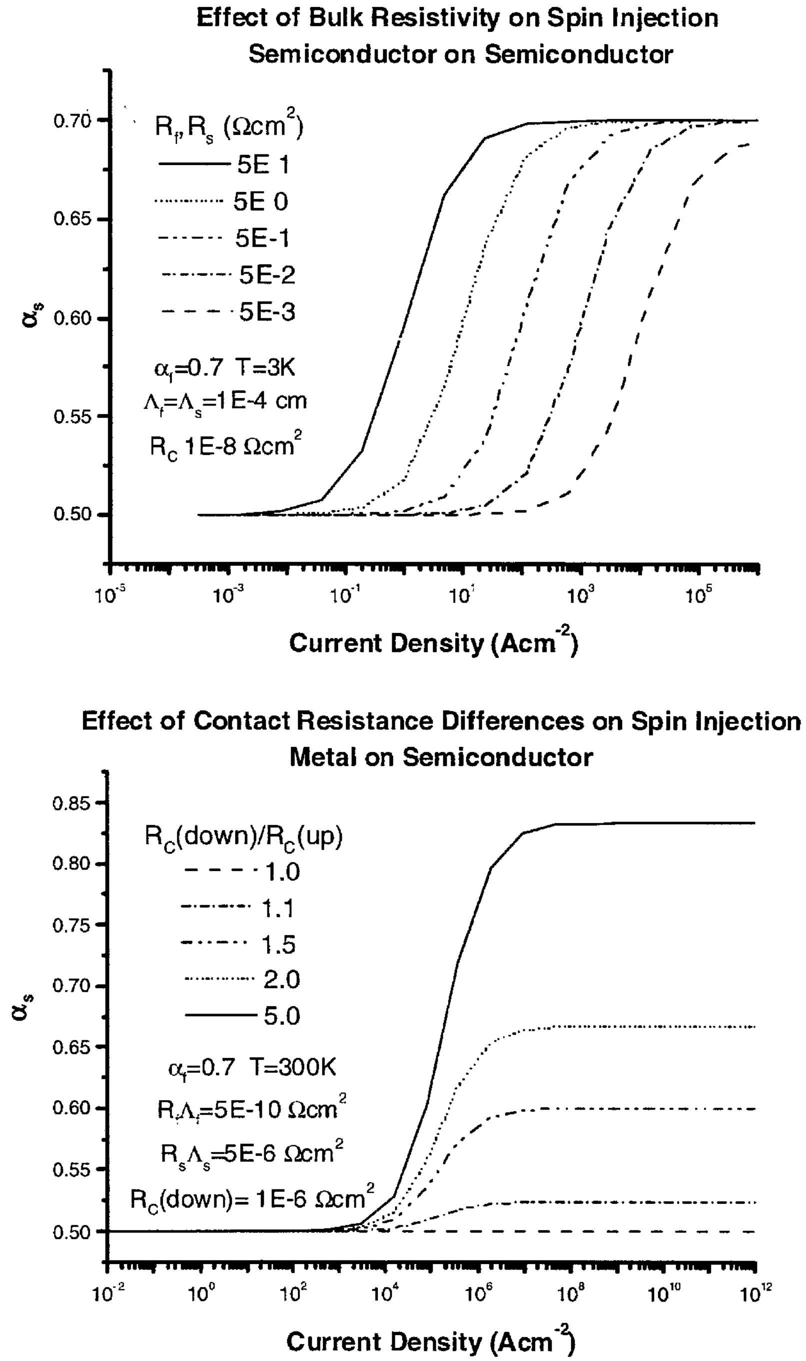

Figure 3.2: Solutions to Spin Injection Equations II. Each panel plots the semiconductor spin polarization α_s versus current density. Top panel relates directly to the spin injection experiments of Jonker and Fiederling, where semiconductor-semiconductor contacts are used at liquid helium temperatures. Each line corresponds to a different value of bulk resistivity. Lower panel shows the results for the metal-semiconductor case when the contact resistance for each spin type is different.

to saturate the spin injection to the value in a ferromagnetic metallic contact are unattainable in conventional devices. A current density of 10^8 Acm^{-2} will destroy any conventional electric contact, and contact resistances better than 10^{-8} Ωcm^{-2} are difficult to achieve even with the best ohmic contact processing technology. The STM, however, solves both of these technical difficulties. A conservatively large estimate of the contact area would be on the order of 10^{-14} cm^2, or one nm^2. An injected current of 10 nA would give a current density of 10^6 Acm^{-2}. Larger currents can get the current density on the order of 10^8 Acm^{-2}. The contact resistance can be approximated by attributing to it all of the voltage drop in the STM experiment. Dropping 1V across the tunnel barrier with a current of 10nA would give an interface resistance of 10^8 Ω. This is spread out over 10^{-14} cm^2, giving a contact resistance on the order of 10^{-6} Ωcm^2. In the experiments we use currents on the order of 1 μA and tip biases of 7 to 9 V. This would give a contact resistance on the order of 10^{-9} Ωcm^2, enough to begin seeing spin injection effects. The uncertainty in material parameters, like spin diffusion lengths and tip dimensions, can change the onset of significant spin injection. In the STM injection experiments we know that we are at least on the correct order of magnitude in terms of current density and contact resistance. Therefore, the STM is a perfect place to begin looking for spin injection effects.

3.3 Measurement of STM Spin Injection

In order to derive equations connecting the circular polarization of the STM luminescence to spin injection we must first consider the allowed transitions and their relative probabilities. To this we must add the geometrical aspects of the experimental setup. Finally, spin relaxation times in the conduction band must be considered.

Figure 3.3 is a simple schematic showing the setup and basic concepts involved in looking for spin injection with an STM setup. The STM tip is a ferromagnetic metal uniformly magnetized parallel or antiparallel to the tip axis. The spin polarization of the ferromagnet is taken to be the bulk value as determined by Andreev reflection experiments [5]. The magnetic energy of an electron in a magnetic field $\vec{B}$ is [10]

$$\begin{aligned} U &= -\vec{\mu} \cdot \vec{B} \\ &= \frac{gq}{2m} \vec{s} \cdot \vec{B}, \end{aligned} \tag{3.18}$$

where q is the absolute value of the electron charge and $\vec{\mu}$, g, $\vec{s}$ and m are the magnetic moment, g-factor, spin and mass of the electron, respectively. Therefore, the electron energy is lowest when the spin and the internal field of the ferromagnet are anti-aligned. The conduction subband with the lowest energy therefore has the spin of the electrons anti-aligned with the internal field. The electrons in this subband are referred to as the magnetic majority spins. This is in contrast to the conduction majority spins, which belong to the subband with the largest density of states at the Fermi level.

In the experiment we place the tip near a semiconductor and apply a bias, so that electrons are injected from the ferromagnet into the conduction band of the semiconductor. We choose to call the axis of the tip the z axis. For simplicity, at this point we assume the electron states can be represented by eigenstates of the full rotation group, $|s, m_s\rangle$. An electron with spin up along the z ($|1/2, 1/2\rangle$ state) axis in the conduction band of the semiconductor can recombine with a hole in any of the valence bands. The resulting photon must have angular momentum ± 1. For the zincblendes, the possibilities for recombination are fairly simple. If the electron recombines with a state in the heavy hole band, the only allowed transition is to a $|3/2, 3/2\rangle$ state with the photon created having an angular momentum of -1 along the z axis. This photon is right circularly polarized (RCP or σ^-), using the naming convention standard in optics. If the transition is to the light hole band, it must take place to a $|3/2, -1/2\rangle$ state and the photon will have an angular momentum of $+1$ along the z axis. In the unlikely event the transition is to the split-off band, it must take place to a $|1/2, -1/2\rangle$ state and the photon will again have an angular momentum of $+1$ along the z axis. Both of these transitions will be left circularly polarized (LCP or σ^-). In the wurzite crystal structure, the picture is essentially the same, but there is some mixing of the crystal split light hole states. Group theoretical considerations show that it is still true in wurzite that transitions from a spin-up state in the conduction band state to the top valence band would yield RCP photons, and transitions to the bottom two valence bands will yield LCP photons. The spin-orbit interaction is very weak in the nitrides and the crystal split band is only 26 meV below the light hole band. This will make the intensity ratios in GaN smaller than for GaAs.

3.3.1 Band Basics

In GaAs at the Γ point the conduction band states have s-like symmetry and the valence band states have p-like symmetry. For a cubic crystal the degeneracy of the p levels is not lifted by the crystal field [13]. The spin orbit interaction splits the p levels into the 4-fold $P_{3/2}$ and 2-fold $P_{1/2}$ states. Representations for these states consistent with the crystal symmetry are given in Table 3.1 [11]. Since the spin-orbit effect pulls the split-off band 0.34 eV below the valence band maximum, we can ignore these states in our luminescence analysis, as the thermal population of holes will be negligible. Given the wave functions for the $P_{3/2}$ states, we can determine the relative intensity ratios of transitions to the heavy and light hole bands from a $|S\uparrow\rangle$ state. The interaction Hamiltonian in the transition matrix elements $|\langle\phi_f|H_{int}|\phi_i\rangle|^2$ takes the form $H_{int} \propto X \pm iY$ for $\sigma^\pm$ light. We can replace $(X \pm iY)/\sqrt{2}$ and Z with the spherical harmonics $Y_1^{\pm 1}$ and Y_1^0 for ease in performing the calculations. Since the radial parts will cancel out, we can see that the ratio of heavy hole to light hole transition probabilities is

$$\frac{|\langle\frac{3}{2},\frac{3}{2}|Y_1^1|\frac{1}{2},\frac{1}{2}\rangle|^2}{|\langle\frac{3}{2},-\frac{1}{2}|Y_1^{-1}|\frac{1}{2},\frac{1}{2}\rangle|^2} = 3. \tag{3.19}$$

Here the transition to a heavy hole would emit a σ^- photon and the transition to the light hole would emit a σ^+ photon.

The maximum circular polarization of the emitted light for states in the conduction band all oriented along $+z$ would then be

$$V_{GaAs}^{max} = \frac{I_{RCP} - I_{LCP}}{I_{RCP} + I_{LCP}} = \frac{1}{2}. \tag{3.20}$$

If instead we choose an arbitrary direction $\hat{n}$ along which to align the spins in the conduction band where

$$\hat{n} = sin\theta cos\phi\hat{x} + sin\theta sin\phi\hat{y} + cos\theta\hat{z}, \tag{3.21}$$

θ is the polar angle between $\hat{n}$ and z and ϕ is the azimuthal angle. Then our spin eigenstates will be [14] $\cos\frac{\theta}{2}|1/2, 1/2\rangle + e^{i\phi}\sin\frac{\theta}{2}|1/2, -1/2\rangle$ and the maximum circular polarization of the emitted light will be reduced to

$$V = V^{max}(cos^2\frac{\theta}{2} - sin^2\frac{\theta}{2}) = V^{max}cos\theta. \tag{3.22}$$

In GaN the crystal structure is wurzite and consequently the crystal field splits the p levels [15]. When the spin-orbit interaction is applied, the result is three 2-fold degenerate levels. The splitting is actually quite small [12], as indicated in the lower panel of Figure 3.4. These energy splittings determine the mixing of the states, as represented by the a and b coefficients in Table 3.1. Their values are [15] $|a|^2$=0.929 and $|b|^2$=0.071. In a manner similar to that used for GaAs we can calculate the maximum circular polarization for luminescence from GaN. However, now we must take into account the energy splittings as well, by using Boltzmann statistics to determine the relative densities of states in each valence band. This calculation has been performed by X. Cartoixà [16] and a value of

$$V_{GaN}^{max} = 0.28 \tag{3.23}$$

was obtained.

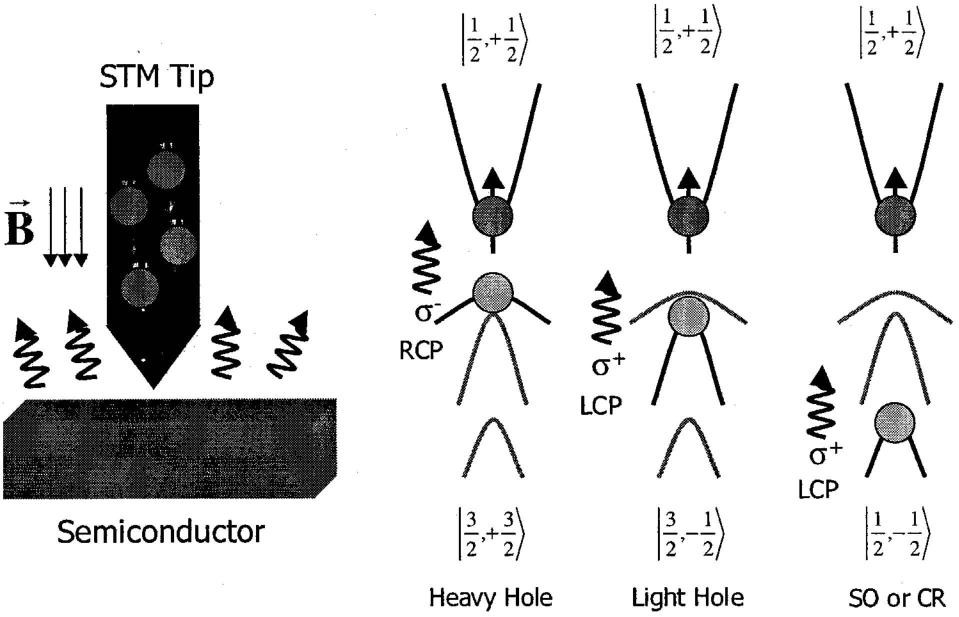

Figure 3.3: Cartoon of Spin-Dependent Recombination in Semiconductors

Symmetry Point	$\lvert J, m_j\rangle$	Wave Function
GaAs [11]		
Γ_6	$\lvert\frac{1}{2},\frac{1}{2}\rangle$	$\lvert S\uparrow\rangle$
	$\lvert\frac{1}{2},\frac{-1}{2}\rangle$	$\lvert S\downarrow\rangle$
Γ_7	$\lvert\frac{1}{2},\frac{1}{2}\rangle$	$\lvert-\frac{1}{\sqrt{3}}(X+iY)\downarrow-\frac{1}{\sqrt{3}}Z\uparrow\rangle$
	$\lvert\frac{1}{2},\frac{-1}{2}\rangle$	$\lvert\frac{1}{\sqrt{3}}(X-iY)\uparrow-\frac{1}{\sqrt{3}}Z\downarrow\rangle$
Γ_8	$\lvert\frac{3}{2},\frac{3}{2}\rangle$	$\lvert\frac{1}{\sqrt{2}}(X+iY)\uparrow\rangle$
	$\lvert\frac{3}{2},\frac{-3}{2}\rangle$	$\lvert\frac{1}{\sqrt{2}}(X-iY)\downarrow\rangle$
	$\lvert\frac{3}{2},\frac{1}{2}\rangle$	$\lvert-\frac{1}{\sqrt{6}}(X+iY)\downarrow-\sqrt{\frac{2}{3}}Z\uparrow\rangle$
	$\lvert\frac{3}{2},\frac{-1}{2}\rangle$	$\lvert\frac{1}{\sqrt{6}}(X-iY)\uparrow+\sqrt{\frac{2}{3}}Z\downarrow\rangle$
GaN[15]		
Γ_7		$\lvert iS\uparrow\rangle$
		$\lvert iS\downarrow\rangle$
Γ_9		$\lvert-\frac{1}{\sqrt{2}}(X+iY)\uparrow\rangle$
		$\lvert\frac{1}{\sqrt{2}}(X-iY)\downarrow\rangle$
$\Gamma_7^{(1)}$		$\lvert a\frac{1}{\sqrt{2}}(X-iY)\uparrow+bZ\downarrow\rangle$
		$\lvert-a\frac{1}{\sqrt{2}}(X+iY)\downarrow+bZ\uparrow\rangle$
$\Gamma_7^{(2)}$		$\lvert b\frac{1}{\sqrt{2}}(X-iY)\uparrow-aZ\downarrow\rangle$
		$\lvert-b\frac{1}{\sqrt{2}}(X+iY)\downarrow-aZ\uparrow\rangle$

Table 3.1: Angular part of the wavefunction for states in GaAs and GaN

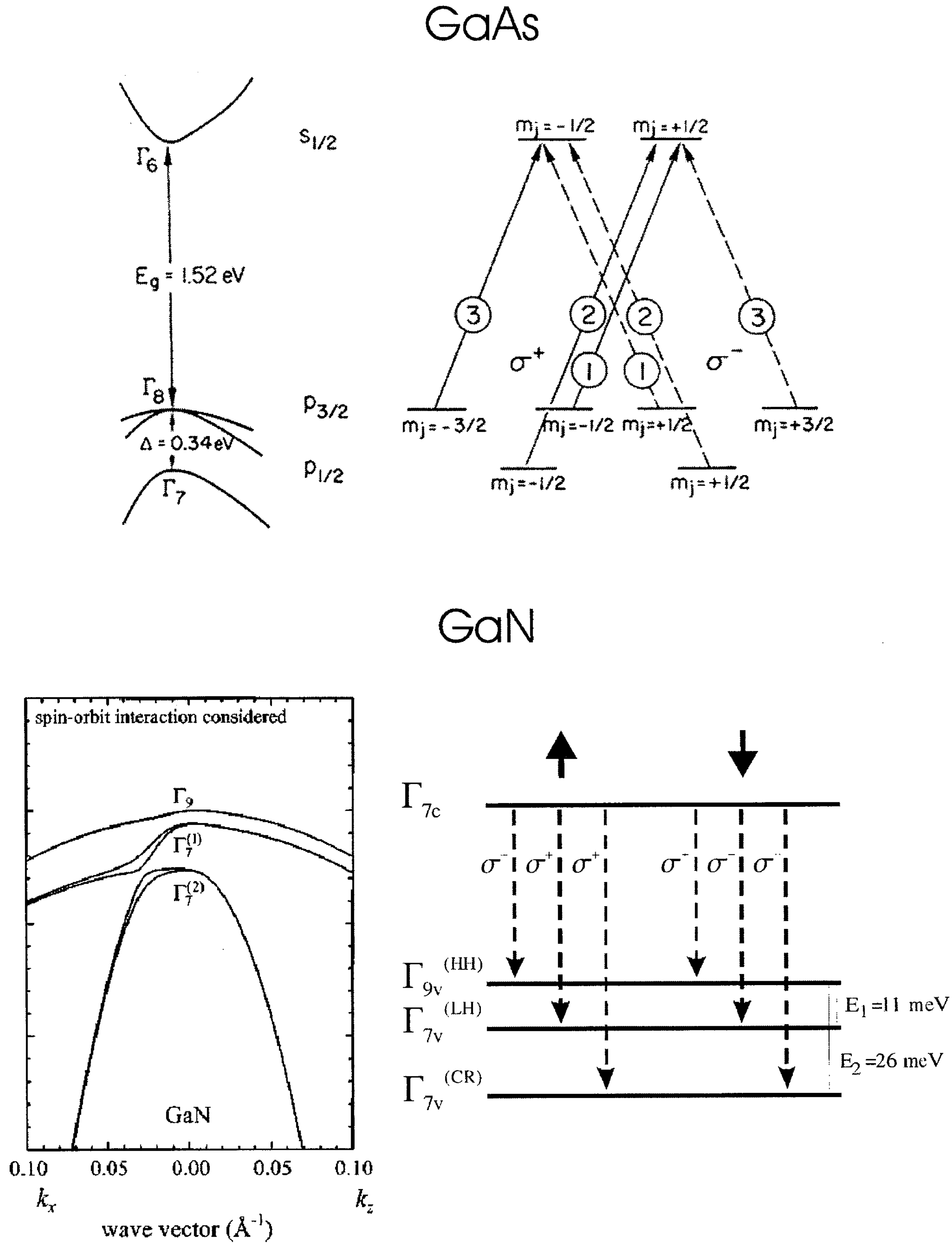

Figure 3.4: Band Structure and Transition Probabilities in GaAs (from Pierce and Meier [11]) and GaN (band diagram from Yeo et al. [12])

3.3.2 Lifetimes

Here we follow the derivation of Pierce and Meier [11, 17] in determining the effect of spin relaxation times on the recombination luminescence. An excess spin population ΔN_0 in the conduction band will decay with a characteristic time, τ_s, such that

$$\Delta N = N\uparrow - N\downarrow = \Delta N_0 e^{-t/\tau_s}, \tag{3.24}$$

where the total number of electrons in the conduction band is $N = N\uparrow + N\downarrow$ and a subscript 0 indicates the value at t=0. N_0 will decay with time as electrons recombine with a characteristic time τ, such that

$$N(t) = N_0 e^{-t/\tau}. \tag{3.25}$$

For steady-state current injection

$$\frac{dN\uparrow}{dt} = G\uparrow - \frac{1}{2}\frac{N\uparrow - N\downarrow}{\tau_s} - \frac{N\uparrow}{\tau} = 0 \tag{3.26}$$

and

$$\frac{dN\downarrow}{dt} = G\downarrow - \frac{1}{2}\frac{N\downarrow - N\uparrow}{\tau_s} - \frac{N\downarrow}{\tau} = 0, \tag{3.27}$$

where G is the generation rate for each spin type. Using these two equations we can solve for the spin polarization of the injected current at the interface, P_f, where

$$P_f = \frac{G\uparrow - G\downarrow}{G\uparrow + G\downarrow} = \frac{(N\uparrow - N\downarrow)/\tau_s + (N\uparrow - N\downarrow)/\tau}{(N\uparrow + N\downarrow)/\tau} \tag{3.28}$$

and therefore the spin polarization of the electrons when they recombine will be

$$P = \frac{P_f}{1 + \tau/\tau_s} \tag{3.29}$$

and, as one would expect, the smaller τ_s is with respect to τ, the smaller the spin population will be.

3.3.3 Measurements

Putting all of the results together, we see that when we make a measurement of the circular polarization of luminescence induced in a semiconductor with a spin polarized current, our measured value V will be

$$V = V^{max} \frac{P_f \cos\theta}{1 + \tau/\tau_s}. \tag{3.30}$$

In this equation V^{max} is the maximum circular polarization of the inter-band luminescence allowed by the semiconductor band structure for a 100% spin polarized electron population in the conduction band. This will be reduced by the following factors:

- P_f, the spin polarization of the current being injected into the semiconductor
- $\cos\theta$, where θ is the angle the magnetization on the tip makes with the surface normal
- $1/(1+\tau/\tau_s)$, where τ and τ_s are the electron recombination and spin relaxation lifetimes, respectively.

This equation will be used in the analysis of the magnetic measurements presented in Chapter 5.

Bibliography

[1] D. L. Smith and R. N. Silver, submitted to Phys. Rev. B.

[2] G. Schmidt, D. Ferrand, L. W. Molenkamp, A. T. Filip, and B. J. van Wees, Phys. Rev. B **62**, R4790 (2000).

[3] E. I. Rashba, Phys. Rev. B **62**, R16267 (2000).

[4] P. C. Van Son, H. Van Kempen, and P. Wyder, Phys. Rev. Lett. **58**, 2271 (1987).

[5] R. J. Soulen, M. S. Osofsky, B. Nadgorny, T. Ambrose, P. Broussard, S. F. Cheng, J. Byers, C. T. Tanaka, J. Nowack, J. S. Moodera, G. Laprade, A. Barry, and M. D. Coey, J. Appl. Phys. **85**, 4589 (1999).

[6] P. R. Hammar, B. R. Bennett, M. J. Yang, and M. Johnson, J. Appl. Phys. **87**, 4665 (2000).

[7] F. G. Monzon and M. L. Roukes, J. Magn. & Magn. Mater. **199**, 632 (1999).

[8] R. Fiederling, M. Keim, G. Reuscher, W. Ossau, G. Schmidt, A. Waag, and L. W. Molenkamp, Nature **402**, 787 (1999).

[9] B. T. Jonker, Y. D. Park, B. R. Bennett, H. D. Cheong, G. Kioseoglou, and A. Petrou, Phys. Rev. B **62**, 8180 (2000).

[10] J. S. Townsend, *A Modern Approach to Quantum Mechanics*, 1st ed. (McGraw-Hill Inc., NY, 1992).

[11] D. T. Pierce and F. Meier, Phys. Rev. B **13**, 5484 (1976).

[12] Y. C. Yeo, T. C. Chong, and M. F. Li, J. Appl. Phys. **83**, 1429 (1998).

[13] G. Dresselhaus, Phys. Rev. **100**, 580 (1955).

[14] J. J. Sakurai, *Modern Quantum Mechanics*, 1st ed. (Addison-Wesley, Reading, MA, 1994).

[15] S. L. Chuang and C. S. Chang, Phys. Rev. B **54**, 2491 (1996).

[16] C. J. Hill, X. Cartioxa, R. Beach, and T. C. McGill, submitted for Publication 10/2000.

[17] F. Meier and B. P. Zakharchenya, *Optical Orientation*, 1st ed. (Elsevier Science Publishers, North-Holland, Amsterdam, 1984).

Chapter 4 STM Light Emission Experiments

4.1 Motivation

The results of the previous theory section clearly define the most favorable conditions for observing spin injection into semiconductors. In order to use metallic contacts at room temperature, it is necessary to use high current densities. This obviates the problem caused by the relatively high bulk resistivity of semiconductors. It is also helpful to have a difference in the contact resistances for each spin type. This can, in principle, be achieved by using a tunnel barrier between the ferromagnet and the semiconductor. The ferromagnet's internal magnetic field lifts the internal spin degeneracy and effectively gives an offset to the bottom of the metal's conduction subbands. Because of this, an electron at the Fermi level in the spin-up subband will have different k values from an electron with the same energy in the spin-down subband. This will lead to different tunneling coefficients across the barrier and hence different contact resistances. The difference in electron density for each subband in the ferromagnet can also contribute to contact difference differentials.

An obvious choice for an experimental setup satisfying the aforementioned conditions is that provided by scanning tunneling microscopy (STM). The STM allows one to use a ferromagnetic tip to inject electrons across a tunnel barrier into a semiconductor. The efficiency of spin injection can be observed by measuring the degree of circular polarization of the electroluminescence. In order to increase the light output, a p-type semiconductor is used. An analysis of the allowed optical transitions in the semiconductor will then allow the determination of the spin injection efficiency.

STM was developed by Binnig and Roher as a vacuum technique [1]. There are very few STM experiments that work better in air than in a clean environment, where water and other contaminants cannot adhere to the tip and sample. Experiments have been performed which measure the size of water droplets formed on the surface as a function of the relative humidity [2]. These types of random contaminants can change the STM currents by a large amount [3]. This problem will be compounded in our STM electroluminescence (STMEL) studies where the light output is very sensitive to the injected current.

Light emission from STM tips has been studied in various incarnations. STM light emission (STMLE) was first observed by Gimzewski et al. [4] and Coombs et al. [5]. The visible spectrum of light emission was measured in the second experiment, where an Ir tip was used to image an Ag film. Decay of surface plasmons excited by the tunneling electrons was used to explain the origin of luminescence. This explanation was later verified by Takeuchi et al. [6] who looked at light emission from Ag evaporated on the flat of a semispherical glass prism. The angular peak in light emission coming out of the prism corresponded to that predicted by a model treating the decay of a surface plasmon-polariton mode in the metal-insulator junction [7]. The first observation of STMEL as a result of carrier injection by the tip into a semiconductor was observed by Berndt et al. into CdS [8]. Alvarado and coworkers have looked at many of the aspects of light emission from GaAs surfaces, including spontaneous linear polarization [9] and circular polarization due to spin-injection effects [10]. Alvarado's work will be discussed in detail with the experimental data presented here.

Gallium nitride (GaN) and gallium arsenide (GaAs) were the two materials chosen for STM analysis. Although indium arsenide (InAs) is very popular for its device applications, the lack of photon counting detectors capable of detecting radiation from its small band gap prohibits optical measurements at these low light levels. Although in principle any direct bandgap material with radiative recombination measurable by photon counting detectors will work, GaN and GaAs both have additional attributes which make them suitable for this work.

GaN was the first choice for the STM experiments described here. In addition to emitting at wavelengths measurable by standard photo-multiplier tubes (PMTs), it is known to have a very low density of surface states [11]. A correspondingly low surface recombination velocity will reduce signal loss due to non-radiative recombination. This is often attributed to the quality of the native oxide, Ga_2O_3, on the surface of the GaN. Although the device quality of GaN samples is a generation behind that of the other III-V semiconductors, a high defect density does not impose a significant problem for the fabrication of light emitting devices. Experiments have shown that these defects do not contribute to non-radiative recombination, perhaps through charging effects. However, the optical recombination ratios due to the wurzite crystal structure are a potential downside in using GaN in spin injection experiments at room temperature.

GaAs is arguably the most technologically relevant III-V semiconductor. However, the same problem that plagues solar cells and prevents a viable GaAs MOS technology is also a problem in the STM experiments. The high surface recombination velocity steals a lot of the optical recombination signal. Fortunately some of the same tricks that were employed for solar cells and MOS attempts can be used here. In addition, the zincblende crystal structure gives more favorable coefficients for observing circular polarization. The benefits of crystal structure were described in detail in the previous chapter.

4.2 Samples

4.2.1 Gallium Nitride

The p-type GaN sample used in the following experiments was prepared by R.A. Beach. The GaN sample was grown in a SVTA Associates BLT-N35 molecular beam epitaxy (MBE) chamber on a (0001) sapphire substrate. The 1 μm Mg doped p-layer was grown on top of 2 μm buffer layer. A thin Au film was sputtered onto the GaN surface, and windows for STM probing were opened in the Au using standard lift-off lithographic techniques. The sample was bonded to a STM sample puck with conductive silver paint. The paint was applied so that it also contacted the gold layer

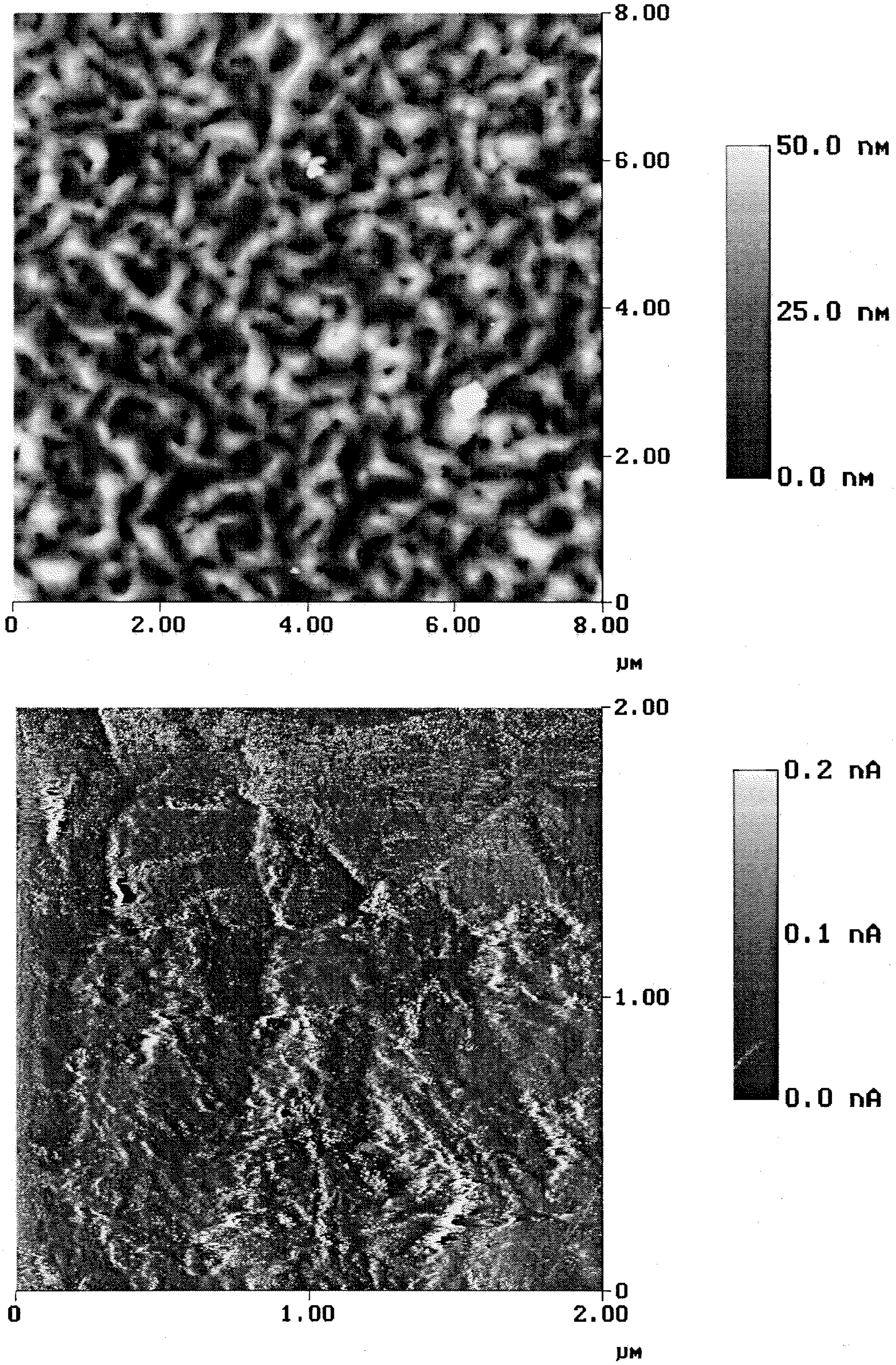

Figure 4.1: AFM (top) and STM (bottom) of pGan sample. STM image shows little resemblance to AFM image due to the low conductivity of GaN and the insulating oxide layer on top.

on top of the sample. Figure 4.1 shows an AFM and STM scan of the GaN surface, which is fairly rough by usual III-V MBE standards.

Epitaxial films of GaN have previously been studied with STM electroluminescence (STMEL) *in-situ* [12]. The purpose of such experiments are to correlate the light emission efficiency with surface morphology and defects to determine the possible insight this could lend to the design of blue light emitting devices. In another *in-situ* STMEL experiment, a spectroscopic study of the luminescence peaks was performed for Mg doped GaN layers [13].

4.2.2 Gallium Arsenide

The GaAs sample was prepared on a (001) substrate with a p-type Zn dopant density of 5x10^{18}cm^{-3}. The native oxide was removed in a Perkin Elmer 430 MBE machine and a 100 nm p-type buffer was grown with a Be doping of approximately 5x10^{18}cm^{-3}. The sample was then transferred *in-situ* to the BLT-N35 chamber for nitride passivation. The sample was heated to 350° C and exposed to a 250 W nitrogen plasma for 60 seconds in a background nitrogen pressure of 10^{-5} torr. This nitrogen flux results in growth rates on Ga rich GaN surfaces of 0.5 Å/s. We can, therefore, estimate a maximum GaN surface layer thickness of 30 Å.

After cool-down, the cathode luminescence (CL) spectra shown in the top panel of Figure 4.2 revealed a small nitride peak at approximately 400nm. The sensitivity of the detector used in the CL scans is reduced by a factor of 10 at the GaAs wavelengths as compared to the GaN, artificially making the GaN peak more pronounced. The high resolution x-ray photoelectron spectroscopy (XPS) scan shown in the bottom panel of Figure 4.2 normalized to the Ga $L_2M_{45}M_{45}$ peak also reveals the presence of nitrogen at the surface. A lowering of the relative intensities of the nitrogen 1s peak to the gallium $L_2M_{45}M_{45}$ Auger peak at higher incidence angles indicates that the nitrogen is limited to the first few monolayers.

In contrast to the GaN sample, no post-growth lithography was done on the GaAs sample. The backside of the GaAs wafer was attached to the STM sample puck with

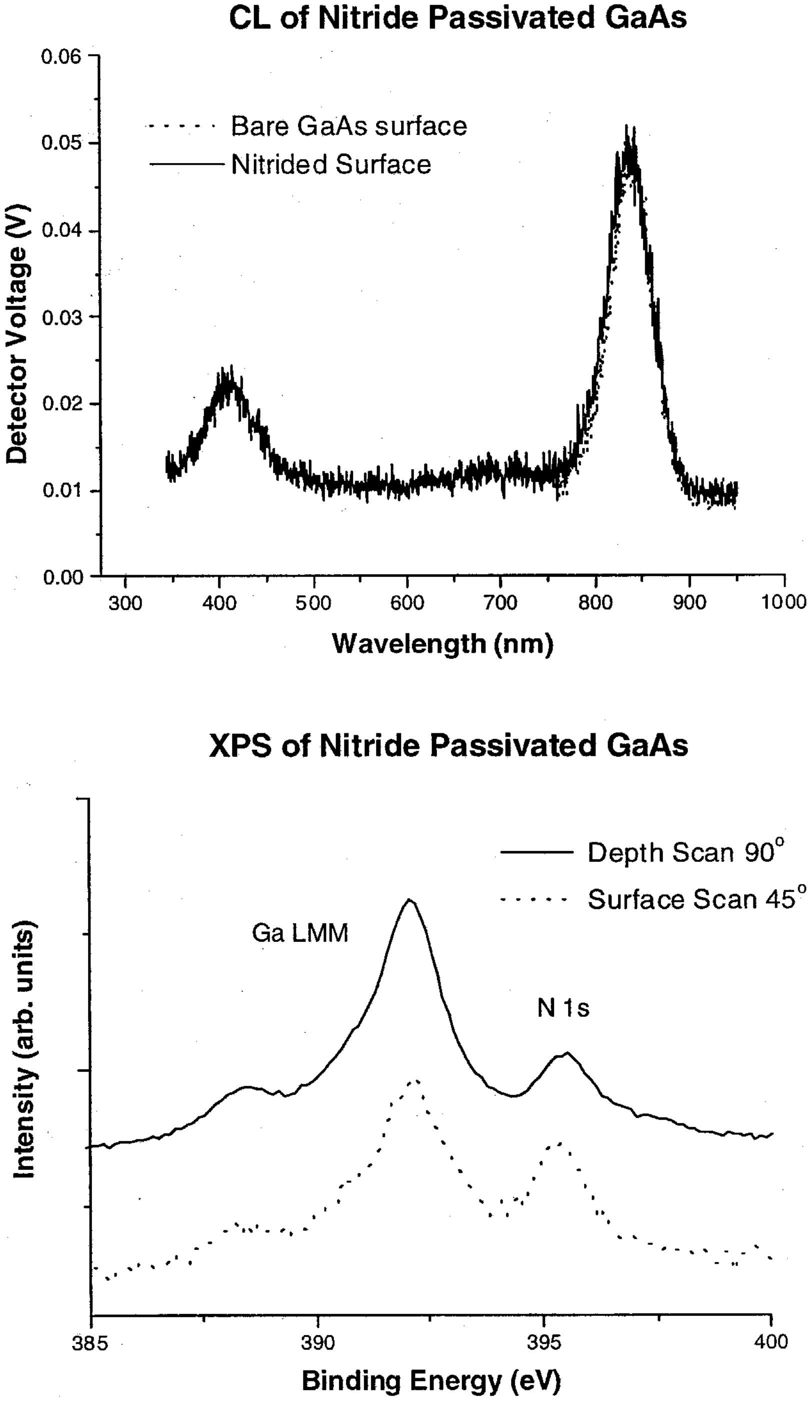

Figure 4.2: Cathode luminescence (top) and XPS (bottom) analysis of nitride passivated GaAs sample.

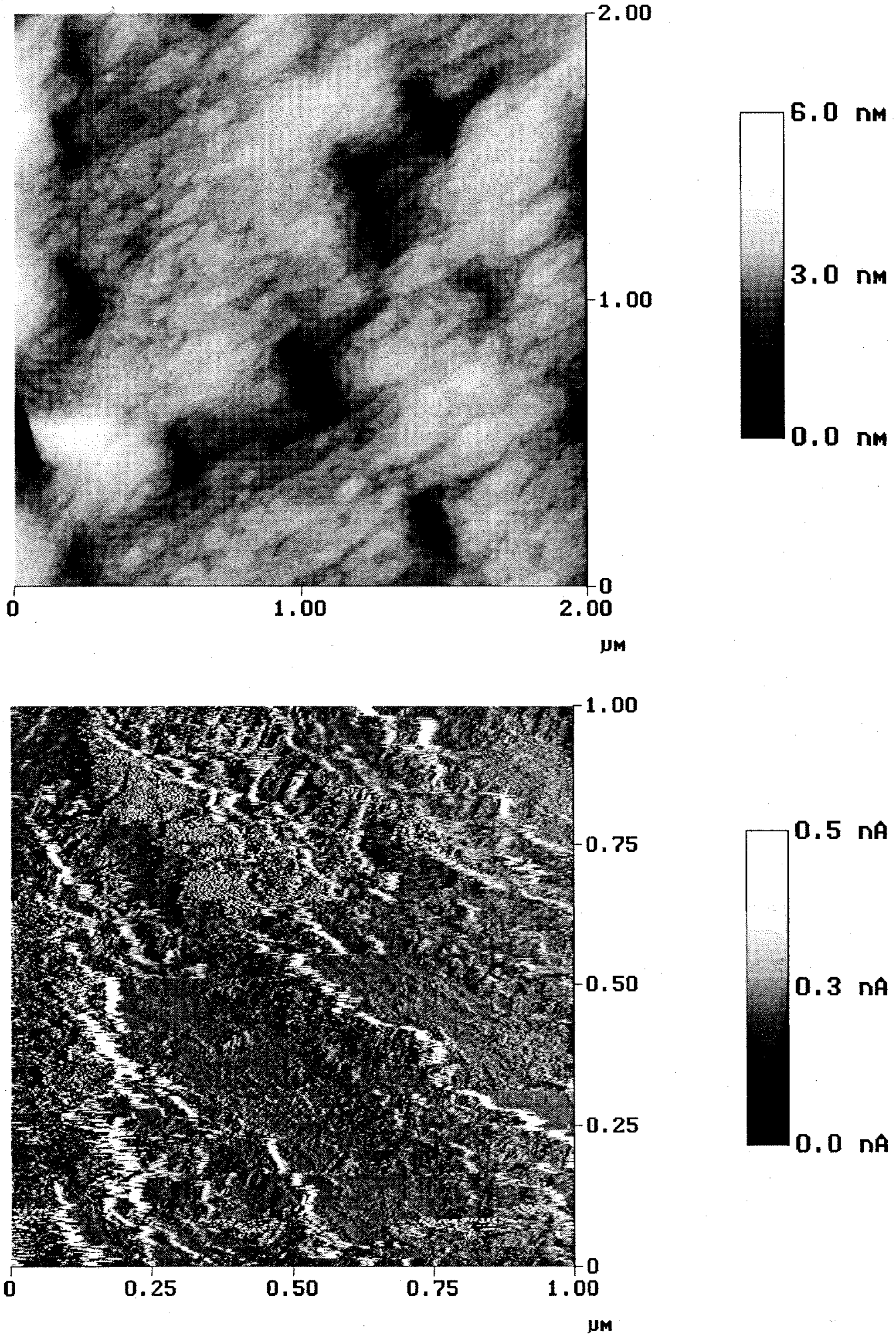

Figure 4.3: AFM (top) and STM (bottom) of nitride passivated GaAs sample. STM image shows little resemblance to AFM image due to insulating GaN and oxide layer on top.

silver paint for electrical contact. This could not be done with the GaN due to the insulating sapphire substrate.

When using GaAs surfaces for light emission in air, passivation techniques are essential. We have found that STM light emission from bare GaAs substrates is very difficult to achieve. The earliest reports of STMLE from GaAs surfaces in ambient conditions was reported by Wenderoth et al. [14]. In their experiments GaAs was cleaved *in-situ* and thin layers of gold were thermally evaporated onto the surface. This enabled them to take STM topographical scans of the surface and determine threshold currents for light emission. They were able to obtain an efficiency of a few counts per second per nanoampere of tunnel current. Later, Reuter et al. [15] compared STM light emission efficiency from GaAs with different surface passivations. They were able to get a small amount of light out of bare GaAs surfaces as well, although passivated surfaces showed up to 57 times greater luminescence. A more recent experiment by Carladous et al. [16] used a paraffin passivated GaAs surface to obtain STMEL spectra and rudimentary photon surface mappings. In this work efficiencies of tens of photons per nanoampere were achieved, similar to the efficiencies we see in our experiments.

Nitridization of GaAs surfaces has been studied by several groups. Early in the development of GaN technology, nitrogen ion bombardment of GaAs was used as a possible growth mechanism of GaN films [17]. Vogt et al. [18] used hydrazine to nitride the surface of GaAs. Although XPS studies revealed that Vogt's surface was still contaminated by water and oxygen, he was still able to show an improvement in photoluminescence (PL) intensity. This was interpreted as resulting from a lower surface state density from improved termination of dangling bonds at the surface. These types of experiments have been repeated with UHV prepared samples with similar increases in PL intensity [19]. More recently, Tanemura et al. [20] looked at plasma damage, annealing and ambient exposure effects on nitride passivated GaAs MIS diodes. The density of papers in this area is rapidly increasing due to the technological benefits of passivated GaAs and the increasing availability of UHV nitride chambers.

4.3 Experimental Setup

The STM experiments used a Digital Instruments MultiMode scanner equipped with a top-view STM head. The experimental setup is shown schematically in Fig.4.4. Light emitted from the semiconductor was collected directly above the sample with a Nikon Alphaphot microscope. The microscope is equipped with a base designed to isolate it from vibrations from the optical bench. The light collected by the microscope lens is piped to a thermoelectrically cooled Hamamatsu R943-02 photo multiplier tube (PMT) via a light guide attached to the Nikon's camera port. Counts were recorded with a Stanford Research Systems SR400 dual-gated photon counter. Emission spectra were taken by mounting the entrance slit of a CVI Laser CM-110 monochromator on the Nikon's camera port and attaching the light pipe to the exit slit. For the spectral measurements a Stanford Research Systems SR540 optical chopper was used to chop the signal and trigger the gates on the SR400.

Circular polarization was measured by placing a quarter wave ($\lambda/4$) plate and a linear polarizer between the microscope lens and the STM tip. For the GaN experiments, a Melles Griot dichroic sheet polarizer with a range of 300-650 nm and a Alphalas Gmbh. tunable quarter wave plate were used. For GaAs, a Melles Griot NIR polarizer with a range of 750-1200 nm and the quarter wave plate was a standard broadband quartz $\lambda/4$ plate with a center at 850 nm from Newport Optics. A Micos rotation stage with a 50 mm clear aperture was used to change the position of the polarizer or quarter wave plate to select the two different types of circular polarization.

PC data acquisition was automated with National Instruments Labview software controlling the positions of the rotation stage and monochromator, as well as the counting cycles of the SR400.

Control experiments and luminescence spectra were taken with standard PtIr STM tips available from Digital Instruments. The ferromagnetic tips for injection experiments were fashioned from 10 mil iron, cobalt, and nickel high-purity wire purchased from Alfa Aesar. All homemade tips tested were able to produce atomic resolution

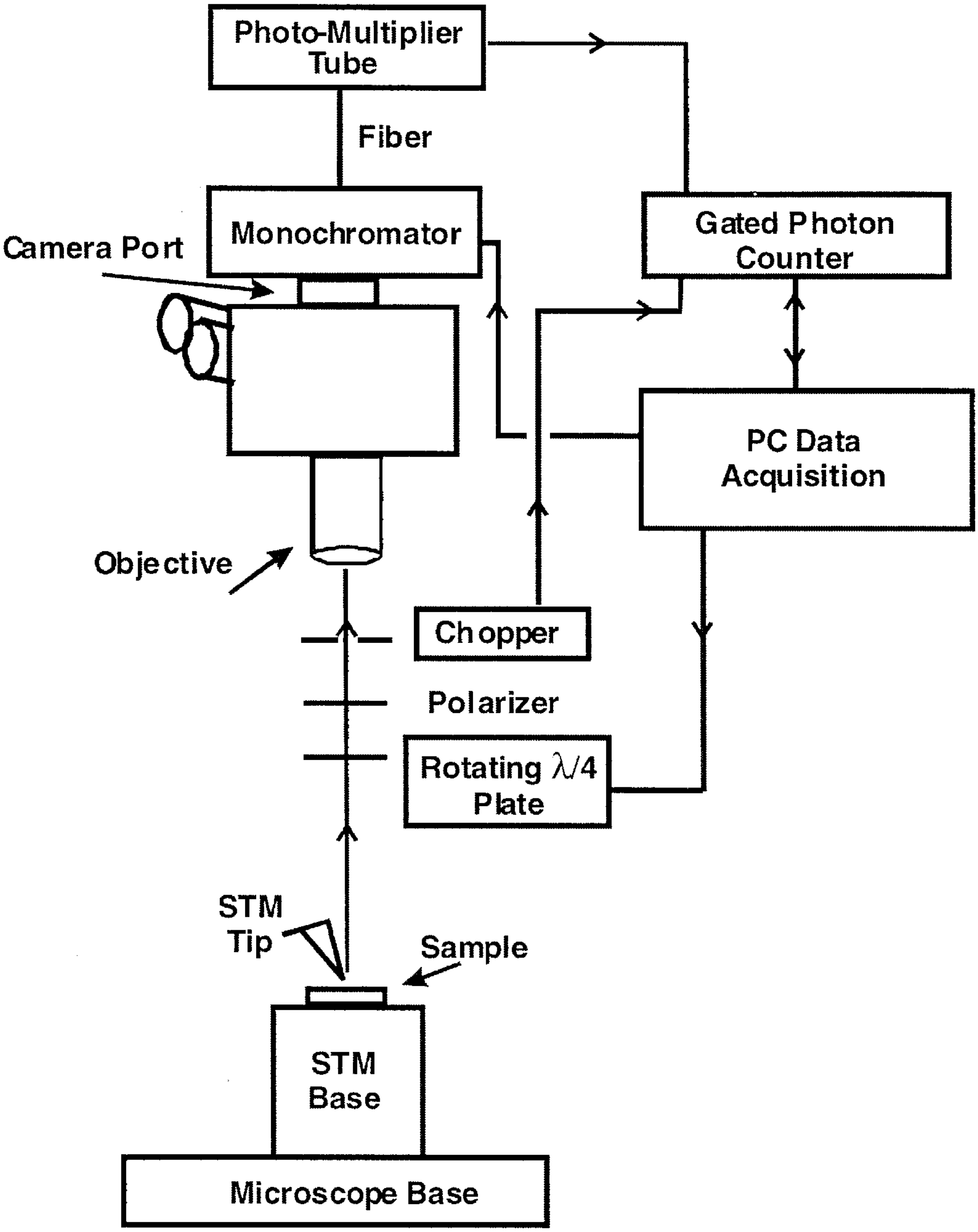

Figure 4.4: Schematic of the STM Light Emission Experiments

images on highly-ordered pyrolytic graphite (HOPG) samples. The magnetic tips were placed in a 0.6 Tesla magnetic field in order to align their magnetization either parallel or antiparallel to the tip axis for spin injection experiments. In the GaAs experiments, tip magnetization was checked before and after injection experiments with a Lakeshore model 421 Gaussmeter to insure that the magnetization was not affected by tip heating or the 40 Oe field above the STM base. This field points downwards and can have the effect of partially canceling or reversing the magnetization of a tip prepared with magnetization pointing away from the sample.

Maximum scanning currents with the DI multimode STM used are on the order of 1 nA. At these current levels no detectable amount of luminescence was observed. In order to achieve a detectable amount of light, the STM was operated in an IV mode where the tip-sample separation is (ostensibly) held constant and the tip-sample bias is swept. After every sweep, the feedback loop adjusts the tip-sample separation to meet normal current and voltage setpoint values in the allowed scanning ranges. Due to the exponential nature of the IV curve, currents which are orders of magnitude larger than the maximum scanning currents are attainable in this mode. As an example, one could set the feedback loop to maintain a separation that gives a current of 40 pA at a bias of 4 V. The IV loop can then ramp the bias up to 7.5 V while holding the separation constant. In this and all subsequent sections, a positive bias of 4 V indicates that the sample is biased 4 V above the grounded tip, so that electrons are injected into the sample from the tip.

The most unfortunate drawback of this technique is that the DI controller can no longer measure the actual current going through the tip. The current must be extrapolated from the light intensity data or by independent measurements. STM luminescence experiments in ambient conditions are plagued by uncontrollable drift in the total intensity. This is exacerbated in the experiments presented here because the DI electronics do not allow the current setpoint to be above 1 nA. This drift was circumvented in the polarization measurements by making measurements on a time scale smaller then the overall intensity drift.

4.4 Device Considerations

In the STM experiments we have a p-type metal-insulator-semiconductor (pMIS) structure, with the vacuum barrier acting as the insulator. In order to inject electrons from the tip into the semiconductor, the tip is fixed at ground and the semiconductor is placed at positive bias. In this configuration the bands bend upward at the semiconductor surface, increasing the concentration of holes. When speaking in terms of MIS diodes, this is known as accumulation mode.

A tunneling drift diffusion simulation program, written by Daniel [21], was used to generate the plots in Figure 4.5, which show the electron and hole current densities for the bias conditions used in the STM experiments as a function of insulator width. If the tip were in contact with the sample, we would have a simple p-type Schottky barrier, and all of the current would be carried by holes. This is the case when the tunnel barrier approaches zero. As the tunnel barrier widens, the bias allows preferential injection of electrons into the semiconductor conduction band. Since optical recombination rates vary as the product of carrier densities, these curves predict a peak in light emission for very small tunneling distances, 1 Å and 5 Å for GaAs and GaN, respectively. For larger barrier widths the behavior is the same but the device becomes more resistive, and the overall current drops.

4.5 Luminous IV Curves

Commercially available PtIr STM tips were used to characterize the current-voltage characteristics of the samples. Nearly all of these tips give light emission from GaN and passivated GaAs. It is difficult to keep the intensity stable for long periods of time. An intensity drift will be apparent in all of the circular polarization measurements, and this problem is even worse with handmade tips. Low count levels are very problematic. No light emission is detectable at normal scanning currents, which are below 1 nA with the STM used in our experiments. There are, however, several ways to get more current from the STM. The first is to use a sample and hold

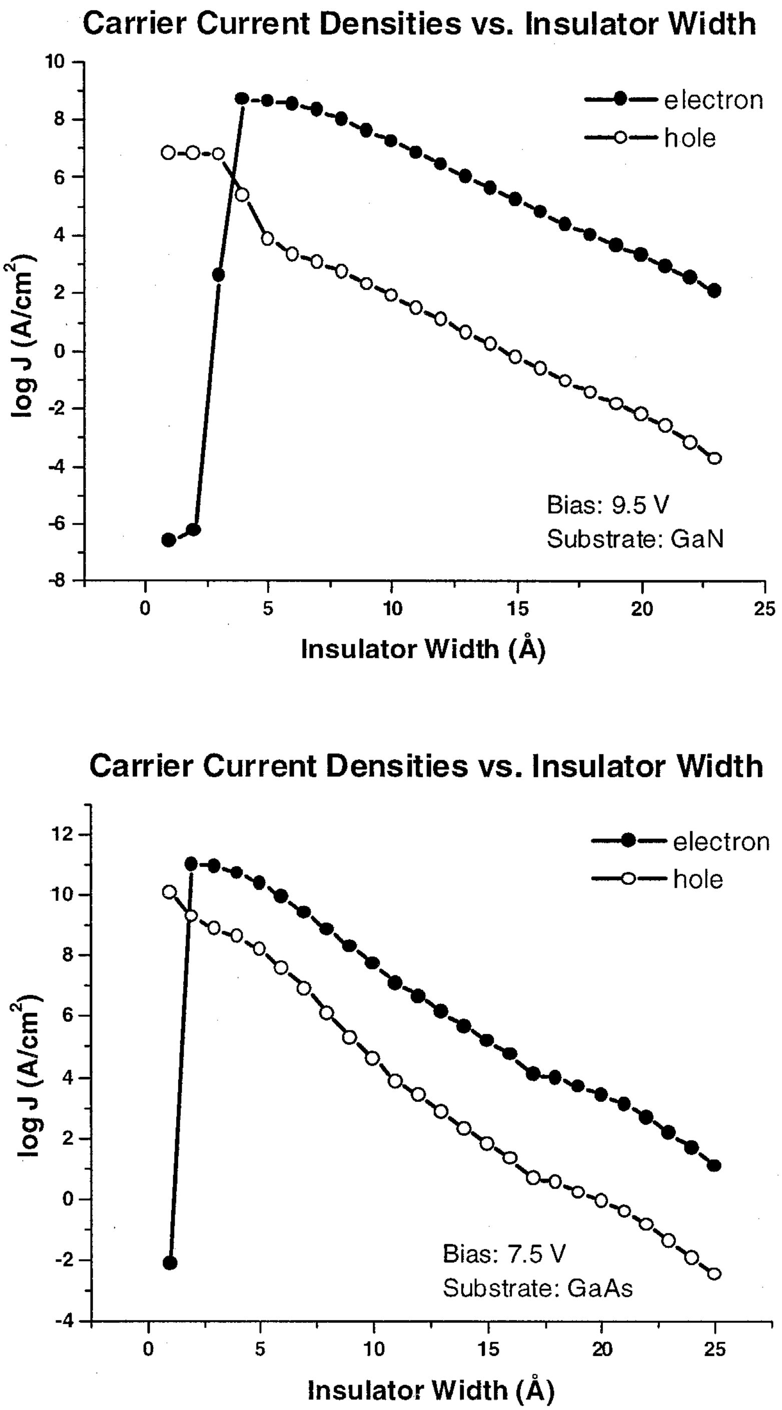

Figure 4.5: Calculated tunneling current densities for GaN (top panel) and GaAs (bottom panel) as a function of barrier width for the bias conditions used in our experiments.

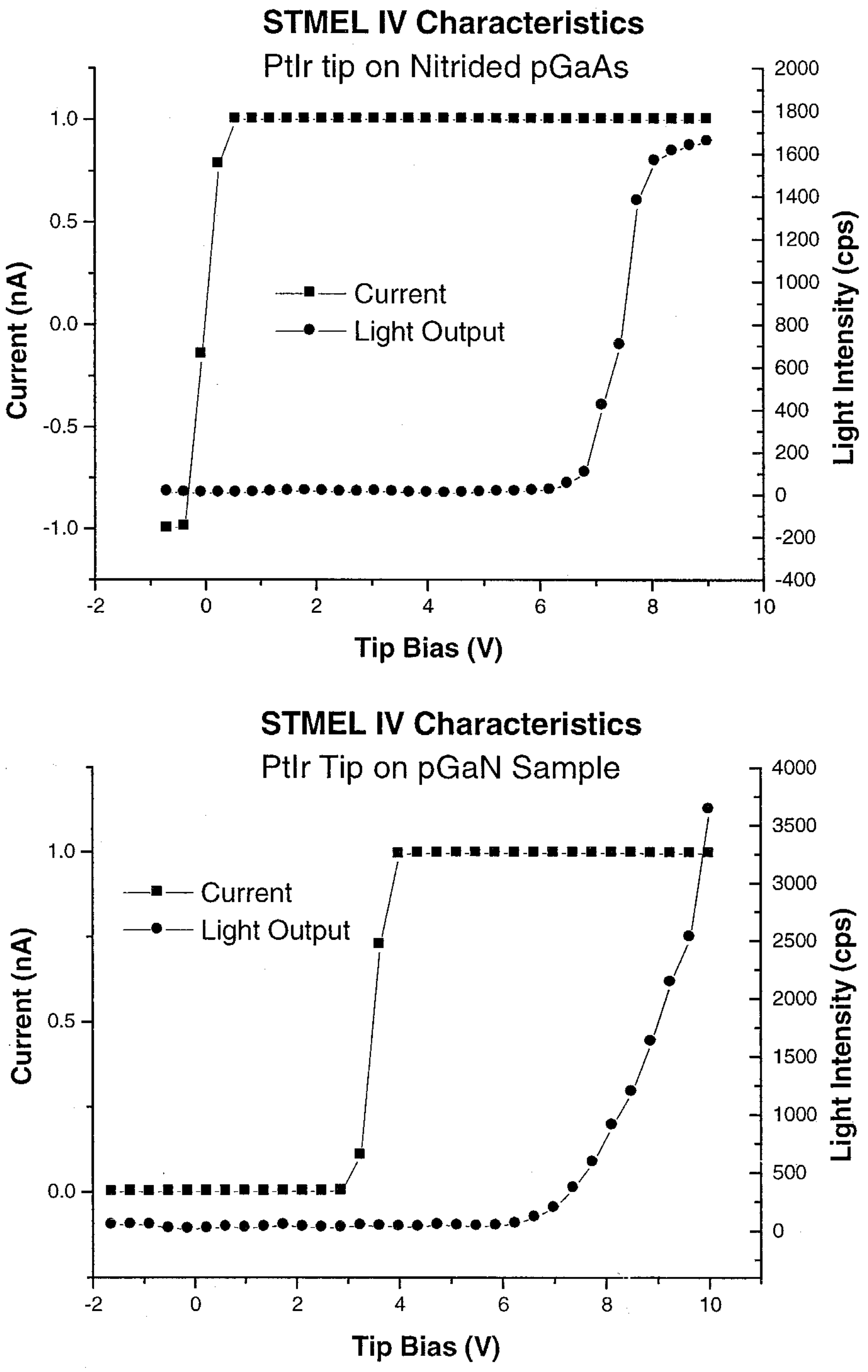

Figure 4.6: STM luminescence intensity versus tip bias for GaAs (top) and GaN (bottom).

method, where the scanning feedback parameters are used to maintain the tip at a fixed distance above the sample. Then the tip bias is ramped above the setpoint value. Current increases exponentially and goes out of the DI controller's measurable range very quickly. Once the current reaches a high enough value, a detectable amount of light is emitted.

This process is shown in Figure 4.6 for GaAs. The figure shows a bias ramp from -1 to 9 V with the DI controller measuring current and the SR400 counting photons. It can be noted from the figure that the DI stops keeping track of current above 1 nA. For GaAs the onset of detectable emission is around 5 V, continues to increase exponentially until around 7.5 V, and then appears to enter an Ohmic regime where intensity increases linearly with bias. Similar behavior is observed with the GaN sample, although the onset of counts occurs at a higher bias, approx 7 V. These curves are quite insensitive to the actual feedback parameters due to the exponential nature of the tunneling process. Attempting to change the tip-sample separation by adjusting the feedback parameters can affect the maximum amount of light output, up to approximately 5000 counts per second. Estimating the actual current from these graphs gives maximum currents on the order of 1 μA.

We do not have the vertical control necessary to try and reproduce the theoretical plots shown in figure 4.5. This has been attempted by using a mode where the STM changes the tip-sample separation at constant bias. This method has never given light.

4.6 Control Spectra

STM electroluminescence spectra were taken with PtIr tips. The introduction of the CVI Laser CM110 monochromator into the optical path considerably lowers the amount of light incident on the PMT. Due to the low light levels, photon counting techniques were employed. The luminescence signal was chopped at 200 Hz with a Stanford Research Systems SR540 optical chopper. Counts measured with the light blocked by the chopper are subtracted from those taken with the chopper wheel open.

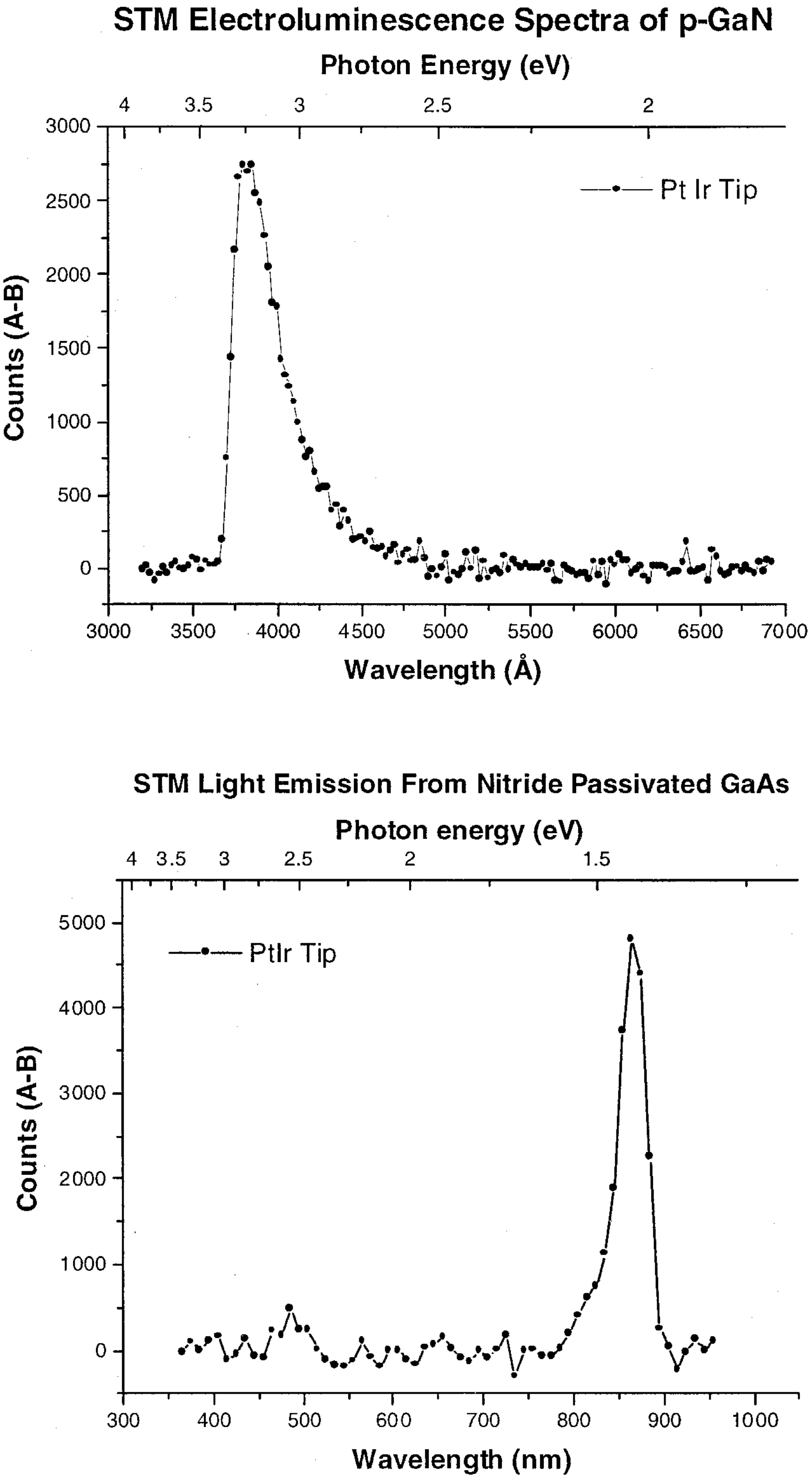

Figure 4.7: Luminescence spectra for light emission from GaN (top panel) and passivated GaAs (bottom panel)

The main source of noise in this experiment are the dark counts from the PMT, which tend to be around 10 counts per second. Since is it known that light can be emitted in STM experiments from tip-induced plasmon modes when both tip and sample are metals [7, 6], these luminescence spectra assure us that we are making measurements of the correct light emitting process.

The luminescence spectra are shown in Figure 4.7, with each point corresponding to a count period of 10 minutes. The top panel for the GaN sample shows that all of the intensity incident on the detector is due to near band edge transitions in the GaN. GaN is often prone to yellow luminescence when doped p-type, and light from below the band edge may not retain information about the spin of the electron that began the process. The bottom panel shows the results for the passivated GaAs sample. The largest peak is due to near band-edge recombination in the GaAs, with a smaller peak near 480 nm due to the thin layer of GaN formed at the surface.

4.7 Photon Mappings

A second method for producing large currents with the DI STM is to operate in lift mode. In this mode a second scan line is taken for each pass made at normal feedback parameters. The surface height is calculated by the first pass. The tip is then lifted to a user defined height above the surface and the tip bias is adjusted anywhere in the -10 to 10 V range allowed by the controller. This enables light emission similar to the spectroscopic mode used for the IV curves. This technique allows photon emission maps of the surface to be recorded. Unfortunately, the STM's ability to accurately track the oxidized surface features is fairly poor, as shown in Figures 4.1 and 4.3. Thus far we have only been successful in imaging random points of light on the GaAs surface with this method.

Bibliography

[1] G. Binnig, H. Rohrer, C. Gerber, and E. Weibel, Phys. Rev. Lett. **50**, 120 (1983).

[2] J. Freund, J. Halbritter, and J. Horber, Microsc. Res. Techniq. **44**, 327 (1999).

[3] W. Schmickler, Surf. Sci. **335**, 416 (1955).

[4] J. K. Gimzewski, J. K. Sass, R. R. Schlitter, and J. Schott, Europhys. Lett. **8**, 435 (1989).

[5] J. H. Coombs, J. K. Gimzewski, B. Reihl, J. K. Sass, and R. R. Schlittler, J. Micros-Oxford **152**, 325 (1988).

[6] K. Takeuchi, Y. Uehara, S. Ushioda, and S. Morita, J. Vac. Sci. Technol. B **9**, 557 (1991).

[7] Y. Uehara, Y. Kimura, S. Ushioda, and K. Takeuchi, Jpn. J. Appl. Phys. 1 **31**, 2465 (1992).

[8] R. Berndt, R. R. Schlittler, and J. K. Gimzewski, J. Vac. Sci. Technol. B **9**, 573 (1991).

[9] S. F. Alvarado, H. Riechert, and N. E. Christensen, Phys. Rev. Lett. **55**, 2716 (1985).

[10] S. F. Alvarado and P. Renaud, J. Appl. Phys. **73**, 5816 (1993).

[11] P. Bridger, Z. Bandic, E. Piquette, and T. McGill, Appl. Phys. Lett. **74**, 3522 (1999).

[12] J. Ma, B. Garni, N. Perkins, W. L. Obrien, T. F. Kuech, and M. G. Lagally, Appl. Phys. Lett. **69**, 3351 (1996).

[13] M. Ortsiefer, A. Liebheit, M. Schwartzkopff, P. Radojkovic, T. Gabriel, and E. Hartmann, Appl. Phys A-Mater. **66**, S371 (1998).

[14] M. Wenderoth, M. J. Gregor, and R. G. Ulbrich, Solid State Commun. **83**, 535 (1992).

[15] E. E. Reuter, S. Q. Gu, P. W. Bohn, J. F. Dorsten, G. C. Abelin, J. W. Lyding, and S. G. Bishop, Proc. MRS Spr. Meet. (1995).

[16] A. Carladous, R. Coratger, G. Seine, F. Ajustron, and J. Beauvillain, J. Appl. Phys. **84**, 1085 (1998).

[17] L. A. Delouise, J. Vac. Sci. Technol. A **10**, 1637 (1992).

[18] K. W. Vogt and P. A. Kohl, J. Appl. Phys. **74**, 6448 (1993).

[19] S. Anantathanasarn, S. Ootomo, T. Hashizume, and H. Hasegawa, Appl. Surf. Sci. **159**, 456 (2000).

[20] H. Tanemura, K. Kanazawa, and H. Ikoma, Jpn. J. Appl. Phys. 1 **39**, 1629 (2000).

[21] E. S. Daniel, X. Cartoixa, W. R. Frensley, D. Ting, and T. C. McGill, IEEE T. Electron Dev. **47**, 1052 (2000).

Chapter 5 Magnetic STM Experiments

5.1 Chronology

We developed the technique on GaN due to the ease of producing samples with large recombination luminescence. The ability to inject spin polarized currents into GaN was demonstrated. However, the small circular polarization allowed by the GaN band structure makes decoupling the circular polarization signal from other possible tip-dependent effects difficult. For this reason, we later moved to GaAs for the larger theoretical circular polarization signal. However, unpassivated GaAs samples failed to produce light emission in the STM setup. The passivated GaAs samples gave light but proved more difficult than GaN to demonstrate spin injection.

5.2 Gallium Nitride

All circular polarization experiments on GaN were performed by collecting the luminescence directly above the sample along the z axis. The tip holder is inclined at a 13° angle to the z axis, allowing for observation of the tip-sample interface without complete shadowing of the luminescence by the tip. The $\lambda/4$ wave plate was held in fixed position, while every 30 s the analyzer was rotated 90° to alternately measure the intensities of left and right circularly polarized light. This method is not as robust in terms of being influenced by linear polarizations as compared to holding the analyzer fixed and rotating the $\lambda/4$ wave plate. Both methods are explained in detail in the appendix. The second method was not available in the GaN experiments, because the face of the $\lambda/4$ wave plate used is not perpendicular to the z axis when tuned to 380 nm. Rotating the $\lambda/4$ wave plate would then rotate the image in the collection optics giving a false signal. One additional complication could arise from the polarization sensitivity of the PMT. This was obviated through the use of a liquid light pipe between the microscope and PMT which did not preserve the polarization of the input beam.

After a tip is loaded into the holder it is scanned along the surface to clean the tip of water or other contaminants, and then the STM is switched to IV mode for high current injection. During data collection the tip was grounded and the substrate biased at 9.5 V. Every second the bias was swept 100 mV about the 9.5 V bias. The feedback loop maintained the tip-sample separation with setpoint biases and currents of 5 V and 500 pA, respectively. This setup allowed for up to 3000 counts per second on the PMT. Often the luminescence intensity was very unstable on the 30 s timescale. However, if allowed enough time, the counts would stabilize for intervals on the order of several minutes to hours. The control experiment with a PtIr tip is shown in Figure 5.1. These and all subsequent graphs of the raw data show the total number of counts collected over a 30 s interval with the analyzer set to measure the intensities of either RCP or LCP light. The degree of circular polarization, also known as the normalized Stokes parameter V, is taken as the difference of successive measurements of right and left circularly polarized intensities over the sum of the two, or

$$V = \frac{I_{RCP} - I_{LCP}}{I_{RCP} + I_{LCP}}. \tag{5.1}$$

Values of V are reported as the mean of measurements taken when the intensity is relatively constant, with error bars indicating the standard deviation of the data around the mean. For this PtIr control tip, the degree of circular polarization is -0.0035 ± 0.0091, which is essentially zero within the error of measurement. At no point during the data collection was a systematic difference between LCP and RCP intensities observed. This is not a guarantee that net circular polarization of the STMLE cannot occur with a PtIr tip. In the GaAs samples, a significant degree of circular polarization can sometimes be seen even with PtIr tips. What the control data here does show is that there is no net circular polarization for this tip and that rotating the linear polarizer does not contaminate the CP signal with a preferential transmission of one linear polarization over the other through the portion of the

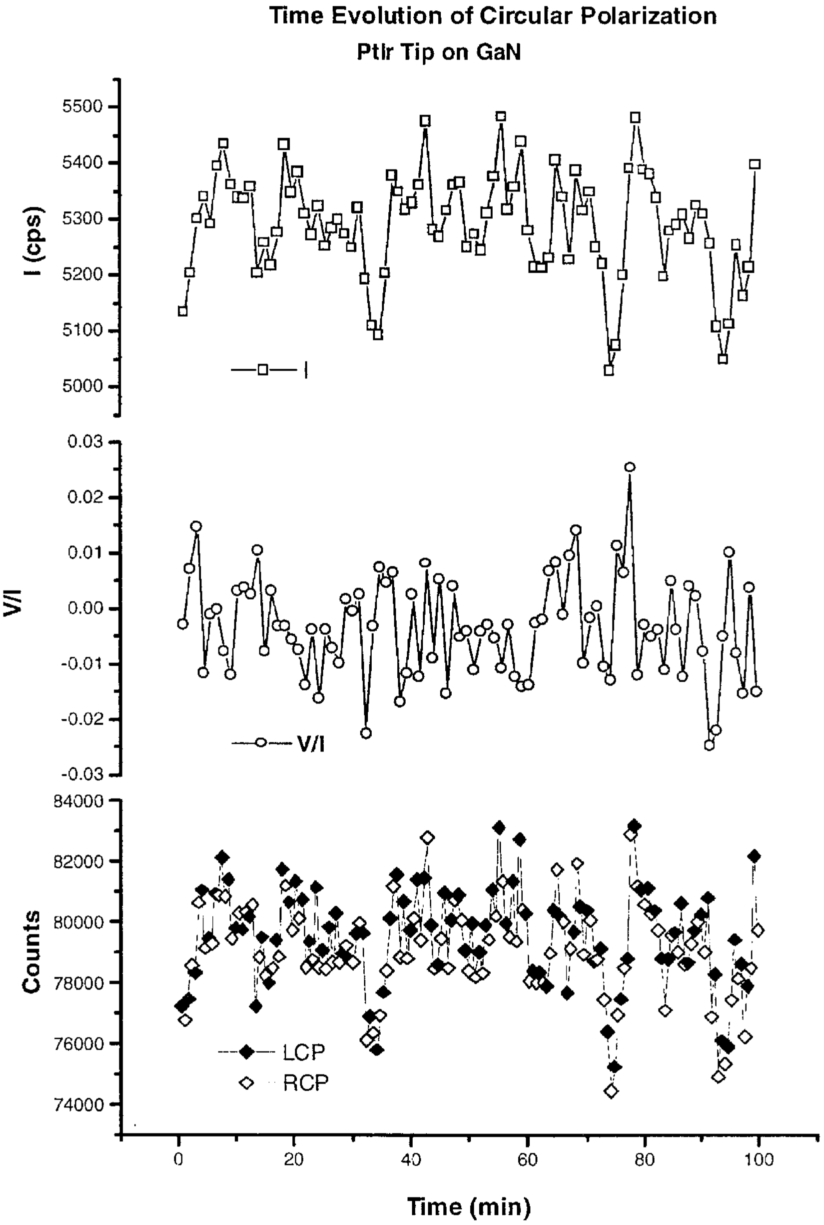

Figure 5.1: Raw Data for PtIr on GaN. Intensity (top) and normalized Stokes parameter V (center) for PtIr tip on GaN. Lowest panel shows the raw data for successive measurements of RCP and LCP.

optical train after the analyzer.

Before magnetic measurements were taken, the ferromagnetic tip was placed in a ceramic tip holder and placed in an electromagnet where the field was ramped up to 0.6 T to magnetize the tip either parallel or antiparallel to the tip axis. Here, parallel is taken to mean the magnetization is along the tip axis pointing towards the tapered end of the tip. Antiparallel means the magnetization is along the tip axis pointing away from the tapered end of the tip. The field is then ramped down to zero and the tip is removed from the electromagnet and placed in the STM tip holder. Details of the magnetic tip preparation techniques are given in the appendix.

The initial experiments on Ni and Co were done before the purchase of the Micos rotation controller. Therefore, the rotation of the analyzer had to be performed by hand. After the tip had been scanned across the surface for several minutes, the controller was switched to IV mode and feedback parameters were adjusted until the luminescence intensity stabilized. This process could take several minutes to a few hours. At this point data acquisition was initiated. The PC was instructed to provide an audible beep at 30 s intervals to signal the end of a data acquisition period. A five second pause was then given for the manual adjustment of the analyzer. This process was repeated throughout the data acquisition, limiting the time of the experiment to the stamina of the operator. The first experiments with Ni on GaN showed a small amount of circular polarization in the STM luminescence that changed sign upon reversal of the magnetization. This was meant as a proof of concept measurement. The amount of circular polarization was very small, and the drift in the total intensity exacerbates the problem of seeing clear trends in the data. The data from the initial Ni experiment (Ni Tip A) is shown in the top panel of Figure 5.2. The data shows a clear difference in the values of circular polarization for magnetizations along z (-0.0150 ± 0.0116) and $-z$ (0.0276 ± 0.0055). This was our first indication that magnetic tips were having an effect on the circular polarization of the STM luminescence.

It rapidly became clear that tips would not in general survive multiple trips to the magnet. To circumvent this problem, in many experiments each tip was cut with

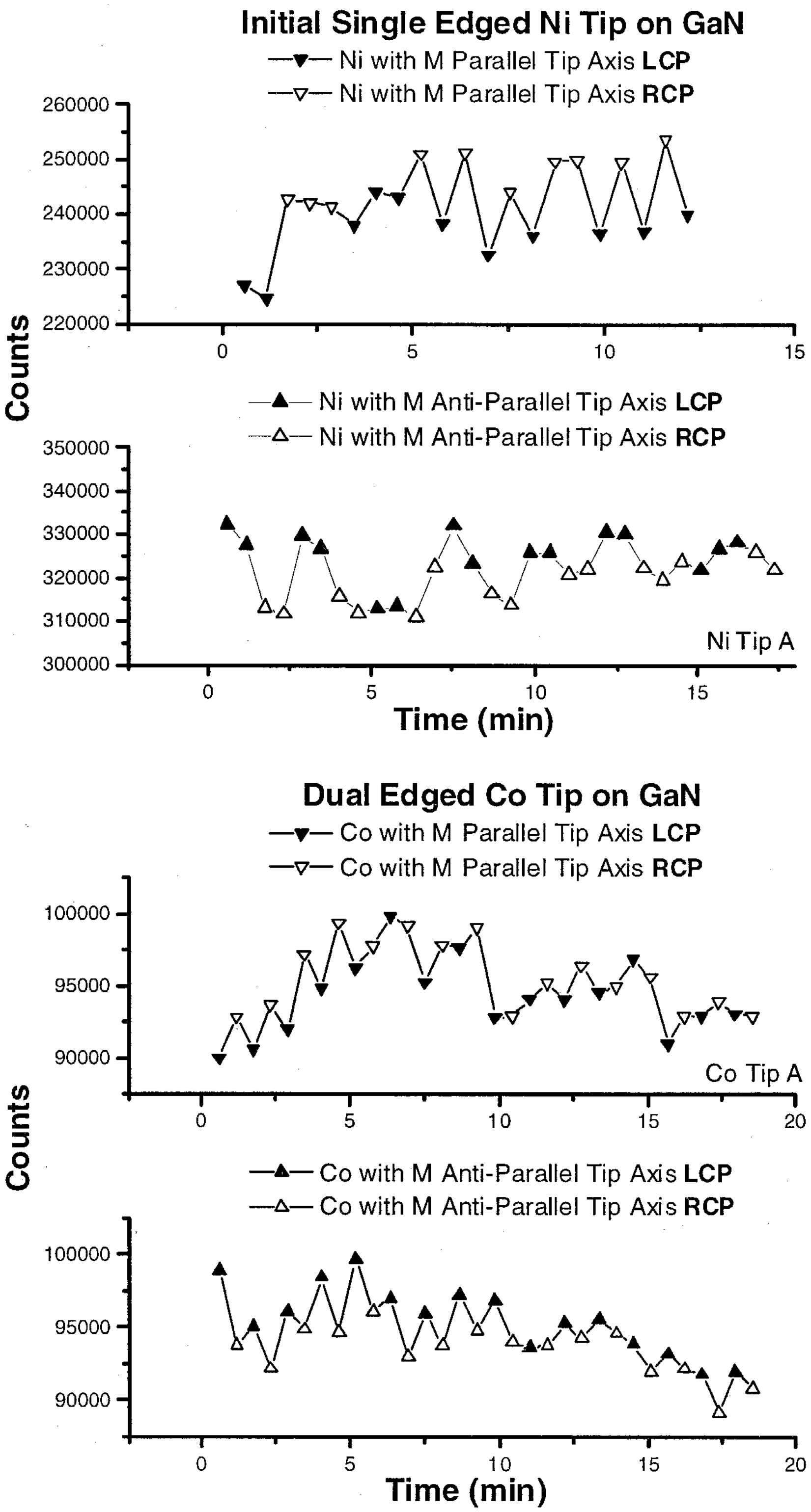

Figure 5.2: Raw Data for initial Ni(Top) and Co (bottom) on GaN. Magnetization of tip is parallel to tip axis, along $-z$, in the upper half of each plot, and along $+z$ in the lower half. Each panel shows the raw data for successive measurements of RCP and LCP.

an edge on both sides, so that only one trip to the magnet was necessary. In order to perform experiments with opposite magnetization direction, the tip was flipped in the holder. This should also help keep the magnitude of the magnetization the same for a given tip. Unfortunately, this method is vulnerable to overlooking any component of circular polarization that is due to tip geometry. Raw data from a double-edged Co tip (Co Tip A) is shown in the bottom panel of Figure 5.2. It too exhibits clear changes in the sign of the circular polarization with the sign of the magnetization.

After the arrival of the rotation controller, more nickel tips were characterized. The rotation controller allowed the experiments to be performed for several hours. At some point during the data acquisition the intensity would stabilize for enough time to get accurate measurements of the circular polarization. For completeness, the raw data from these experiments with single edged tip Ni B and double edged tip Ni C is shown in Figure 5.3. Circular polarization changes with magnetization were again observed, but the effect was opposite to that observed with the first magnetic experiment. The second and third tips tested both agreed in sign, opposite to the first. We presume that this is due to a mistake made in magnetizing the first tip. It was discovered that if the power supply to the magnet is shut off before tip removal with any measurable current flowing, a pulse of current in the other direction ensues. This can serve to reduce or even flip the magnetization of the tip. As the idiosyncrasies of the magnet were not well understood at the time this first set of data was taken, it is possible that the tips were incorrectly magnetized. The third tip also did not produce very stable circular polarization for the magnetization in the $+z$ direction. This is possibly due to the low Curie temperature of nickel (350°C), and our inability at the time to test the magnetization state of the tip before and after measurements were taken. With the currents we are sending through the tips, it is possible that changes in temperature at the apex on the order of 100°C or more are possible, making demagnetization of the Ni tip a very real possibility.

These problems prompted us to focus our efforts on tips with higher Curie temperatures. Both iron and cobalt have $T_c > 1000$°C. The results of magnetic experiments with a double-edged iron tip (Fe Tip A) is shown in Figure 5.4. The data shown are

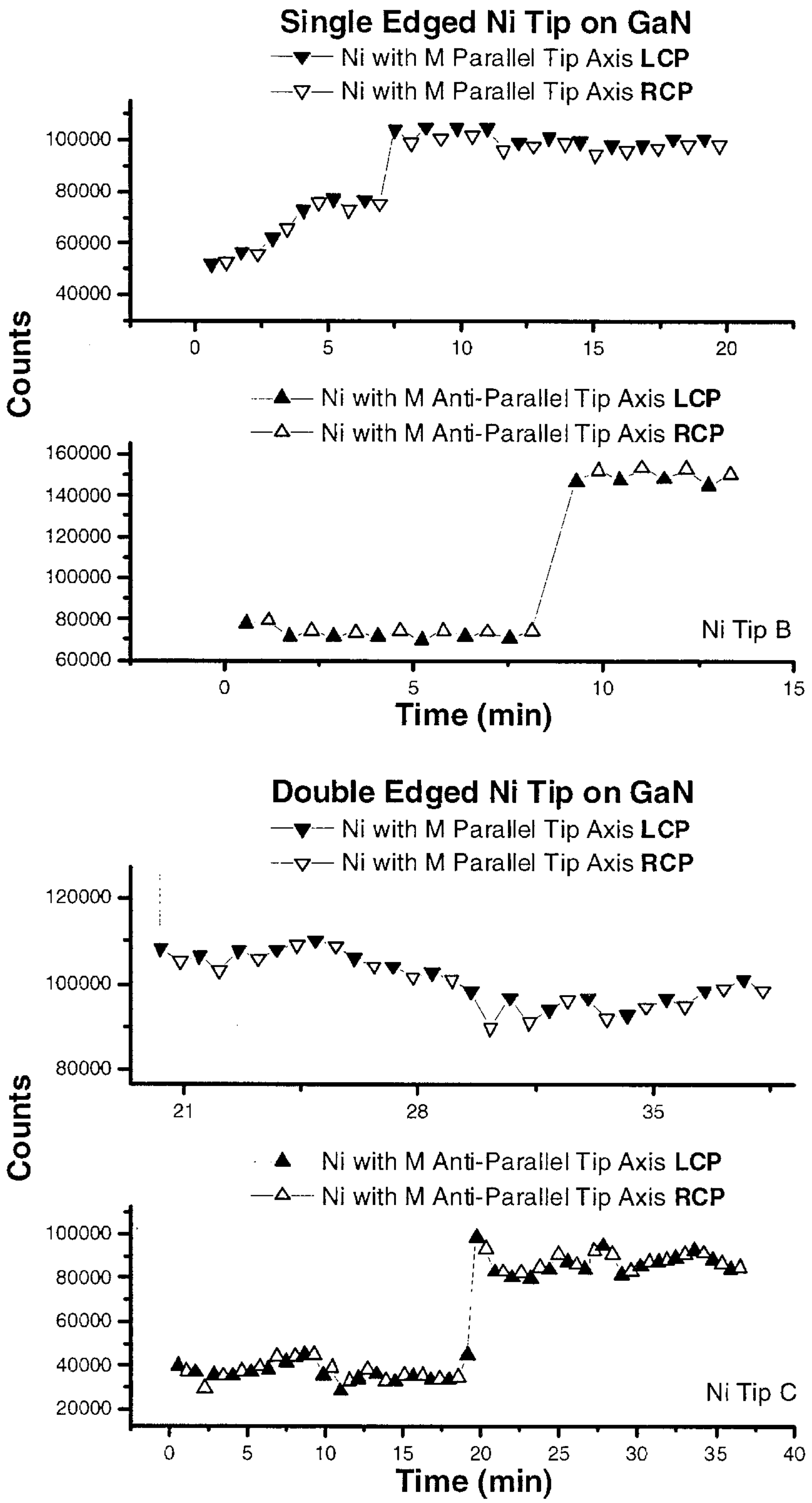

Figure 5.3: Raw Data for single (top) and double (bottom) edged Ni tips on GaN. Magnetization of tip is parallel to tip axis, along $-z$, in the upper half of each plot, and along $+z$ in the lower half. Each panel shows the raw data for successive measurements of RCP and LCP.

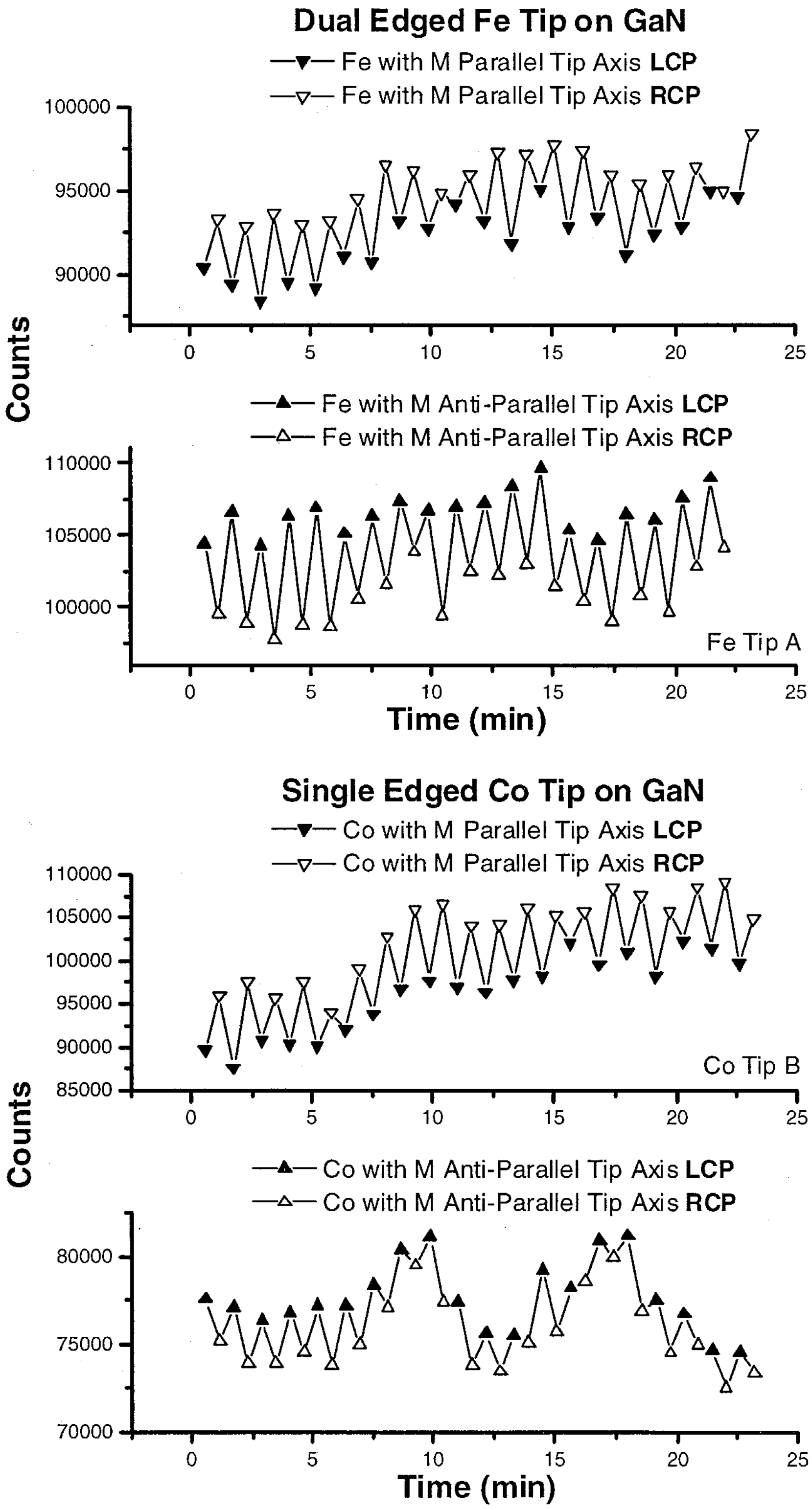

Figure 5.4: Raw Data for Co(Top) and Fe(bottom) on GaN. Magnetization of tip is parallel to tip axis, along $-z$, in the upper half of each plot and along $+z$ in the lower half. Each panel shows the raw data for successive measurements of RCP and LCP.

for 25-minute periods, where the total intensity was relatively constant. Each panel shows alternating measurements of LCP and RCP counts for a given tip material and magnetization. When the magnetization is parallel to the tip axis, the RCP signal is stronger. When the magnetization is reversed to the antiparallel orientation, the LCP signal is stronger. The sign of the circular polarization does indeed reverse with magnetization. The data shows a mean circular polarization of 1.8% when the magnetization is down and -2.8% when the magnetization is up. A similar experiment with a Co tip (Co Tip B) is shown in the bottom panel of Figure 5.4. This time the tip is single-edged, and therefore had to be magnetized twice. The results are in qualitative agreement with those from Fe Tip A and Co Tip A. The data shows a mean circular polarization of 3.6% when the magnetization is down and -1.5% when the magnetization is up. This experiment is important because it uses the same tip edge for each magnetization.

These experiments are viewed as successful injection of spin-polarized current into the GaN. However, large relative changes in the magnitude of the effect argue that we are seeing more than just the effects of spin injection. It is possible that the part of the circular polarization seen is due to tip asymmetries. Because of these types of concerns, we invested heavily into getting light out of GaAs, where in theory much larger circular polarizations can be seen.

5.3 GaAs Experiments

Data was taken on the passivated GaAs sample in a manner similar to the GaN experiments. Of course, different optics were used that were appropriate for the wavelength of recombination in bulk GaAs. In these experiments the $\lambda/4$ wave plate was flat and could be rotated instead of the linear polarizer. While both techniques allow for the determination of circular polarization, the rotating $\lambda/4$ wave plate method enables the measurement of all four Stokes parameters. The differences in the two techniques are discussed in the appendix.

PtIr control experiments were performed on the GaAs sample with surprising

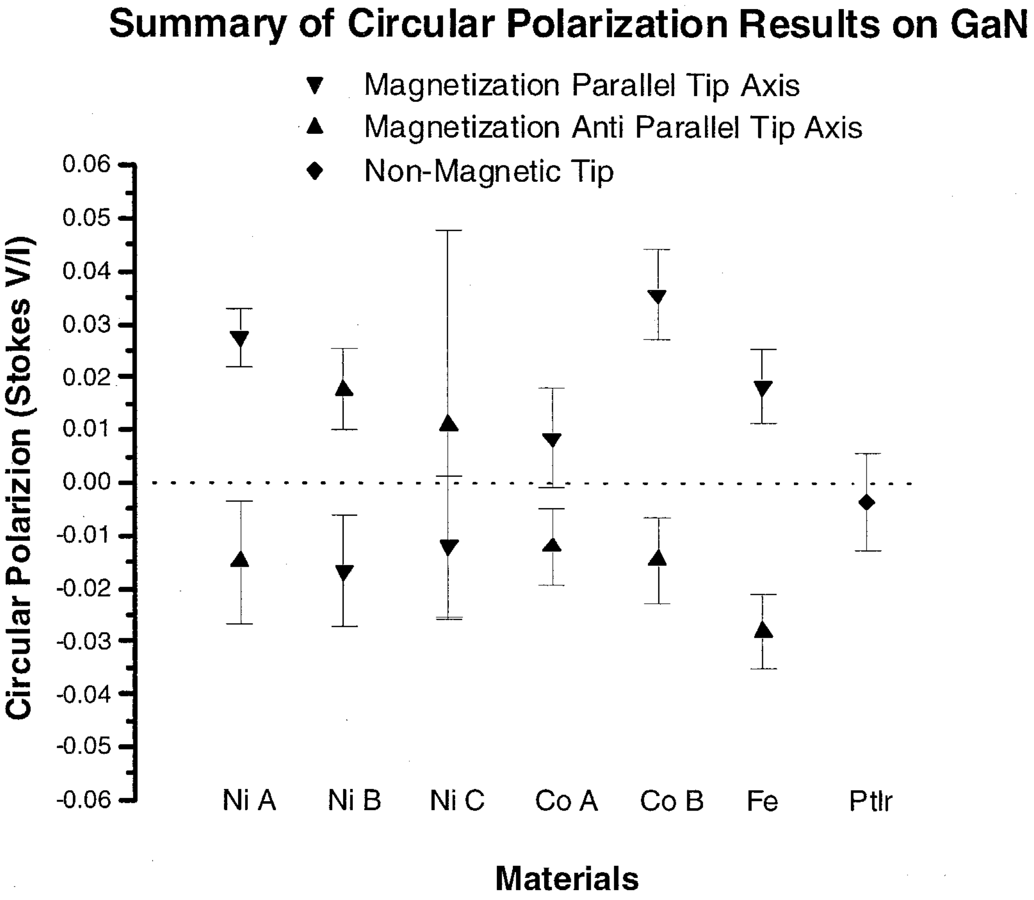

Figure 5.5: Summary of circular polarization data for light emission from GaN.

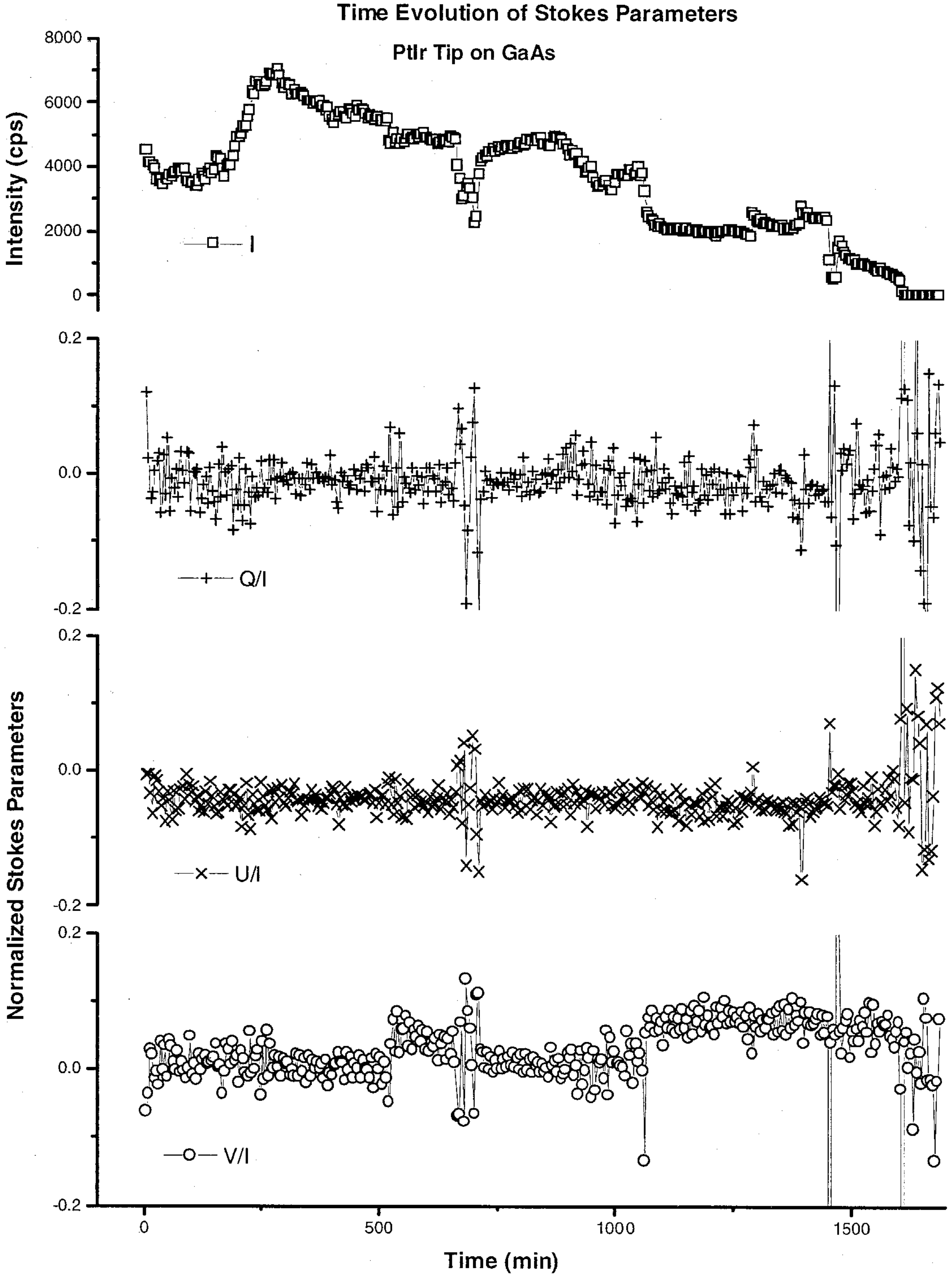

Figure 5.6: Evolution of Stokes parameters with time for PtIr tip D on GaAs.

results. Some tips showed a small yet persistent amount of circular polarization. A small component of linear polarization is to be expected since the Fresnel equations for reflections off of the metallic tip tend to remove components of $\vec{E}$ perpendicular to the tip. We do indeed see small amounts of linear polarization in our data. PtIr tips A, B, and C were characterized using alternating measurements of RCP and LCP intensities. Tip A showed a surprisingly large amount of circular polarization. Tips B and C showed none. For tip D we took full advantage of the experimental setup's ability to measure all four Stokes parameters. Figure 5.6 shows the time evolution of the Stokes parameters of the STM luminescence from a PtIr tip on GaAs taken over several hours. The overall intensity is shown in the top panel. It slowly decays over the data acquisition period. The normalized components of linear polarization, Q and U, remain roughly constant throughout the entire scan. Circular polarization spontaneously changes from the initial value of zero as the scan progresses. The stokes parameter V, which is the degree of circular polarization, jumps to a value of approximately 0.06 1100 minutes into the scan and holds this value steadily. Given this data on a non-magnetic tip, it is likely that with time the shape of the tip changed slightly during use and induced a small net circular polarization in the luminescence reflecting off of the tip.

In the GaAs experiments we use smaller feedback biases, which should tend to keep the tip held closer to the surface than in the GaN experiments. Additionally, the STM height data varies much more than the more reliable AFM data indicating that the tip may be coming into contact with the surface during the scan. As we use the tip for extended periods of time, the likelihood of bending the tip increases.

Spontaneous circular polarization has been seen in other STMLE experiments [1] and was attributed to the energy-dependent spin splitting of the GaAs conduction band along the (110) direction. This splitting has been used to produce spin polarized photoelectrons from negative electron affinity GaAs (110) surfaces [2]. This splitting does not, however, occur when k is along the (100) direction, which should be the direction of net k in our experiments. Other groups have seen spontaneous circular polarization in metal-metal STM light emitting experiments [3], but there the photon is coming from a plasmon-polariton decay mode, which has a preferred linear polarization [4]. The authors attributed this spontaneous amount of circular polarization to tip asymmetries. It is hard to imagine an obvious mechanism for producing spontaneous circular polarization from a normal metallic tip unless some symmetry breaking change of shape occurred during the scan.

To address the problems of tip demagnetization, a Lakeshore 421 Gaussmeter was purchased and used to measure the field outside the tip after coming out of the magnet and after being used for CP measurements. After being magnetized, the blunt end of Ni and Co tips would register a field of up to 10 G when placed in contact with the Gaussmeter. Strangely, Fe tips would not register any measurable field upon removal from the magnet. Since we could not be certain of the magnetization direction, Fe tips were no longer used in CP experiments.

Ni tips were tested again, and in one case very large results were seen. The top panel of Figure 5.7 shows the circular polarization for a Ni tip (Ni Tip D) magnetized antiparallel to the tip axis. A consistent CP of 14% is observed. However, when the magnetization of the tip was reversed in the magnet and retested, the sign of the CP reversed but with a much smaller magnitude. It is possible that if the difference is due to preferential injection of spin, then there must also be a geometric factor skewing the data towards positive circular polarization. After a third trip to the magnet the tip would unfortunately no longer give light.

Co tips were tested and also showed larger CP than in the GaN experiments. Unfortunately, no tip with large CP made it through the magnet more than once. One tip, Co Tip C, showed a very strange evolution of circular polarization with time. It started out with a fairly unstable luminescence intensity with a 22% CP. Several hours later it settled into a stable mode with an 7% circular polarization of the opposite sign. This data is shown in Figure 5.8. Upon removal from the STM holder, the overall magnetization still appeared to be in the original direction. The Gaussmeter claims that the magnetization of the tip did not change during the scan, which is consistent with the high Curie temperature and coercivity of cobalt. It is possible that the tip became blunted during the scan, and we no longer had the current

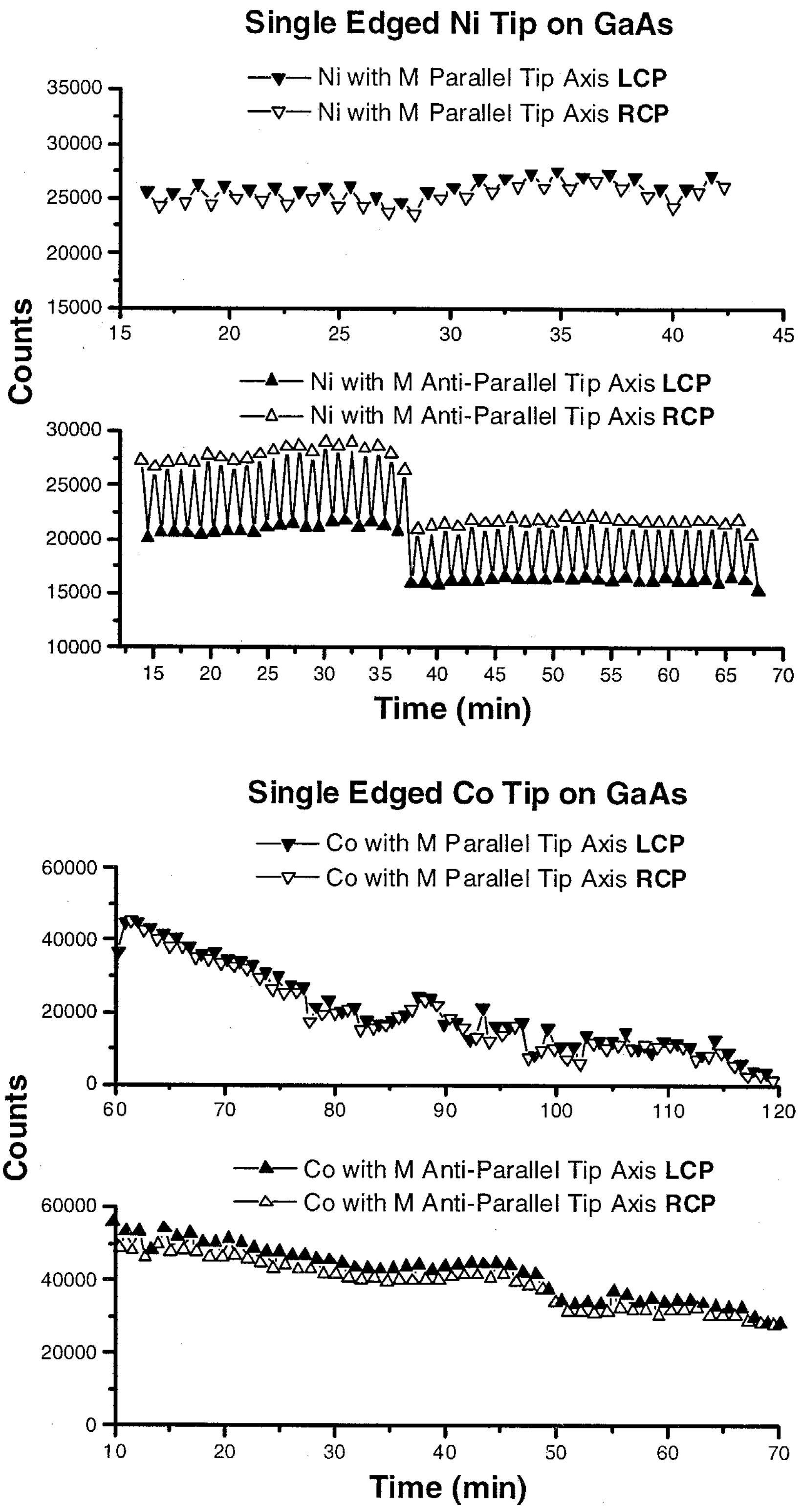

Figure 5.7: Raw Data for Ni(Top) and Co(bottom) on GaN. Magnetization of tip is parallel to tip axis, along $-z$, in the upper half of each plot and along $+z$ in the lower half. Each panel shows the raw data for successive measurements of RCP and LCP.

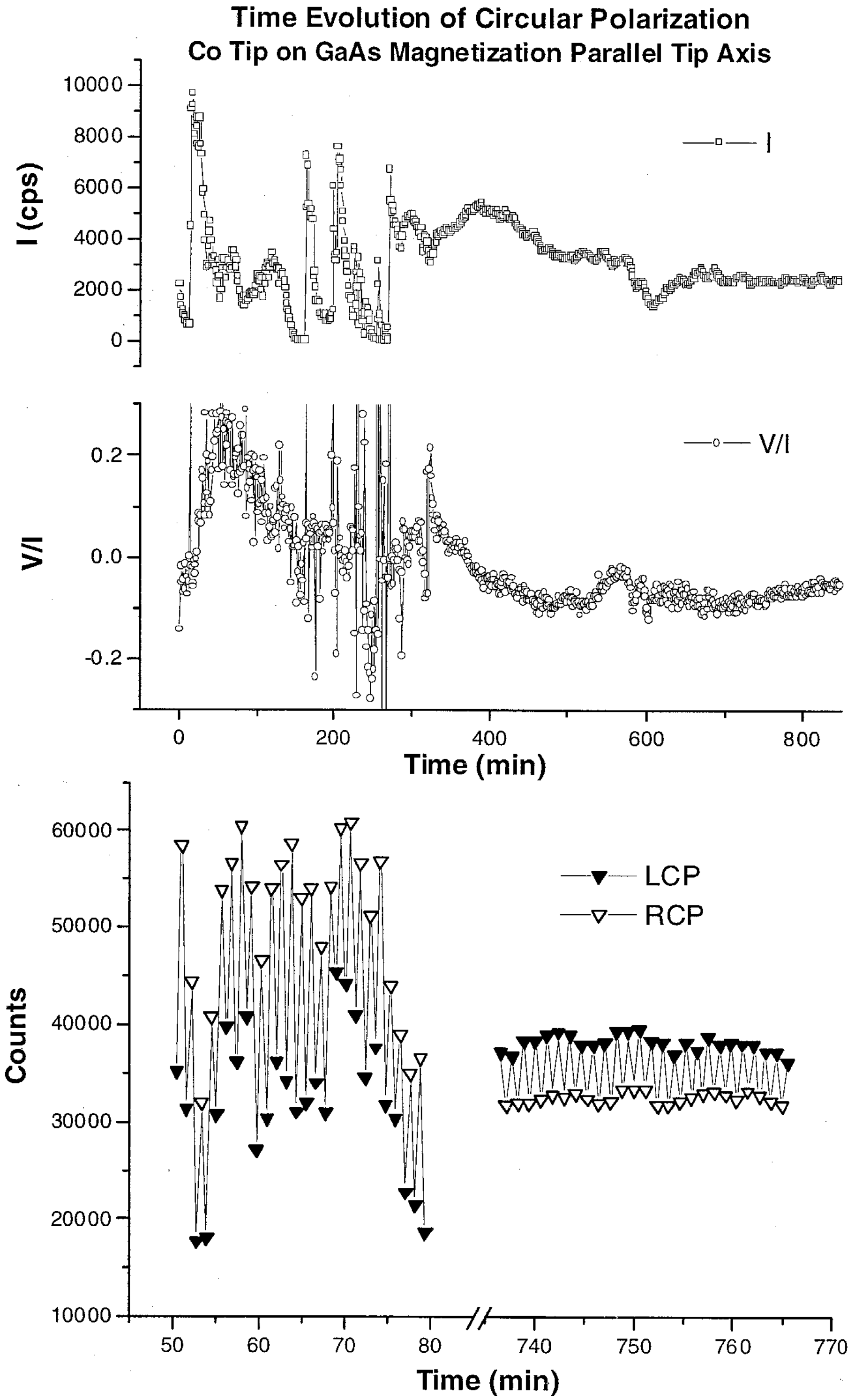

Figure 5.8: Circular Polarization Data for Co on GaAs. Magnetization of tip is parallel to tip axis, along $-z$. Top panels show Stokes intensity and normalized V parameters. Lower panel shows the raw data for two periods in time before and after the direction of circular polarization spontaneously reversed.

densities necessary to overcome the conductivity mismatch barrier to spin injection. This change in tip shape could have induced the net circular polarization that we see later in the same scan. The tip no longer gave light after a second magnetization process. Another Co tip (Co Tip D) was magnetized several times, and showed a consistent circular polarization which did not change with magnetization. Raw data from this tip is shown in the bottom panel of Figure 5.7.

Alvarado et al. reported similar behavior in the time dependence of circular polarization in their UHV measurements of Ni on GaAs [1]. They reported that some tips could show no circular polarization at all, or the circular polarization could go away with extended tip use. They cite insufficient cleaning of the tip for the first problem and absorption of contaminants onto the tip for the latter. We have seen similar behavior in that some tips show no circular polarization over the period of data acquisition, and in others circular polarization can quench after several hours of tip use. The Smith-Silver theory [5] makes it clear that if a tip can not deliver very high current densities, the spin injection efficiency will suffer. This helps explain why a blunt tip, while still injecting electrons and producing luminescence, can fail to inject spin polarized currents.

5.4 Summary

A summary of the circular polarization data taken on GaN and GaAs is shown in Figures 5.5 and 5.9. We can use the data to draw conclusions about the GaN spin lifetimes. The situation is complicated by the fact that it is possible for the spin polarization at the Fermi level of a ferromagnet to differ at different crystal faces. Depending on the technique used and crystal orientation, the spin polarization of Ni at the Fermi level has been reported to be as large as -100% [6]. Tedrow and Meservy in their original works reported a positive spin polarization for Ni [7, 8]. The STM measurements of Alvarado et al. made with polycrystalline Ni tips yielded negative spin polarizations of -31% [1]. This result was verified in a reverse experiment using GaAs tips pumped with circularly polarized light tunneling into Ni films [9], although

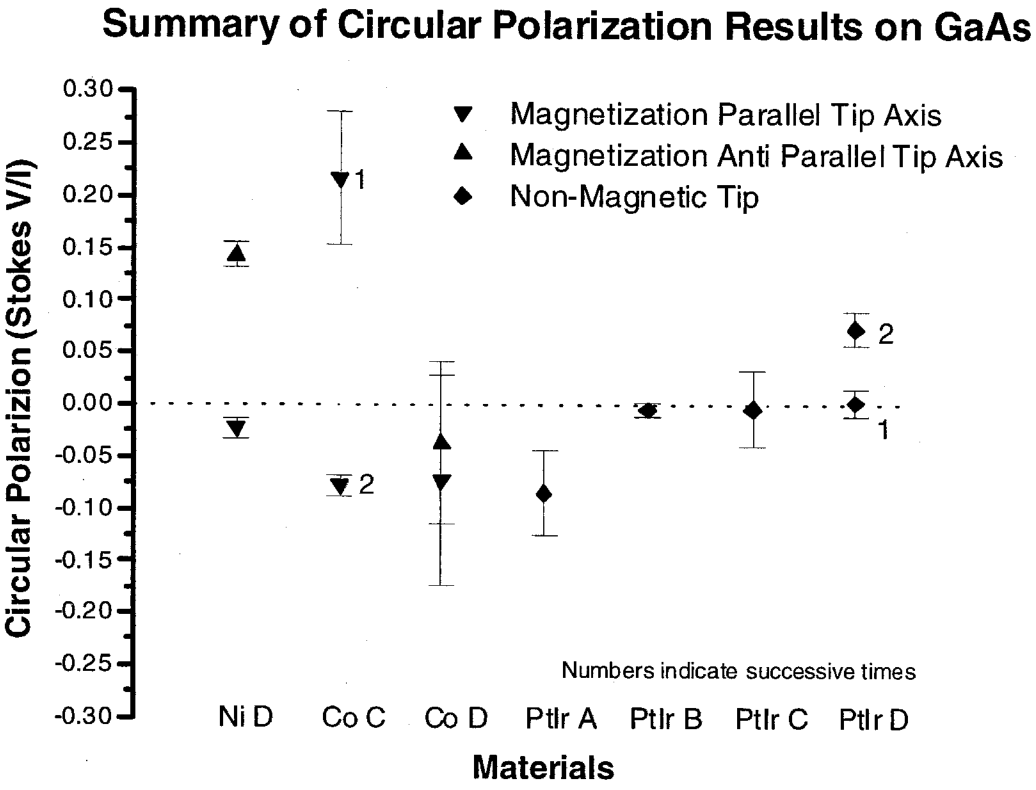

Figure 5.9: Summary of current circular polarization data for light emission from GaAs.

Tip	$(V_{down} - V_{up})/2$
Ni A	0.021 ±0.006
Ni B	-0.017 ±0.006
Ni C	-0.011 ±0.020
Co A	0.010 ±0.006
Co B	0.025 ±0.006
Fe A	0.023±0.005

Table 5.1: Results for the spin injection measurements on GaN. Values shown are the average circular polarizations for magnetization down minus magnetization up. A positive value indicates a positive spin polarization of the injected current.

the same assumptions were made about spin lifetimes.

In our experiments it is clear that the sign of the injected spin polarization for Ni is negative, and for Co and Fe it is positive. We choose to use the spin polarization values measured by Soulen et al. [10] who report values in the range of 0.40 to 0.42 for bulk Ni, Co and Fe using Andreev reflection techniques.

Using equation 3.30 with the values θ=13°, P_f=0.4, V_{GaN}^{max}=0.28 and our measured values of circular polarization on GaN from table 5.4, we can estimate a range of values for τ/τ_s to be between 3.4 and 10. Measurements on the minority carrier lifetime in room temperature p-GaN have yielded results of 0.1 ns [11] to 0.3 ns [12]. From this we can estimate the room temperature spin lifetime in GaN to be on the order of 50ps.

The GaAs results are not nearly as complete. The ability to induce circular polarization on PtIr tips has been demonstrated. We believe that our inability to produce definitive spin injection measurements on GaAs to date is due to our scanning method blunting the tips. Blunted tips will not allow the current densities necessary to overcome the conductivity mismatch and inject spin polarized currents into the semiconductor.

Bibliography

[1] S. F. Alvarado and P. Renaud, J. Appl. Phys. **73**, 5816 (1993).

[2] S. F. Alvarado, H. Riechert, and N. E. Christensen, Phys. Rev. Lett. **55**, 2716 (1985).

[3] A. Pierce, D. T.and Davies, J. A. Stroscio, and R. J. Celotta, Appl. Phys. A-Mater **66**, S403 (1998).

[4] Y. Uehara, Y. Kimura, S. Ushioda, and K. Takeuchi, Jpn. J. Appl. Phys. 1 **31**, 2465 (1992).

[5] D. L. Smith and R. N. Silver, submitted to Phys. Rev. B.

[6] E. Kisker, W. Gudat, E. Kuhlmann, C. R., and M. Campagna, Phys. Rev. Lett. **45**, 2053 (1980).

[7] R. Meservey and P. M. Tedrow, Phys. Rev. Lett. **26**, 192 (1971).

[8] R. Meservey and P. M. Tedrow, Phys. Rev. B. **7**, 318 (1973).

[9] K. Mukasa, K. Sueoka, H. Hasegawa, Y. Tazuke, and K. Hayakawa, Mat. Sci. Eng. B-Solid **31**, 69 (1995).

[10] R. J. Soulen, M. S. Osofsky, B. Nadgorny, T. Ambrose, P. Broussard, S. F. Cheng, J. Byers, C. T. Tanaka, J. Nowack, J. S. Moodera, G. Laprade, A. Barry, and M. D. Coey, J. Appl. Phys. **85**, 4589 (1999).

[11] Z. Z. Bandic, P. M. Bridger, E. C. Piquette, and T. C. McGill, Appl. Phys. Lett. **73**, 3276 (1998).

[12] M. Smith, G. D. Chen, J. Y. Lin, H. X. Jiang, A. Salvador, B. N. Sverdlov, A. Botchkarev, H. Morkoc, and B. Goldenberg, Appl. Phys. Lett. **68**, 1883 (1996).

Part II

Scanning Apertureless Microscopy

Chapter 6 Principles of SAM

6.1 Introduction

Imaging structures on the near atomic scale could revolutionize chemistry, biology and condensed matter physics. To this end, many imaging techniques have been developed which claim to measure optical properties at resolutions well below the classical diffraction limit for the illuminating wavelength. One of the most promising of these is the scanning apertureless microscope (SAM) technique pioneered by Wickramasinghe [1, 2, 3].

With any proximal probe technique there are questions about the exact source of the signal giving the image. Some of the controversy centers around whether or not one can truly separate information that is topographical in nature from that which is optical in any near field imaging technique [4]. This chapter focuses on the imaging theory and experiments with SAM and shows that the technique measures optical properties of the sample not accessible by a straightforward atomic force microscope (AFM) measurement.

The basic idea behind SAM is to use an AFM operating in tapping mode and perform an extra measurement. In tapping mode the AFM tip is oscillating perpendicular to the surface at a frequency on the order of 300 kHz and with an amplitude of a few nanometers. This method is believed to suffer less signal degradation from surface contaminants that are problematic when performing scanning microscopy in atmospheric conditions. While the tapping mode scan is performed, an external laser is used to illuminate the tip. The light scattered off of the tip is collected by a photodiode and then filtered by a lock-in amplifier with the tip oscillation frequency as a reference. This filtered signal is passed back to the AFM controller for digital storage. This technique allows the simultaneous measurement of sample topography with the AFM as well as information that is ostensibly optical in nature with the SAM.

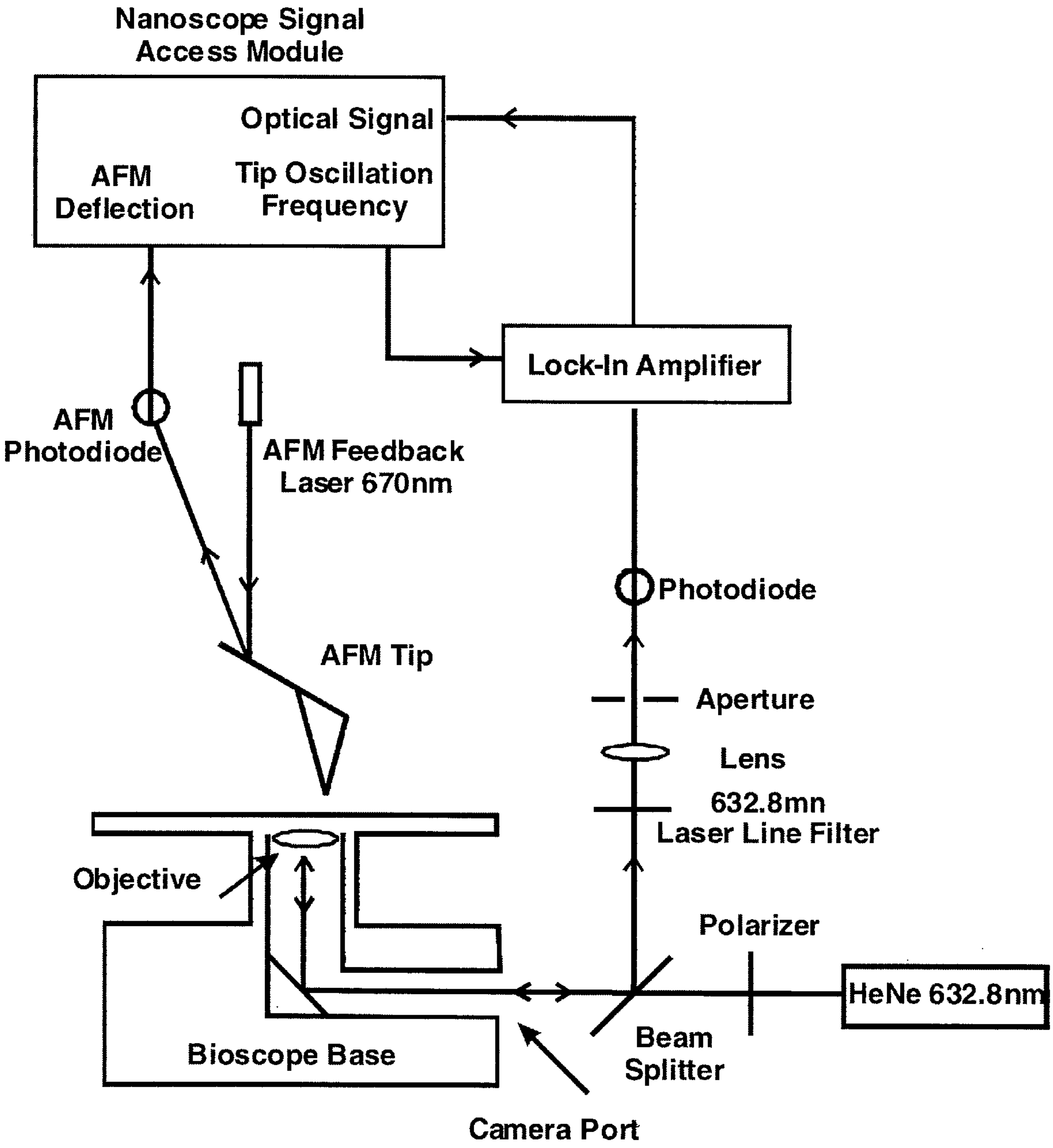

Figure 6.1: Schematic of the SAM experimental setup.

A simplified schematic of the experimental setup is shown in Figure 6.1. It consists of a Digital Instruments Bioscope AFM operating in tapping mode, with the AFM tip illuminated by an external HeNe laser source through the camera port of a Nikon Diaphot 200 optical microscope which forms the base of the Bioscope. The diaphot is an inverted microscope, so in this transmission mode setup the substrate must be transparent to the illuminating wavelength. The technique is not restricted to transmission mode, instruments have been made where the laser is not normally incident on the sample and the scattered light is collected by a fiber [5]. Here the microscope objective focuses the external laser onto the top of the cover slide on which the sample is prepared. The tip then scans in the focused laser spot. The light scattered by the tip is collected by the microscope objective and directed via a beam splitter through a focusing lens and a notch filter before detection. The notch filter rejects light from the diode laser used by the AFM to measure tip deflection. An EG&G Park 5302 lock-in amplifier takes the photodiode signal and passes the component changing with the tip oscillation frequency to the DI Nanoscope IIIa control electronics. A detailed description of the development of this particular instrument can be found in [6].

The optical image is the direct measurement of the intensity of the radiation scattered by the AFM tip at the oscillation frequency. A coupled-dipole model explaining image contrast was first proposed by Wickramasinghe. In this model, dipole fields are induced in both the tip and sample by the external laser. Since the tip is performing an oscillatory motion at the tapping frequency, the lock-in amplifier can detect the far-field dipole radiation pattern of the tip. This far-field radiation pattern will depend on the induced dipole moment in the tip. The dipole moment of the tip will be proportional to the total field incident on the tip, which will be the sum of the field due to the external laser and the near fields of the dipoles induced in the samples. The following derivation is based on these simple ideas.

6.2 Theory

The AFM tip is modeled as a radiating dipole, where the expression for the far-field produced by such a dipole is [7]

$$\vec{E}_t = \frac{1}{4\pi\epsilon_0}\frac{k^2 e^{i(\vec{k}\cdot\vec{d}-\omega t)}}{d}\left(\hat{n}\times\vec{p}_t\times\hat{n}\right), \tag{6.1}$$

where k is the wave number of the radiation, $\vec{p}_t$ is the dipole moment of the tip, ω is the angular frequency of the oscillation, $\vec{d}$ is the vector from the dipole to the observation point, and $\hat{n}$ is in the unit vector in the direction of the observation point. The angles and parameters used in the derivation are depicted in figure 6.2.

The corresponding intensity at the detector is

$$I_t = \frac{c\epsilon_0 k^4}{(4\pi\epsilon_0)^2 d^2}\langle|\vec{p}_t|^2\rangle \sin^2\phi, \tag{6.2}$$

where c is the speed of light, ϵ_0 is the permittivity of free space, and ϕ is the angle between the vector from the tip to the detector and the dipole moment of the tip. The term in the above equation which contains optical information about the sample is $\vec{p}_t$, the dipole moment of the tip, which is given by

$$\vec{p}_t = 4\pi\epsilon_0\alpha_t(\vec{E}_{laser} + \vec{E}_s), \tag{6.3}$$

where α_t is the polarizability of the tip. The total field incident on the tip is the sum of the laser field $\vec{E}_{laser}$ and the sample's field $\vec{E}_s$. It is therefore necessary to calculate the very near field of the sample in order to determine the far-field radiation pattern produced by the tip.

For simplicity, we model the features being imaged as dielectric nanospheres with an induced dipole moment, which to first order, is $\vec{p}_s = 4\pi\epsilon_0\alpha_s\vec{E}_{laser}$, where all of the symbols are the same as before except that they refer to the sample instead of the tip. The value of the polarizability, α_s, is dependent on the structure of the sample

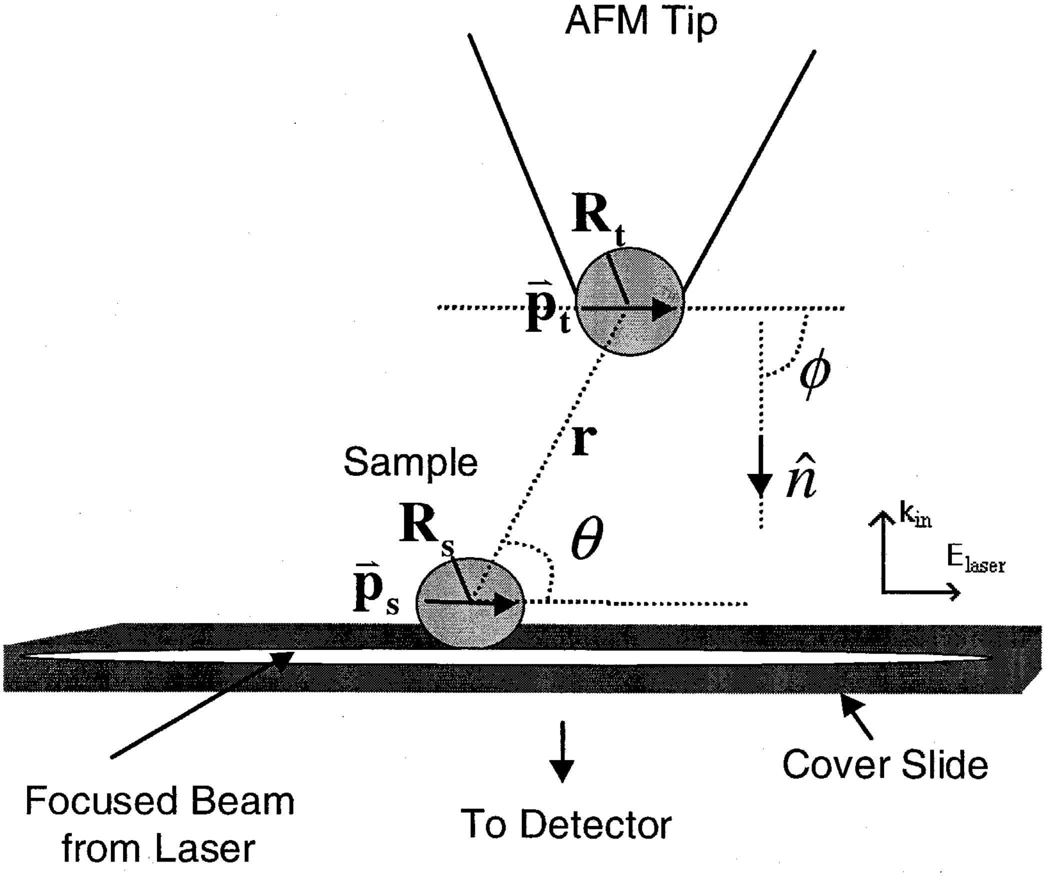

Figure 6.2: Close-up of tip and sample showing the parameters used in the calculations.

and the wavelength of the external laser, and for spheres is expressed as

$$\alpha_s = \frac{\epsilon_s/\epsilon_0 - 1}{\epsilon_s/\epsilon_0 + 2} R_s^3, \tag{6.4}$$

where R_s is the radius and ϵ_s is the dielectric constant of the sphere [7]. The dependence on the laser frequency and index of refraction is contained in ϵ_s, since $n = \sqrt{\epsilon_s}$ and ϵ_s will be a function of frequency.

The standard textbook equation for the near field of a dipole is

$$\vec{E} = (3\hat{n}\,(\hat{n} \cdot \vec{p}) - \vec{p}) \left(\frac{1}{r^3} - \frac{ik}{r^2} \right) e^{i\vec{k}\cdot\vec{r}}. \tag{6.5}$$

Equation 6.5 is an approximation which does not take into account the actual physical dimensions of the dipole. In these experiments the tip dimensions and tip-feature spacing will be on the order of the size of the feature. It is necessary to start from the beginning with the potential distribution for a physical dipole [8]. The field of a physical dipole with finite width a oscillating with angular frequency ω is

$$\vec{E} = -\vec{\nabla} \frac{q}{4\pi\epsilon_0} \left(-\frac{cos\left(\omega(t - \frac{r^-}{c})\right)}{r^-} + \frac{cos\left(\omega(t - \frac{r^-}{c})\right)}{r^+} \right), \tag{6.6}$$

where r is the distance from the center of the dipole to the observation point and $r\pm = (a^2 + r^2 \pm arcos(\theta))^{\frac{1}{2}}$. Taking the gradient in spherical coordinates gives the full expression for the near field of the sample. This near field, accurate to first order in the external field $\vec{E}_{laser} \cos \omega t$ and taking into account the finite dimensions of the dipole, is

$$\vec{E}_s = \frac{\alpha_s |\vec{E}_{laser}|}{2R_s^3} \left(\begin{array}{c} \left[\frac{(R - \cos\theta)\cos\omega t_-}{d_+^{3/2}} - \frac{(R + \cos\theta)\cos\omega t_+}{d_-^{3/2}} - \frac{\omega R_s \sin\omega t_-}{cd_+} - \frac{\omega R_s \sin\omega t_+}{cd_-} \right] \hat{e}_r \\ + \sin\theta \left[\frac{\cos\omega t_-}{d_+^{3/2}} + \frac{\cos\omega t_+}{d_-^{3/2}} - \frac{\omega R_s \sin\omega t_-}{cd_+} - \frac{\omega R_s \sin\omega t_+}{cd_-} \right] \hat{e}_\theta \end{array} \right), \tag{6.7}$$

where r is the distance between the center of the sample and the observation point, θ is the angle between the sample's dipole moment and the vector locating the observation point, t is time, $d_\pm = 1 + R^2 \pm 2R\cos\theta$, $t_\pm = t - R_s d_\pm^{1/2}/c$ and $R = r/R_s$.

Equation 6.7 makes use of the substitution

$$\begin{aligned} |\vec{p}_s| &= 2a_s q \\ &= 4\pi\epsilon_0\alpha_s|E_{laser}| \end{aligned} \tag{6.8}$$

for the dipole moment induced in the sample by the external laser. Second order effects due to the tip's field modulating the sample's dipole moment are neglected. When the sample is spherical, equation 6.4 for α_s can be used.

This near field, E_s, changes the induced dipole moment of the AFM tip and effectively modulates the scattered intensity measured at the detector as the AFM tip scans across the sample. In this first order treatment the effect of the tip on the sample field is ignored.

From equation 6.7 and the plot in Figure 6.3, it can be seen that the near field of the sample dipole will add destructively with the external field inducing the tip dipole when the tip is directly above the sample. The fields will add constructively when the tip is on either side of the sample along the dipole axis, although this effect is more localized and, therefore, presumably more difficult to observe than the effects due to destructive interference.

With the expression for the near field of the sample, the total field at the tip can now be calculated. The intensity at the detector can be calculated for an arbitrary number of samples, n, as

$$I_t = \epsilon_0 c \frac{k^4}{d^2}\frac{|\alpha_t|^2}{2}\left[\langle|\vec{E}_{laser}|^2\rangle + \sum_{i}^{n}\langle\vec{E}_{laser}\cdot\vec{E}^*_{si} + c.c.\rangle + \sum_{i,j}^{n}\langle\vec{E}_{si}\cdot\vec{E}^*_{sj} + c.c.\rangle(1-\frac{\delta_{ij}}{2})\right]. \tag{6.9}$$

The δ_{ij} is simply a bookkeeping term, which prevents the intensities when $i = j$ from being counted twice.

It is obvious that this treatment of the fields relies on a specific type of sample geometry. Other groups have performed simulations for corrugated dielectric interfaces [9]. These types of simulations depend heavily on the evanescent fields created

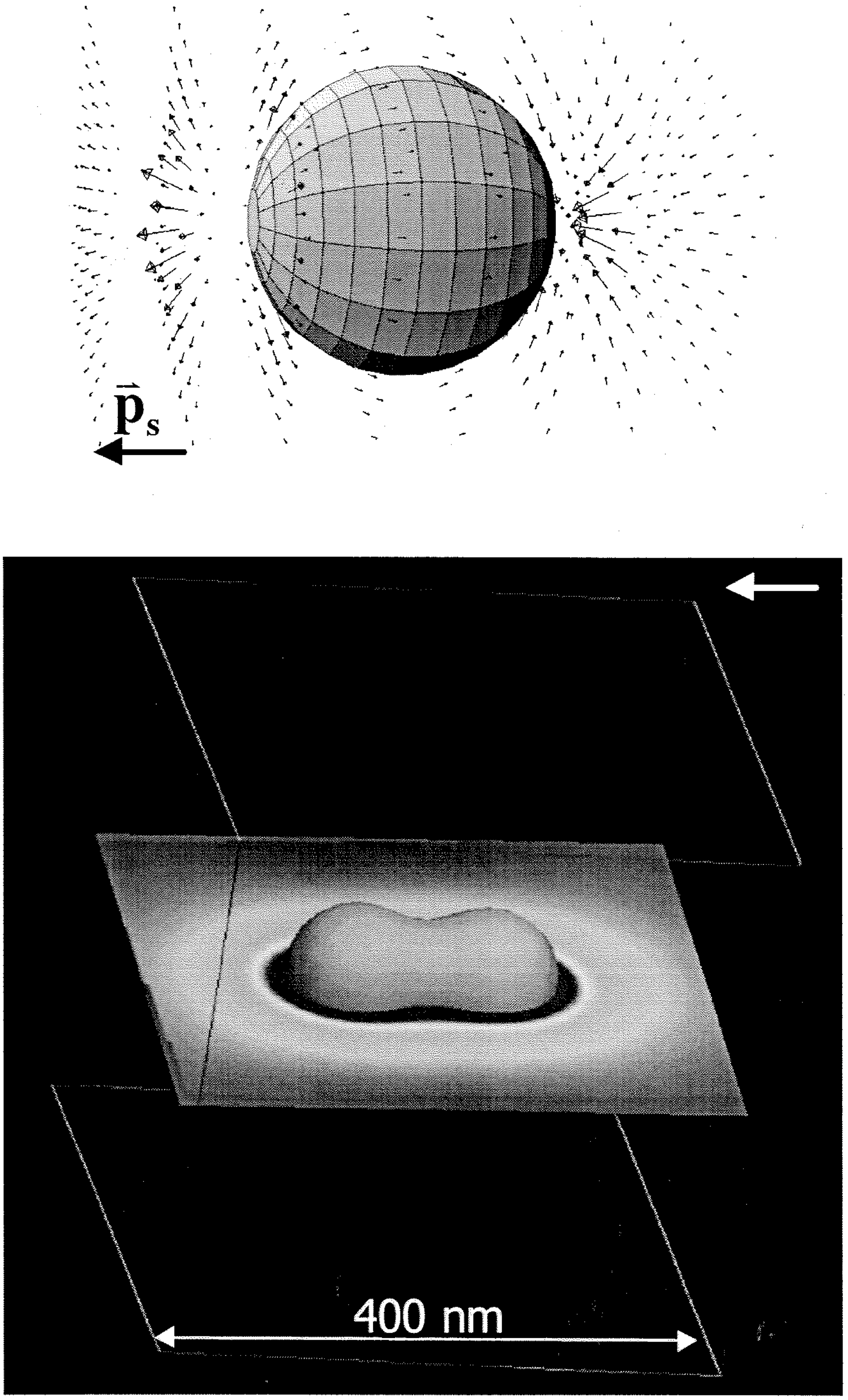

Figure 6.3: Electric field (A) and modulus (B) of a 50 nm physical dipole similar to the ones used in the image simulations.

by total internal reflection as the source of local field enhancement [10]. The field enhancement from metallic probes has also been simulated [11]. In many of these cases the AFM can tell you everything there is to know about the sample. The model presented here lends itself more readily to size standards of different materials and biologically interesting cases.

Bibliography

[1] H. Wickramasinghe and C. Williams, 1989, Apertureless Near Field Optical Microscope, U.S. Patent 4,947,034.

[2] F. Zenhausern, Y. Martin, and H. K. Wickramasinghe, Science **269**, 1083 (1995).

[3] F. Zenhausern, M. P. Oboyle, and H. K. Wickramasinghe, Appl. Phys. Lett. **65**, 1623 (1994).

[4] B. Hecht, H. Bielefeldt, Y. Inouye, D. W. Pohl, and L. Novotny, J. Appl. Phys. **81**, 2492 (1997).

[5] P. M. Adam, P. Royer, R. Laddada, and J. L. Bijeon, Appl. Opt. **37**, 1814 (1998).

[6] P. M. Bridger and T. C. McGill, Opt. Lett. **24**, 1005 (1999).

[7] J. Jackson, *Classical Electrodynamics*, 2nd ed. (John Wiley & Sons, Inc., New York, NY, USA, 1974).

[8] D. Griffiths, *Indroduction to Electrodynamics*, 2nd ed. (Prentice-Hall, Inc., Englewood Clifs, NJ, 1989).

[9] A. Madrazo, R. Carminati, M. Nieto-Vesperinas, and J. J. Greffet, J. Opt. Soc. Am. A. **15**, 109 (1998).

[10] G. von Freymann, T. Schimmel, and M. Wegener, Appl. Phys. A-Mater **66**, S939 (1998).

[11] H. Furukawa and S. Kawata, Opt. Commun. **148**, 221 (1998).

Chapter 7 Simulations and Experiments

7.1 Computer Program

Equation 6.9 gives the total intensity for radiation scattered off of the AFM tip that would be measured at a detector. The actual strength of the incident laser is not necessary to simulate the image contrast that would arise from the interaction of the tip with the field of the sample. The amplitude of the electric field $\vec{E}_s$ was shown in equation 6.7 to be proportional to $\vec{E}_{laser}$. This term can be factored out of 6.9 leaving a normalized intensity of unity modulated by cross terms between the external laser and the samples and cross terms between the sample fields themselves.

To calculate this intensity a C++ program with a Tcl/Tk graphical user interface has been developed which takes as input the topographical data from an AFM image. The user then specifies the location of the center of each sample, along with the sample's radius and index of refraction. The final necessary elements are the tip radius and the wavelength of the external laser. In order to determine the direction of the induced dipole moments, the direction of linear polarization of the laser is also specified. A screen capture illustrating this process is shown in Figure 7.1.

The modulated intensity at each pixel is then calculated by assuming the tip center is located a distance R_t directly above the surface as given by the AFM image. The tip-sample separation is then calculated and the total electric field experienced by the tip, $\vec{E}_{laser} + \sum \vec{E}_s$, is known. The AFM image in Figure 7.2 is of two adjacent 50 nm diameter polystyrene beads on glass. Also shown is apertureless data taken with the illuminating laser randomly polarized. We take this AFM image one as a basis for calculating tip-sample separations. If we add to this the pertinent material parameters, we can use the results of the previous section to generate a theoretical SAM image.

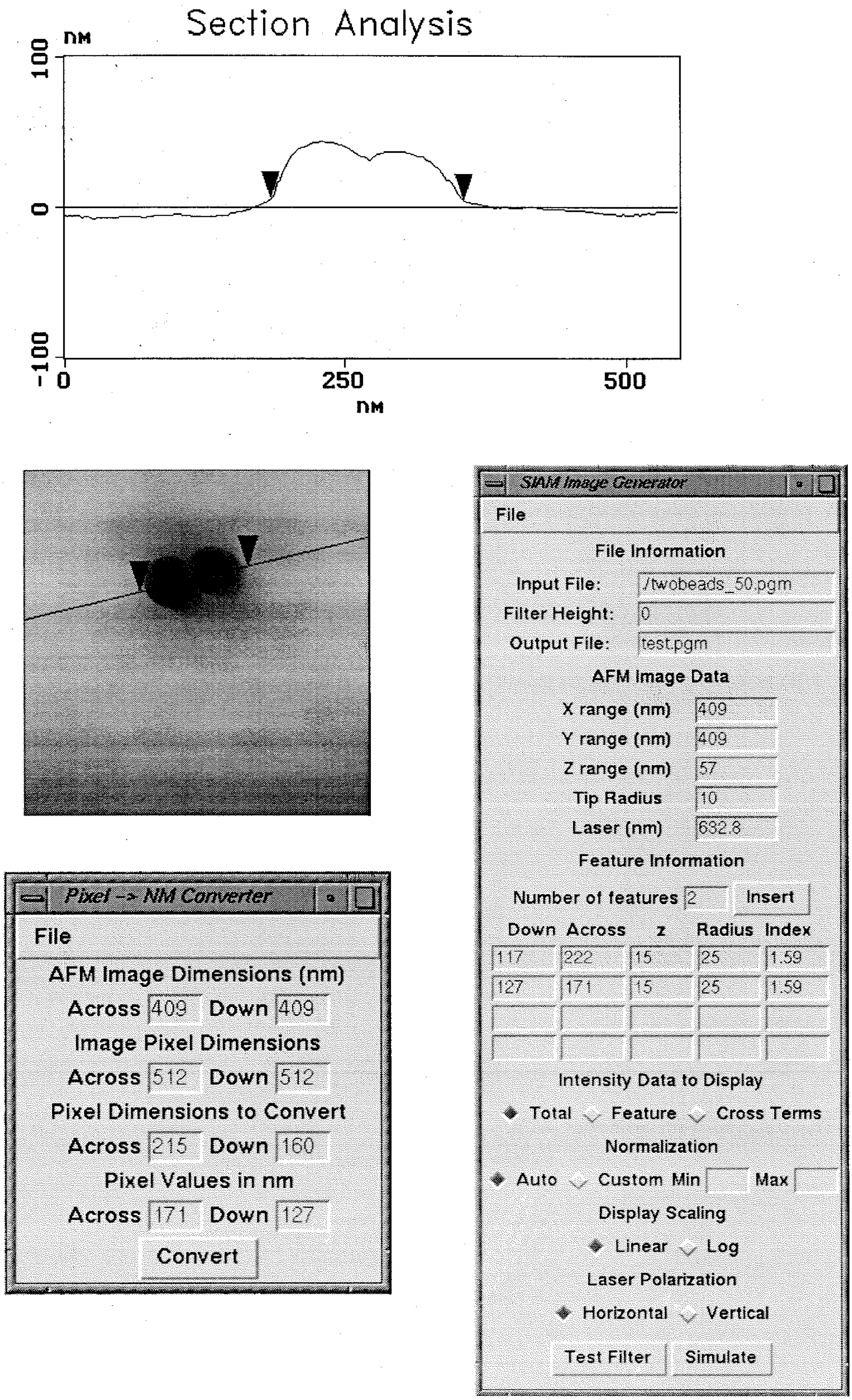

Pixel -> NM Converter

File

AFM Image Dimensions (nm)

Across 409 Down 409

Image Pixel Dimensions

Across 512 Down 512

Pixel Dimensions to Convert

Across 215 Down 160

Pixel Values in nm

Across 171 Down 127

Convert

SIAM Image Generator

File

File Information

Input File: ./twobeads_50.pgm

Filter Height: 0

Output File: test.pgm

AFM Image Data

X range (nm) 409

Y range (nm) 409

Z range (nm) 57

Tip Radius 10

Laser (nm) 632.8

Feature Information

Number of features 2 Insert

Down	Across	z	Radius	Index
117	222	15	25	1.59
127	171	15	25	1.59

Intensity Data to Display

● Total ○ Feature ○ Cross Terms

Normalization

● Auto ○ Custom Min ☐ Max ☐

Display Scaling

● Linear ○ Log

Laser Polarization

● Horizontal ○ Vertical

Test Filter Simulate

Figure 7.1: Process for generating a simulated image. The AFM image is analyzed for height information and an educated guess is made about the locations of the sample centers. Pixels are converted to physical units. The AFM data is read into the simulation and the other relevant information is given to the GUI.

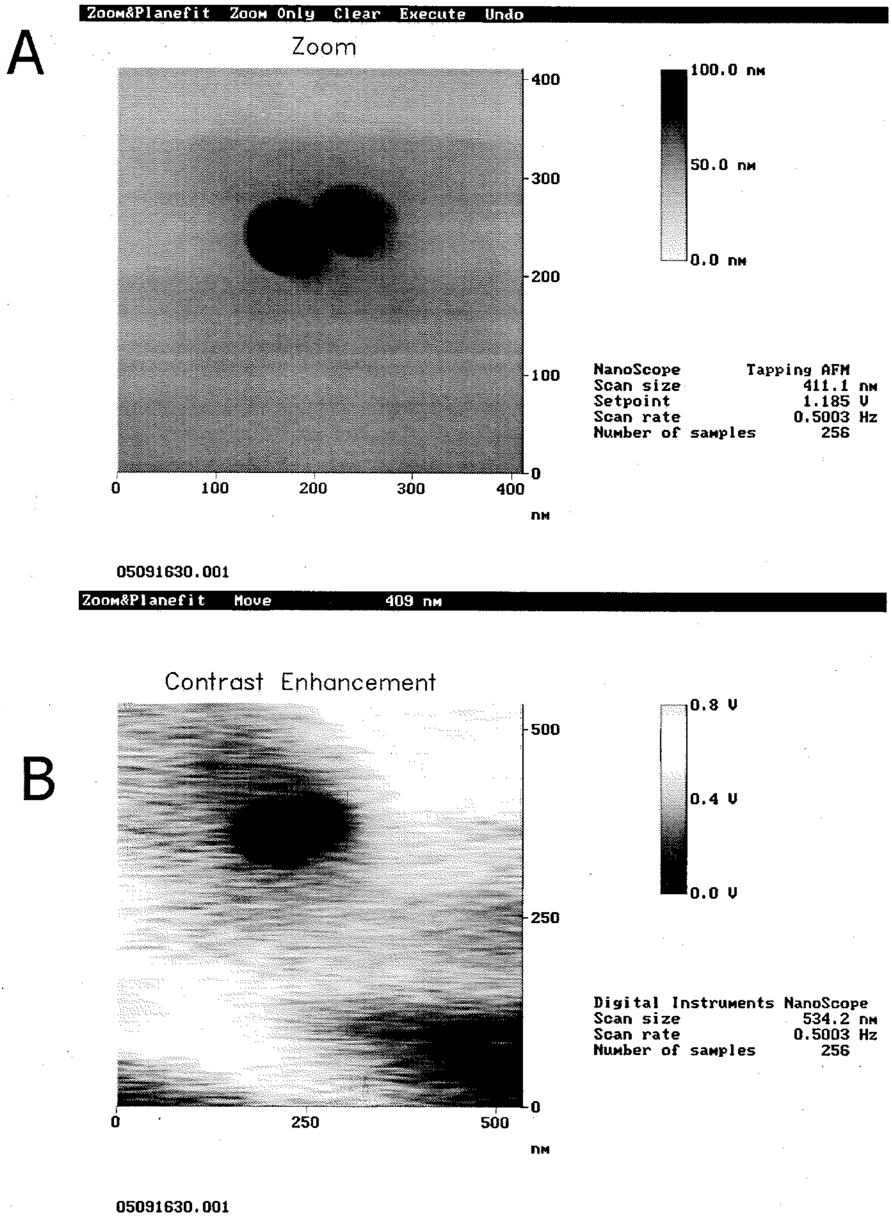

NanoScope Tapping AFM
Scan size 411.1 nm
Setpoint 1.185 V
Scan rate 0.5003 Hz
Number of samples 256

Digital Instruments NanoScope
Scan size 534.2 nm
Scan rate 0.5003 Hz
Number of samples 256

Figure 7.2: AFM (A) and SAM with randomly polarized external laser (B) images of two adjacent 50 nm diameter polystyrene beads. Scan taken by P.M. Bridger.

7.2 Calculated Images

7.2.1 Polarization Dependence

In the following simulations, the values λ=632 nm, R_s=25 nm, R_t=10 nm, and n_s=1.59 are used except where otherwise noted. All intensity values are normalized to the scattered intensity in the absence of any modulation due to the sample's electric field. The corners of each image far away from the sample will therefore show a normalized intensity of unity. Due to the limitations of black and white printing, each image is scaled in 256 shades of grey between the minimum and maximum intensity values for optimal contrast. Figure 7.3 shows the effect of different orientations of the linear polarization of the external laser. What is most striking about the images is an obvious anisotropy in intensity due to the orientation of the dipole field. These images also suggest that an enhancement in resolution is possible for two adjacent objects if their dipoles are aligned to give a large field between them. The change in intensity due to the presence of the samples is approximately 30% above the samples due to destructive interference. This effect is quite spread out and should be the easiest to detect in the actual experiment. On the sides of the sample aligned with the dipole axis are areas where the intensity has increased roughly 60% due to constructive interference between the sample and laser fields. These effects are much more localized than the effects which lessen the intensity and will therefore be more difficult to observe. These localized effects are not visible in the image taken with unpolarized light shown in Fig 7.2. There is no definite direction for the dipole moment of the samples except that it must lie in the plane perpendicular to the direction of light propagation, and therefore the dipole model cannot make a distinction between the vertical and horizontal directions in the images.

7.2.2 Tip Dependence

Unlike conventional optical microscopy where the resolution is ultimately limited by the wavelength of illumination, the parameter which should limit the resolution in

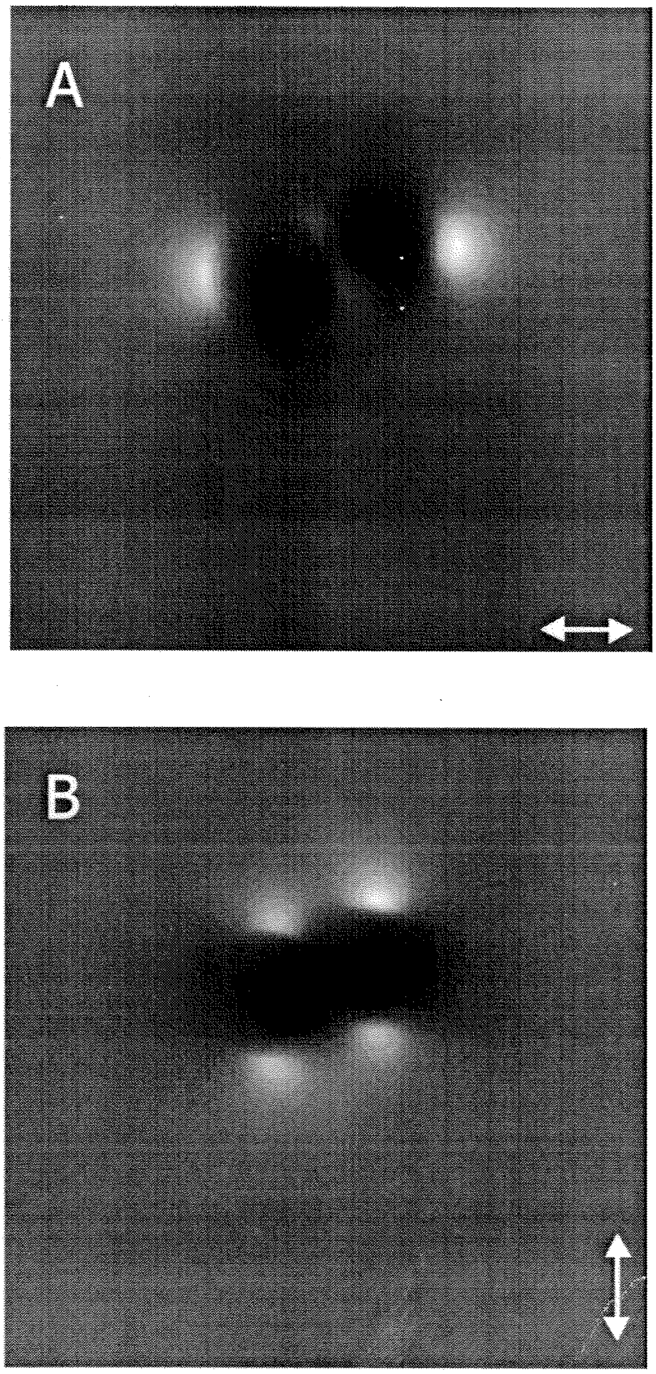

Figure 7.3: Simulations showing the image contrast dependence on the external laser polarization. Polarization direction is indicated by the arrows. (A) horizontal polarization, data range 0.76 to 1.43. (B) vertical polarization, data range 0.64 to 1.34. White indicates highest intensity.

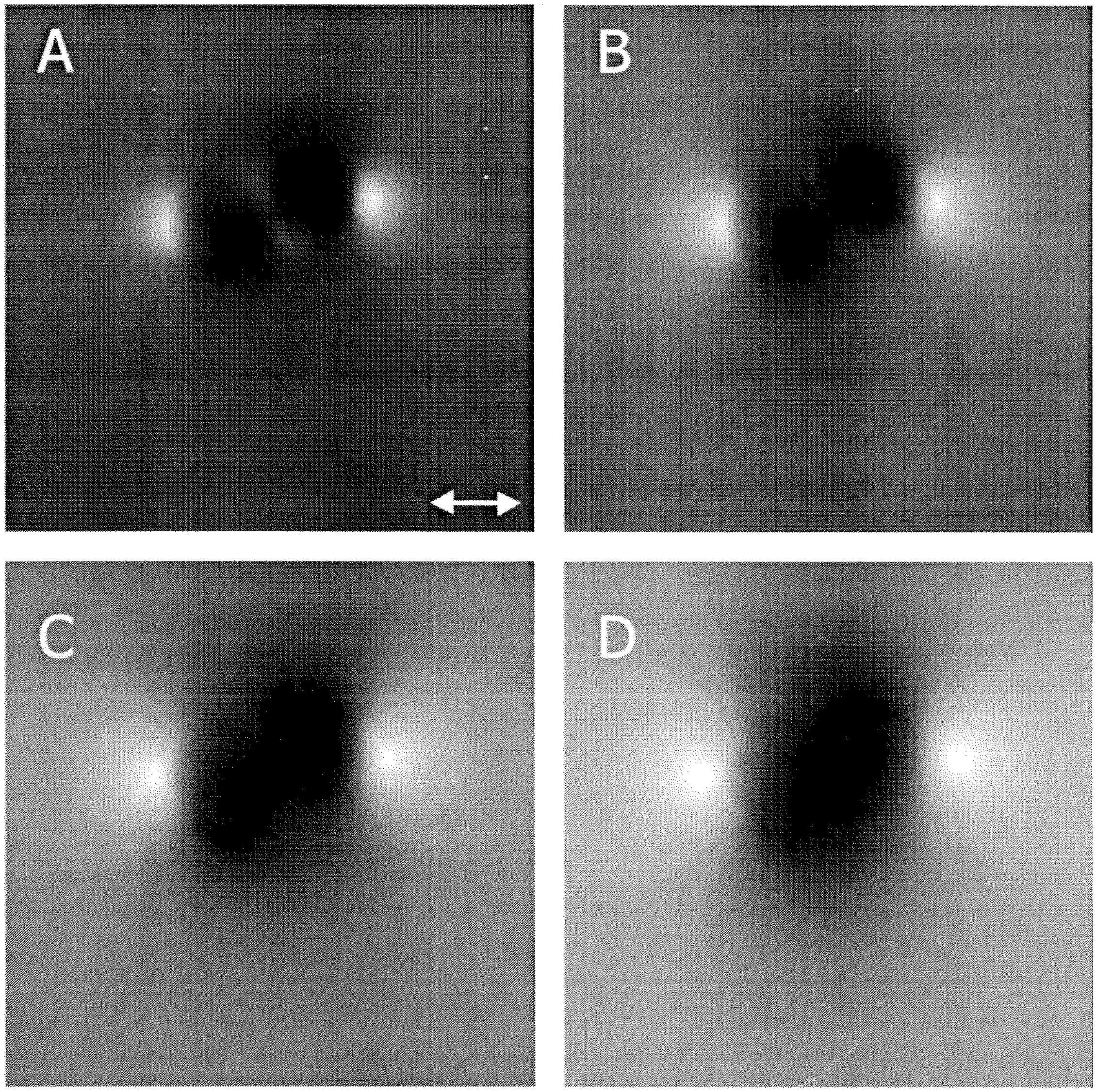

Figure 7.4: Intensity contrast vs. tip size, with external laser polarization set in the horizontal direction. (A) 10 nm tip, data range 0.76 to 1.43. (B) 20 nm tip, data range 0.78 to 1.14. (C) 30 nm tip, data range 0.91 to 1.06. (D) 40 nm tip, data range 0.93 to 1.04. White indicates highest intensity.

SAM is the size of the tip. If the tip is too large to explore variations in the local electric field, then resolution will be compromised. Figure 7.4 shows four panels where the size of the tip is increased from 10 to 40 nm in steps of 10 nm. As the tip gets larger, it is no longer able to enter the regions of high sample field between the two spheres, and the two beads which are clearly resolved in panel (a) gradually merge as the tip radius increases. In panel (d) with the 40 nm tip, the two features are barely recognizable as separate entities. Although one cannot tell from viewing the images, the intensity contrast also drops off with the increasing tip size. The range of data in panel (a) is from 0.76 to 1.43, while in panel (d) it is much smaller, ranging from 0.93 to 1.04. If panel (d) were printed on the same scale as panel (a), it would simply come out as a grey square. It is fortunate for the imaging method that the demands of AFM resolution force most AFM tips to be made with dimensions much closer to 10 nm than 40 nm.

7.2.3 Index Dependence

There is also a strong dependence on the sample's index of refraction at all wavelengths. The amplitude of the near field of the sample varies linearly with the polarizability. The polarizability varies as in equation 6.4. Figure 7.5 shows how the image contrast changes with sample index of refraction. In each panel the sphere on the right has n=1.59, while the index of the left bead is varied. Panel (a) is a sanity check, with the index of the sample set to 1. This is the same as open space, with a polarizability of zero. There will be no dipole field for this feature. The image would look exactly like the case with a single sphere present except for the fact that the surface map from the AFM is still there, preventing the tip from getting far enough down to sample the region of enhanced field. Panel (b) has the index of the left bead set to 1.3, slightly lower than the feature on the right. We can begin to see the effects of destructive interference over the left feature, but not as pronounced as the right. Panels (c) and (d) continue to increase the index of the left bead, at values of 1.8 and 4, respectively. In all of these images the sample with the larger index causes

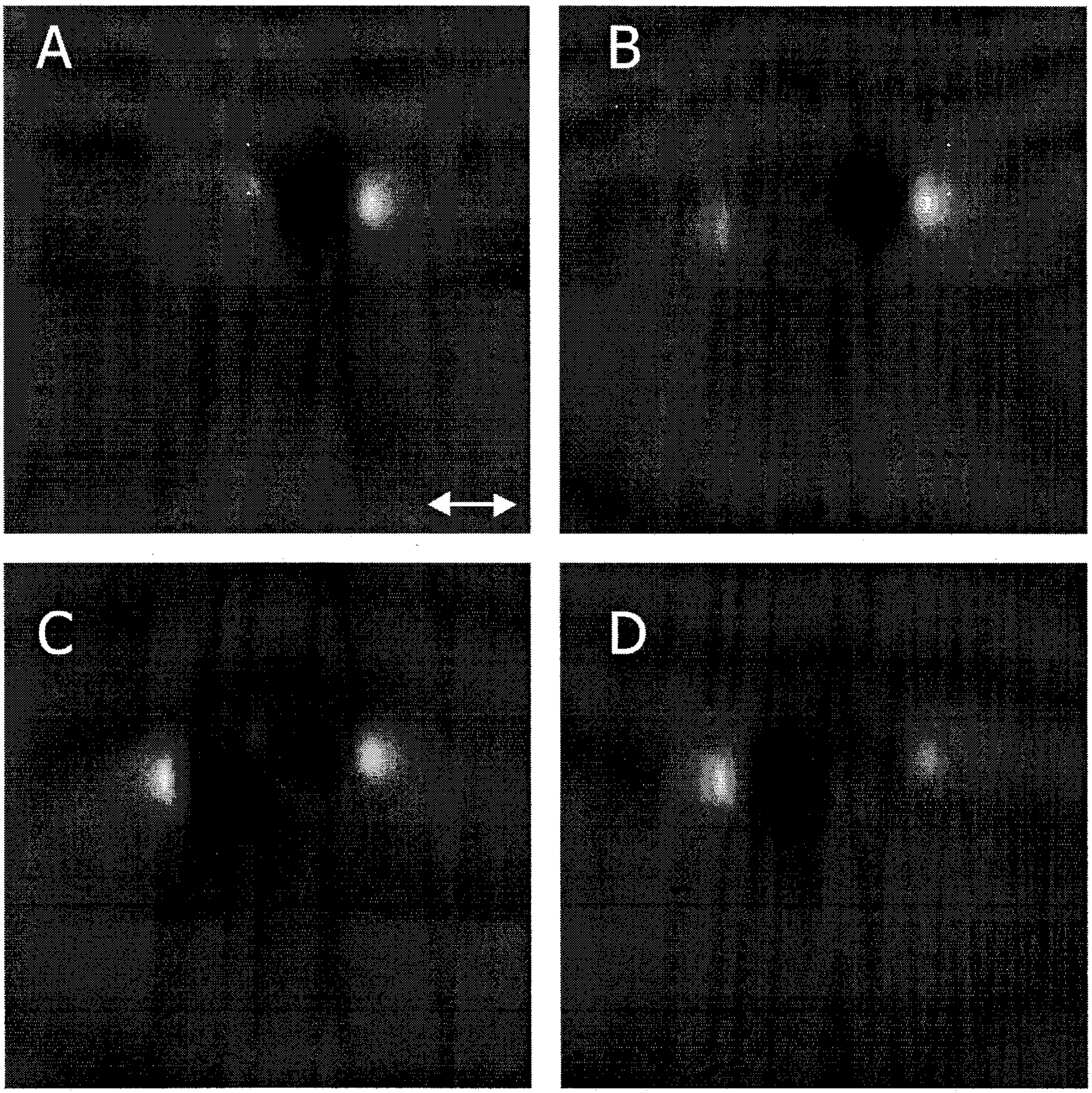

Figure 7.5: Simulations of intensity contrast vs. sample index of refraction, with external laser polarization set in the horizontal direction. Right bead n=1.59. (A) Left bead n=1.0, data range 0.69 to 1.34. (B) Left bead n=1.3, data range 0.73 to 1.36. (C) Left bead n=1.8, data range 0.72 to 1.55. (D) Left bead n=4.0, data range 0.43 to 2.14. White indicates highest intensity.

the greatest variations in intensity. This result has very important implications for optical imaging. If two beads of the same size but different materials were placed side by side, no force microscopy measurement could tell them apart. However, the optical image would be sensitive to the constituent materials. Properties that correspond to color or opacity when the size of the particle is much larger than the imaging wavelength could now be resolved on the nanometer scale.

The printing limitations make it difficult to see that the range of data and hence contrast increases with increasing n. For the image with n =1.8, the range of data is from 0.72 to 1.55 and with n =4.0, the range is from 0.43 to 2.14. This effect is accounted for by the fact that the polarizability increases from 0.52 to 0.83. The main contribution to intensity contrast is the cross terms between the external laser field and the sample's field, and these terms are linearly dependent on the polarizability. The effect will not continue in this drastic fashion since the polarizability rapidly approaches unity as n is increased. Therefore, perhaps the best test of this model would be to use low index glass size standards side by side with size standards made from semiconductors with n closer to 4.

7.2.4 Wavelength Dependence

The top two panels Figure 7.6 are calculated for horizontal polarization with the wavelength of the external laser taken as HeNe red (632 nm) and green (543 nm). We assume that the index of refraction stays constant over this wavelength range. The two images generated are nearly identical. The actual range of intensities varies from 0.758 to 1.430 in the image generated with 632 nm light and 0.754 to 1.433 in the image generated with 543 nm light. This is because λ only appears outside of a cosine term in the sample field as a factor of $R_s\omega/c$ in front of the r^{-2} terms. Here we are imaging at tip-sample separations where the r^{-3} dominate the intensity contrast. The ratio of the amplitudes of these two terms is shown in the bottom panel of Figure 7.6 for two different wavelengths and sample radii. The r^{-2} terms will play a larger role when the sample radius increases, and are shown in more detail in the simulations

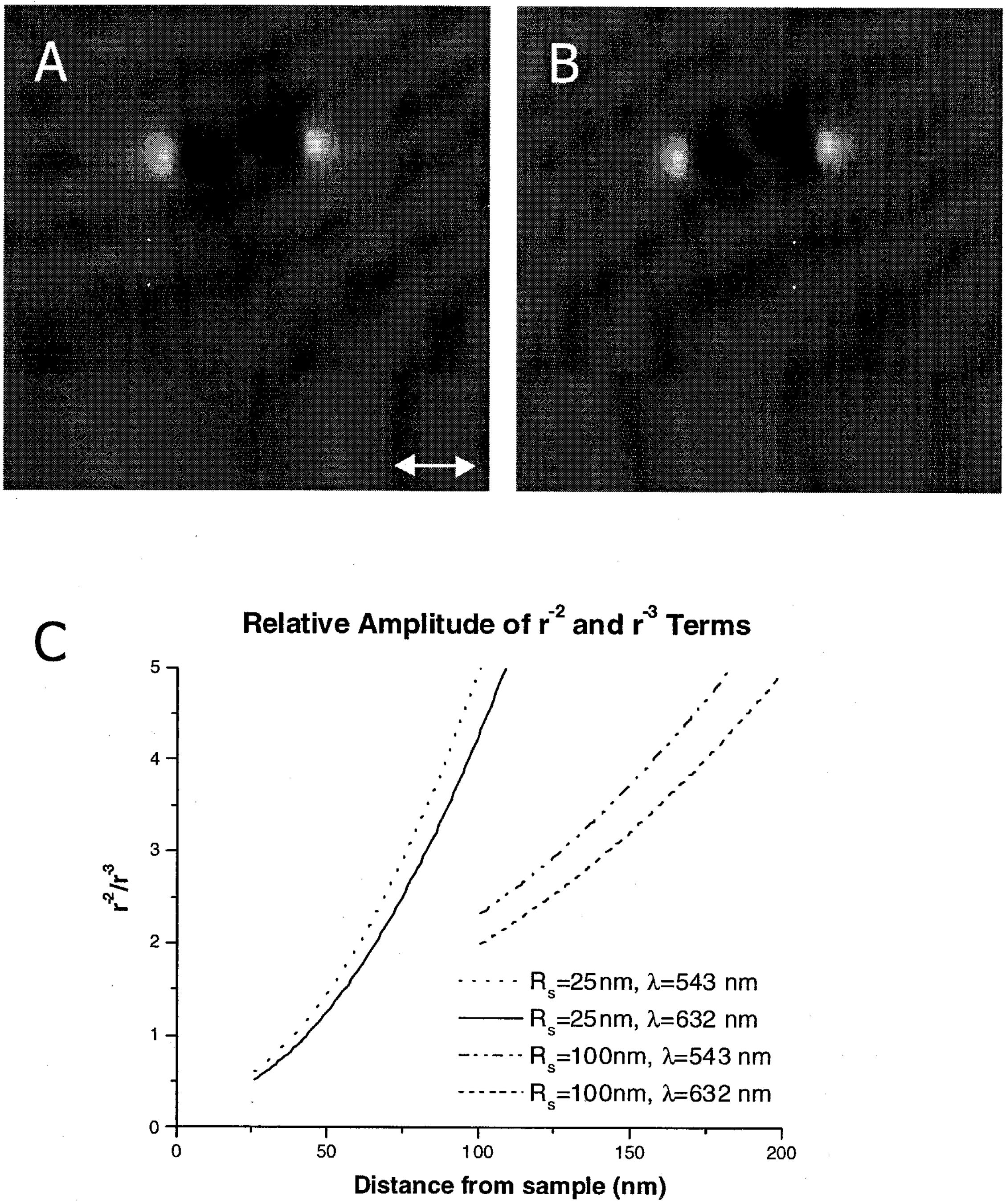

Figure 7.6: Contrast dependence on wavelength of external laser. (A) 632.8 red. (B) 543.5 green. Intensity difference is about 0.5%. Horizontal polarization is used as indicated by the arrow. (C) Relative amplitude of the r^{-3} and r^{-2} terms in the samples electric field.

involving 200 nm beads. The implications here are that for samples smaller than 50 nm the amplitude dependence on wavelength is very small. Therefore a spectroscopic SAM analysis of features this size or even large molecules the data will depend mostly on the material properties at that wavelength via n and not on the wavelength itself.

These images show clearly that the dipole model can image differences in optical properties. If this simple dipole-dipole scattering model is the dominant source of contrast in our apertureless technique then we can, in theory, image information about a sample that is indeed optical in nature. One of the nicest aspects of the model is that it contains no fitting parameters; all physical constants used are well known or easily measured.

7.3 Near Field Dipole Visualization Experiments

The results of the previous section indicate that the polarization of the external laser can have a significant effect on the image. To test this 200 nm diameter polystyrene spheres adsorbed on a glass substrate were imaged while varying the direction of linear polarization of the external laser. Two beads were found side by side, and an AFM image of them is shown in Figure 7.7. The topographical data from Figure 7.7 is used to perform the simulations in Figure 7.8. The other relevant parameters used were n =1.59, R_s =100 nm, R_t =10 nm, λ =632 nm. These simulated images are similar to those generated in the previous section. The only notable exception is the ring in intensity around the features at a distance of approximately 400 nm. This is due to the fact that we are now in a regime where the amplitude of the r^{-2} terms is greater in magnitude than for the r^{-3} terms. The cross terms between the laser and sample fields contain a component which is oscillatory in distance from the sample. The explicit expression for the cross term is

$$\langle \vec{E}_{laser} \cdot \vec{E}_s^* + c.c. \rangle = |E_{laser}|^2 \frac{Re(\alpha_s)}{2R_f^3} \left\{ \begin{array}{cc} \cos \xi d_- \frac{R-\cos\theta}{d_-^3} & -\cos \xi d_+ \frac{R+\cos\theta}{d_+^3} \\ +\xi \sin \xi d_- \frac{R-\cos\theta}{d_-^3} & -\xi \sin \xi d_+ \frac{R+\cos\theta}{d_+^3} \end{array} \right\}, \quad (7.1)$$

where $\xi = R_s/k$ and all other terms have been previously defined.

The SAM data of these beads imaged with linearly polarized light are shown in Figure 7.9. Above each sample the signal is reduced, which corresponds the destructive interference between the external and sample fields explained in equation 6.7 and Fig 6.3. Even if they exist, the noise level in the images is too high to see any of the oscillations shown in the simulations. However, clear differences arise in the experimental images as the polarization of the external laser is changed. There is one bright feature that shows up in the unpolarized image as well as panel (d) along the direction of laser polarization. The feature is also bright panel (c) and extinguished in (b). If this were truly a measurement of the dipole field of a sphere, then the images should look much more like the simulation. A more probable explanation is that the asymmetry in the bead manifests itself as an edge in the lower left corner where the

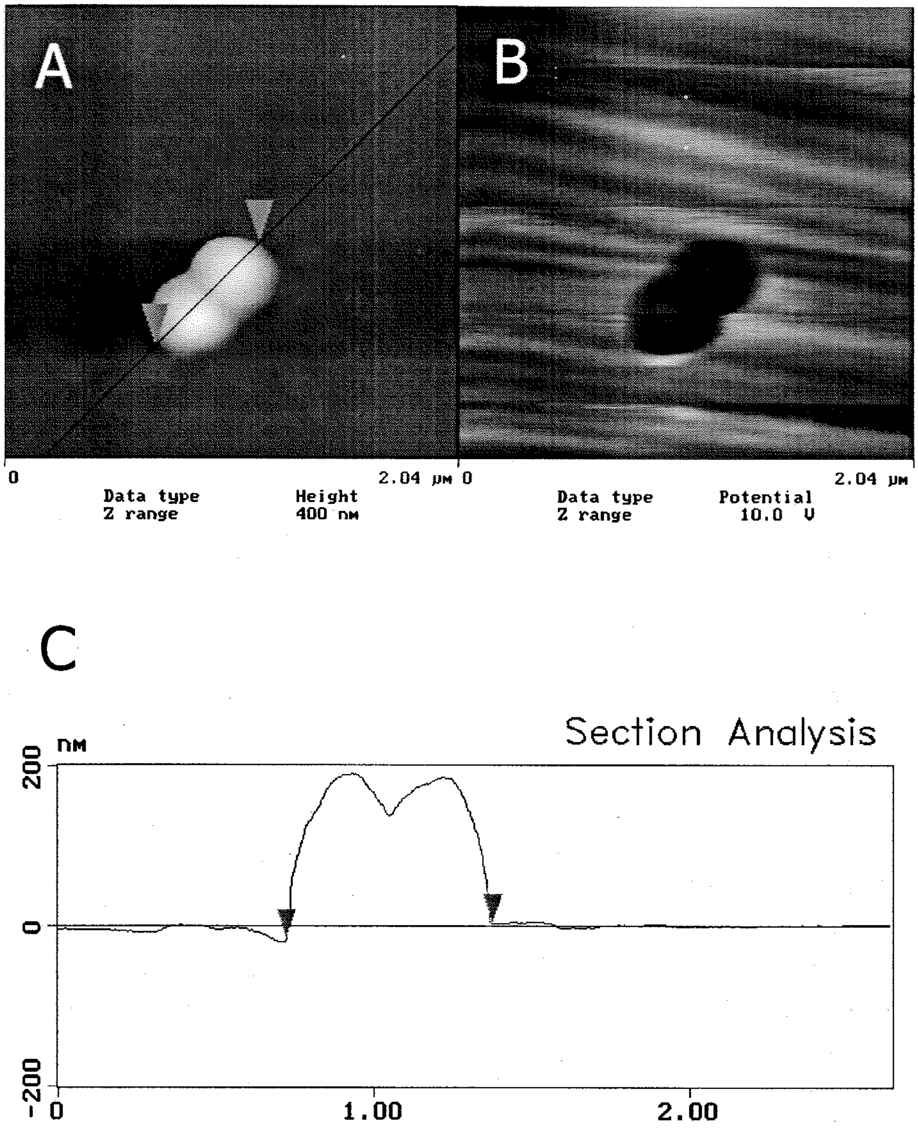

Figure 7.7: (A) AFM and (B) unpolarized SAM images of 200 nm polystyrene beads. (C) Section analysis of the AFM data in (A).

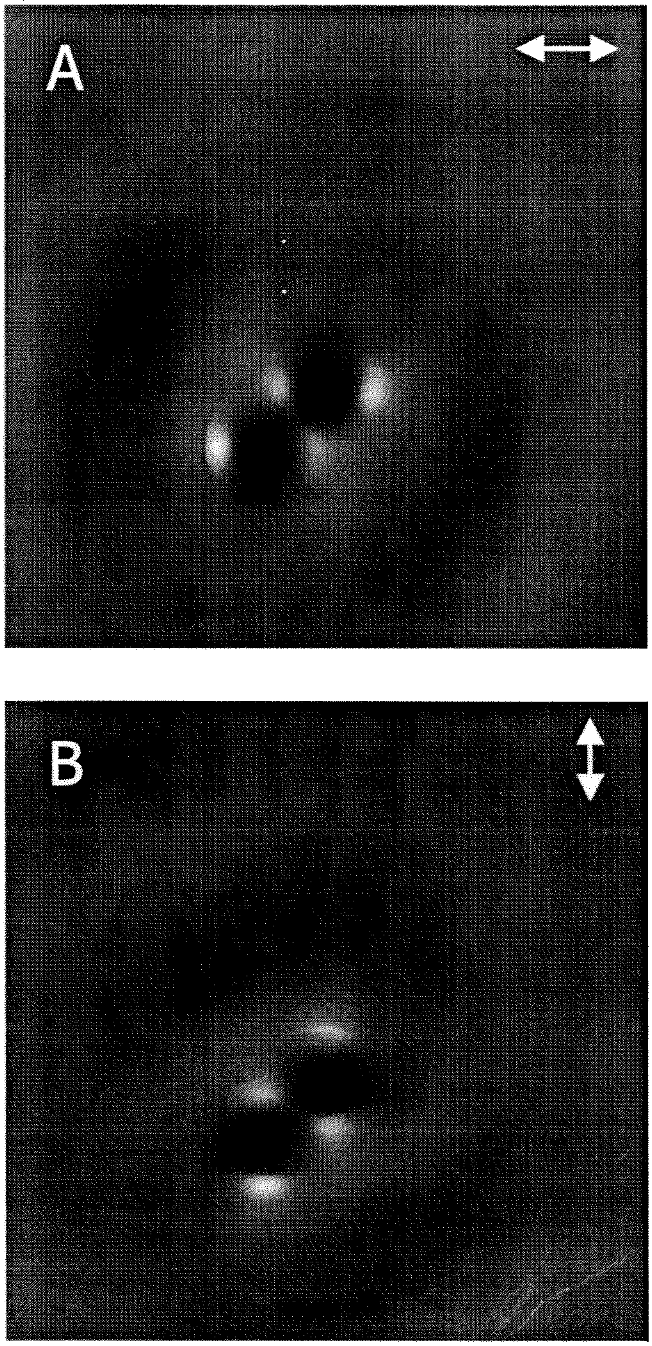

Figure 7.8: Simulations for 200 nm polystyrene beads with external laser polarization in the direction indicated by the arrow. (A) horizontal polarization, data range 0.71 to 1.89. (B) vertical polarization, data range 0.71 to 2.08. White indicates highest intensity.

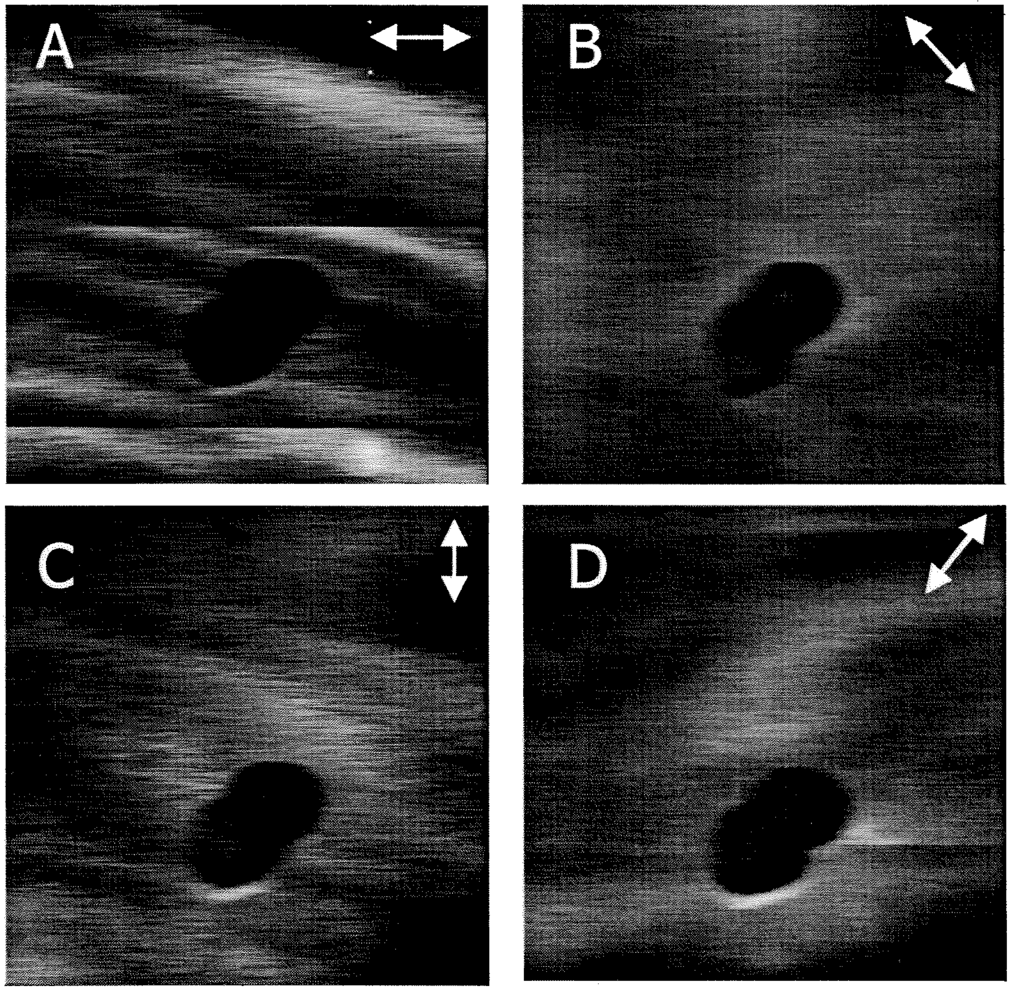

Figure 7.9: Actual SAM images with linearly polarized external laser for the 200 nm spheres. Direction of external laser polarization is indicated by the arrows.

local dipole electric field is very strong. It is the author's opinion that one would be quite fortunate to see even one out of the many possible "hot spots" in sample field due to their localized nature and the fact that the model attributes perfect sphericity to objects that surface tension turns into ellipsoids.

These experiments do show a strong polarization dependence in the images as well as destructive interference lowering the signal intensity when the tip is above the sample. There have been studies which used s and p polarizations to illuminate cylindrical aluminum dots patterned on a quartz substrate [1, 2]. They observed image enhancement between dots along the direction of polarization much like that shown here. The periodicity of their sample makes the effect quite obvious and the effects are explained by variations in electric field caused by the metal-air interface. Other studies done with polarization dependence in apertureless microscopy have focused on the intensity of the scattered signal and not the contrast [3].

7.4 Analysis of the Dipole Model

All of the features predicted by the dipole model do not show up in the images. In fact, in large scale images the features often appear only as contrast to the background diffraction image. Samples appear more intense when the background diffraction pattern is dark and less intense when the diffraction pattern is bright. This indicates that some cavity resonances are playing a role or topography is influencing the optical image. However, the polarization sensitivity shown here and in other experiments indicates that the directionality of the electric field does indeed play a role in image formation. Experiments need to be performed on size standards of different polarizability to test the optical resolution claims of the dipole model.

Bibliography

[1] P. M. Adam, P. Royer, R. Laddada, and J. L. Bijeon, Appl. Opt. **37**, 1814 (1998).

[2] P. M. Adam, P. Royer, R. Laddada, and J. L. Bijeon, Ultramicroscopy **71**, 327 (1998).

[3] L. Aigouy, A. Lahrech, S. Gresillon, H. Cory, A. C. Boccara, and J. C. Rivoal, Opt. Lett. **24**, 187 (1999).

Chapter 8 The Future of SAM

The future of scanning apertureless microscopy is very promising. The dipole model lends credence to the following important points:

- Resolution is limited by tip size
- The SAM image is sensitive to the optical properties of the sample
- The polarization of the external laser can enhance image contrast
- The method lends itself to use at many wavelengths

The most promising of these results are the tip dependent resolution and the ability to image optical properties on nanometer scales. It is easy to imagine possible biological or chemical sensing applications. Organic molecules tend to have vibrational/rotational resonances at energies corresponding to infrared wavelengths. It is not outside the realm of possibility to take some of the larger molecules and run a multi-spectral SAM image on them. It is theoretically possible to image large organic molecules. In the experiment one can choose wavelengths to select the C-N, C-O, or C-H bond resonances. In the scan it may even be possible to have the individual bonds light up with the correct wavelength. Ultimately this could allow determination of biological origin in the field. Imaging of large biological samples with the SAM has already been reported [1].

Additionally, more sensitive interferometric measurements have been preformed which claim sub-nanometer resolution. Some of the possible applications for this technique include high density data storage and retrieval [2]. Over the past two years many more groups have adopted apertureless techniques and applied them to such diverse subjects as ferroelectric domains [3] and surface plasmon modes [4], and imaging AlGaAS laser diodes during operation [5].

Bibliography

[1] P. M. Bridger and T. C. McGill, Scanning **21**, 229 (1999).

[2] Y. Martin, S. Rishton, and H. K. Wickramasinghe, Appl. Phys. Lett. **71**, 1 (1997).

[3] X. K. Orlik, M. Labardi, and M. Allegrini, Appl. Phys. Lett. **77**, 2042 (2000).

[4] P. M. Adam, S. Benrezzak, J. L. Bijeon, and P. Royer, J. Appl. Phys. **88**, 6919 (2000).

[5] G. Wurtz, R. Bachelot, and P. Royer, Euro. Phys. J. Appl. Phys. **5**, 269 (1999).

Appendix A Measurement of Circularly Polarized Light

In our experiments we are mainly concerned with the degree of circular polarization of the luminescence emitted from the semiconductor surface. Before detection the signal passes through a $\lambda/4$ plate and a linear polarizer, the relative alignment of which can select out the circularly polarized components of the total intensity. We therefore need a method of characterizing the polarization state of the initial light given the intensity at the detector for various configurations of the optics. The two most common ways to perform this type of characterization are the methods of Jones and Muller. The Muller calculus most readily lends itself to our experiments due to the fact that it is intensity-based and can deal with light which is not completely polarized. A brief introduction to the Muller calculus and how it is applied in the analysis of our data will be given here.

The electric field of light propagating in the z direction with angular frequency ω in a given medium with wave number k can be characterized in complex exponential notation as

$$\vec{E} = (A_x e^{\phi_x}\hat{x} + A_y e^{\phi_y}\hat{y})e^{i(kz-wt)}, \tag{A.1}$$

where A_x and A_y represent the amplitudes of the electric field along the x and y directions, respectively, and ϕ_x and ϕ_y are the phases. From this equation we can get the four (unnormalized) Stokes parameters [1]:

$$\begin{aligned} I &= A_x^2 + A_y^2 \\ Q &= A_x^2 - A_y^2 \\ U &= 2A_xA_y cos(\phi_x - \phi_y) \\ V &= -2A_xA_y sin(\phi_x - \phi_y) \end{aligned}$$

(A.2)

I is the total intensity. Q is the intensity of the component linearly polarized along x minus the intensity of the component linearly polarized along y. U is similar to Q except the linear polarization axes are taken to be +45° and -45° with respect to the x axis. V is the intensity of right circularly polarized light (RCP) minus the intensity of left circularly polarized light (LCP). For clarity it must be stated that RCP designates light with angular momentum $-\hbar$ along the direction of propagation [2], as is standard notation in optics but not in quantum mechanics. These four parameters completely determine the polarization state of the light in question. The Stokes parameters obey the relation $I^2 \geq Q^2 + U^2 + V^2 \geq 0$, where the first equality holds if the light is completely polarized and the second holds when the light is completely unpolarized. In the Muller calculus the light to be analyzed is represented by a column vector where the four components are the Stokes parameters:

$$\vec{S} = \begin{bmatrix} I \\ Q \\ U \\ V \end{bmatrix}. \tag{A.3}$$

An optical element that changes the polarization state of the light from $\vec{S}$ to $\vec{S}'$ is represented by a 4x4 Mueller matrix M such that $\vec{S}' = M\vec{S}$. In our optical experiments we use a $\lambda/4$ plate followed by a linear polarizer. The Mueller matrices representing these elements are [1]

$$M_{linpol}(\theta) = \frac{1}{2}\begin{bmatrix} 1 & \cos(2\,\theta) & \sin(2\,\theta) & 0 \\ \cos(2\,\theta) & \cos^2(2\,\theta) & \sin(2\,\theta)\cos(2\,\theta) & 0 \\ \sin(2\,\theta) & \sin(2\,\theta)\cos(2\,\theta) & \sin^2(2\,\theta) & 0 \\ 0 & 0 & 0 & 0 \end{bmatrix} \tag{A.4}$$

for the linear polarizer where θ is the angle between the x axis and the polarizer axis and

$$M_{\lambda/4}(\alpha) = \begin{bmatrix} 1 & 0 & 0 & 0 \\ 0 & \cos^2(2\,\alpha) & \sin(2\,\alpha)\cos(2\,\alpha) & -\sin(2\,\alpha) \\ 0 & \sin(2\,\alpha)\cos(2\,\alpha) & \sin^2(2\,\alpha) & \cos(2\,\alpha) \\ 0 & \sin(2\,\alpha) & -\cos(2\,\alpha) & 0 \end{bmatrix} \tag{A.5}$$

for the $\lambda/4$ plate where α is the angle between the x axis and the fast axis of the plate.

In our experiments we wish to make a measurement of V, the degree of circular polarization. Specifically, when light traveling in the z direction passes through a quarter wave plate with the fast axis along x and then through a linear polarizer oriented at a $\pi/4$ azimuthal angle, a measurement of the RCP component of the intensity is made. When the linear polarizer is oriented at $-\pi/4$, one then measures the LCP component of the intensity. The difference of the two is V.

The simplest way to do this accurately is to rotate the $\lambda/4$ plate while fixing the position of the linear polarizer. The STM luminescence with Stokes parameters $\vec{S}$ first travels through the $\lambda/4$ plate and then the linear polarizer, so our final Stokes parameters would be $\vec{S'} = M_{linpol}(0)M_{\lambda/4}(\alpha)\vec{S}$. The resultant I' would be

$$I' = \frac{1}{2}\left(I + \cos^2(2\alpha)Q + \sin(2\alpha)\cos(2\alpha)U - \sin(2\alpha)V\right). \tag{A.6}$$

Note that the two components of the linear polarization Q and U are $\pi/2$ periodic in α, while the circularly polarized component V is π periodic in α. If we were instead to fix the position of the $\lambda/4$ plate and rotate the polarizer, the intensity of $\vec{S}' = M_{linpol}(\theta) M_{\lambda/4}(0) \vec{S}$ would be

$$I' = I + \cos(2\theta)Q + \sin(2\theta)V. \tag{A.7}$$

This method suffers from the problem that the linearly polarized component and the circularly polarized component are π periodic. This is not a problem as long as the angle between the fast axis of the $\lambda/4$ plate and the linear polarizer is exactly $\pm\pi/4$, and then the cosine terms are zero. Otherwise, there will be a small error introduced by any misalignment of the optics. In the rotating $\lambda/4$ plate method as long as the relative positioning of the quarter wave plate is accurate then the linear polarization components must cancel. With the Micos rotation controller we have accuracy of 0.001° in relative positioning, making the rotating $\lambda/4$ plate method the most desirable.

One of the other problems with rotating the linear polarizer has to do with the polarization sensitivity of the PMT and the fiber coupling. In order to counteract this problem we used a liquid-filled light pipe that was non-polarization preserving to take the light from the microscope to the PMT in the initial GaN experiments.

The final point contrasting these two methods is that the rotating $\lambda/4$ plate method allows for the determination of all four Stokes parameters, allowing one to completely specify the initial polarization state of the light. Simply rotating the polarizer will not allow the determination of U.

Bibliography

[1] D. Kliger, J. Lewis, and C. Randall, *Polarized Light in Optics and Spectroscopy*, 1st ed. (Academic Press, Inc., New York, NY, USA, 1990).

[2] E. Hecht, *Optics*, 2nd ed. (Addison-Wesley, Reading, MA, 1987).

Appendix B Magnetic Tip Preparation and Characterization

B.1 Tip preparation

B.1.1 Fabrication

The nickel, cobalt, and iron tips used in the magnetic experiments were all fashioned from high purity wire purchased from Alfa Aesar. The nickel wire is 99.994% pure with respect to other metallic contaminants. Similarly the cobalt wire is listed as 99.995% pure and the iron is 99.998% pure. Other elemental metals are assumed to be the dominant impurity. The amount of other common impurities, such as carbon, is not provided by the manufacturer.

The tips are then made from a standard technique where stainless steel scissors are used to pinch the wire at an angle while pulling. The best tips are made when the wire snaps as it is cut, keeping the scissor blades from damaging the fresh tip. Although this method sounds crude, in our laboratory it reliably produces tips which can produce atomic resolution images on graphite (HOPG) standards.

A sharp tip is necessary but not sufficient for producing a large amount of luminescence signal from a semiconductor surface in our experimental geometry. Tips with pencil-like endings are not desirable since we are collecting light emitted normal to the semiconductor surface and the tip comes in at a 10 to 20° angle from the normal. A more desirable tip shape has a chisel-like symmetry, allowing for unobstructed viewing of the contact area.

Although nearly all commercial PtIr tips we used have this type of symmetry, perhaps one in three of our hand-fashioned tips give this favorable shape. If a tip has not been blunted by the scissor blades, this tip will generally give good light emission.

Once a tip has crashed or has become damaged in handling, however, it will no longer give light.

B.1.2 Magnetization

A small ceramic tube mounted on a circuit board was used to place the tips inside a Power and Buckley electromagnet. The field inside the magnet can reach 6000 Oe at 8 Amperes current as read by a Lakeshore Cryogenics 421 Gaussmeter. The meter actually reports magnetic induction in Gauss, but since μ_o is 1 in air Gauss can be used interchangeably with Oersteads. This field is more than enough to fully magnetize polycrystalline Ni and Fe. It should also be sufficient for polycrystalline Co, although technically along the hard axis a field of 8000 Oe is needed. Tips are placed in the holder and the high field is applied. The field is then ramped down to near zero and the tips are removed from the magnet. Only after the initial GaN experiments did we learn that turning off the power supply to the magnet sends a brief surge of current in the opposite direction and this can demagnetize the tips. After this discovery we began to place the tips in close proximity to the Gaussmeter to check that the magnetization is in the right direction. Nickel and cobalt give the strongest fields outside the tip, on the order of 10 Oe when placed as close as possible to the probe.

The tips are then mounted in the STM tip holder for light emission experiments. After the experiments are performed, the tip is removed from the STM holder and again the tip is placed close to the Gaussmeter to check that the magnetization is still in the right direction. We have noticed that nickel with its lower Curie temperature of 350°C can come out of the STM demagnetized.

The process is then repeated for opposite magnetization. Unfortunately, there is a limit on the number of times a tip can be placed into the magnet with our crude tip holder and still come out sharp.

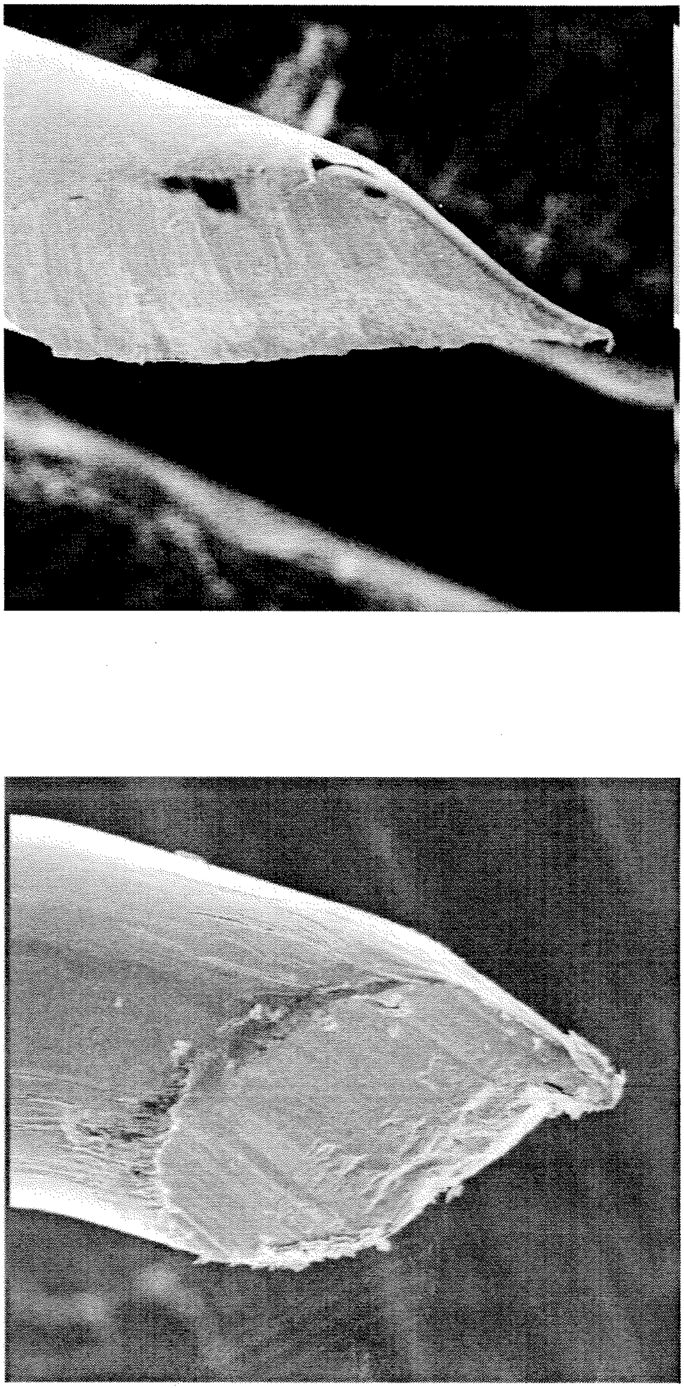

Figure B.1: SEM of PtIr (top) and Ni (bottom) tips.

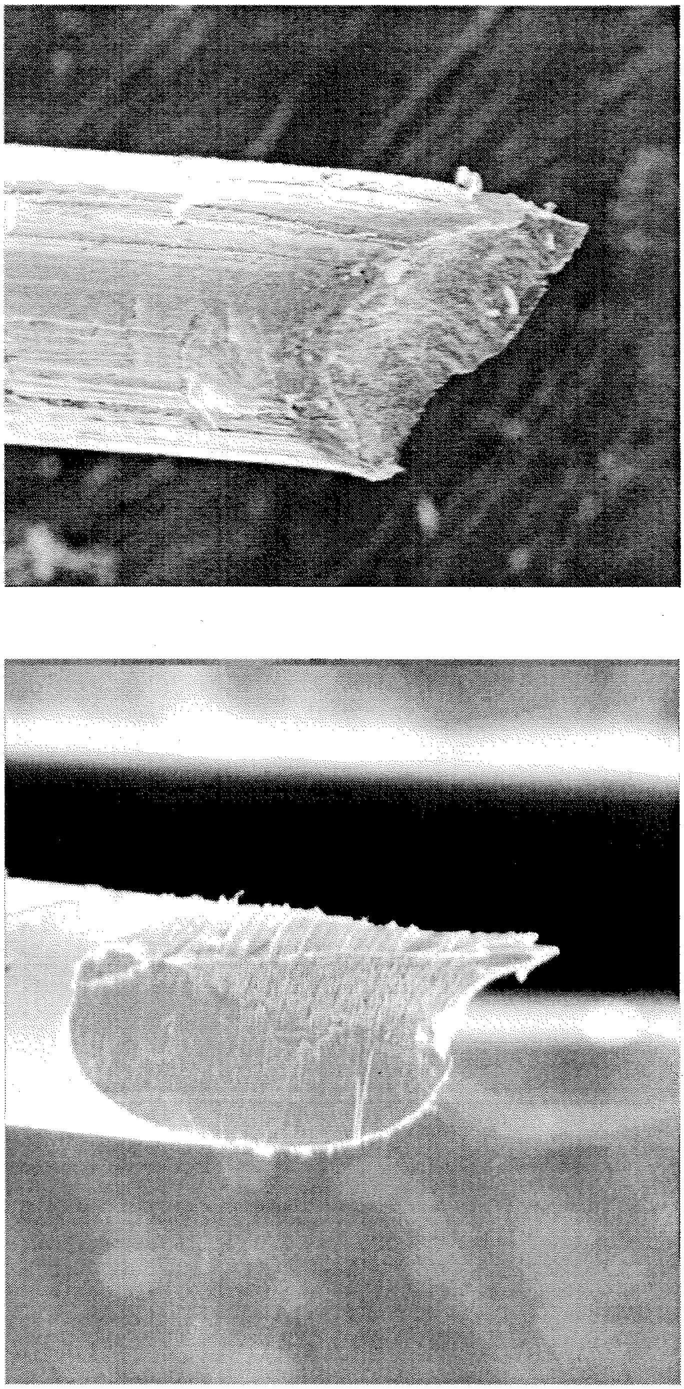

Figure B.2: SEM of Co (top) and Fe (bottom) tips.

B.2 SEM Images

Scanning electron microscopy (SEM) images of PtIr, Ni, Co, and Fe tips are shown in Figures B.1 and B.2. All tips shown have been used for data collection and no longer emit light. The top panel of Figure B.1 shows a commercial PtIr tip. This type of tip has a more tapered profile than the other three tips. The mechanical cutting method gives the best tip shapes with the ductile Fe wire. This method does not work nearly as well with Co, where snapping the wire is the best way to achieve sharpness. All three magnetic materials have been able to produce images of atomic resolution in our lab, which is vitally important to the spin injection project due to the integral role of the current density in spin injection.